DOCTORAL THESIS

FUNCTIONALIZED MAGNETOELASTIC RESONANT PLATFORMS FOR CHEMICAL AND BIOLOGICAL DETECTION PURPOSES

Report presented to aim for the degree of Doctor by:

Ariane Sagasti Sedano

(2018)

Universidad del País Vasco

Euskal Herriko Unibertsitatea

eman ta zabal zazu

Universidad del País Vasco

Euskal Herriko Unibertsitatea

FUNCTIONALIZED MAGNETOELASTIC RESONANT PLATFORMS FOR CHEMICAL AND BIOLOGICAL DETECTION PURPOSES

Report presented to aim for the degree of Doctor by:

Ariane Sagasti Sedano

(2018)

BCMATERIALS
BASQUE CENTER FOR MATERIALS, APPLICATIONS & NANOSTRUCTURES
ehugroup

Resumen

En los últimos años, la investigación sobre materiales magnetoelásticos se ha centrado en sus aplicaciones en el campo de los sensores tanto químicos cómo biológicos, aprovechando el hecho de que este tipo de materiales permiten la detección de manera remota.

Los materiales magnetoelásticos son materiales ferromagnéticos que presentan magnetoelasticidad. La magnetoelasticidad, también conocida como efecto Villari, es el fenómeno opuesto a la magnetostricción o efecto Joule. Los materiales magnetostrictivos se elongan o contraen cuando son sometidos a un campo magnético, mientras que los materiales magnetoelásticos sufren cambios en su estado magnético cuando son sometidos a tensiones, siendo el valor de la magnetostricción el que determina el tipo de comportamiento que presentará el material. Los materiales presentados en este trabajo poseen valores positivos de magnetostricción, ya que son los que usualmente se emplean como sensores. Debido a esto un material magnetostrictivo/magnetoelástico es un material ferromagnético que se deforma continuamente cuando se encuentra bajo la influencia de un campo magnético. De esta manera, excitando el material con un campo magnético podemos a partir de estas propiedades magnetoelásticas hacer que este vibre exhibiendo una frecuencia de resonancia característica. Esta frecuencia de resonancia, que varía en función de ciertos parámetros como la longitud de la cinta o la densidad, hace que nuestro material sea sensible a cambios en la masa, entre otros, siendo esto lo que fundamenta la base para las aplicaciones como sensor que se van a presentar.

Dentro de los materiales ferromagnéticos, las aleaciones amorfas presentan excelentes propiedades magneto-mecánicas y más concretamente las ricas en hierro presentan un alto coeficiente de acoplamiento magnetoelástico. Por tanto los materiales magnetoelásticos amorfos presentes a lo largo del trabajo son en base hierro, fabricados en forma de cinta por el método "melt-spinning". Aleaciones con distintas composiciones se han empleado para los distintos tipos de sistemas. Sin embargo, para que estas cintas puedan actuar como sensores es necesario recubrirlas con algún "material activo",

es decir, que sea capaz de detectar y atrapar las moléculas objetivo. De esta manera, el incremento en la masa del sistema dará lugar a un descenso en la frecuencia de resonancia, mediante el cual podrá calcularse la concentración presente en el medio del compuesto a detectar. Para esto previamente se habrá realizado un calibrado del sistema siguiendo la evolución de la frecuencia de resonancia con concentraciones conocidas del compuesto a detectar.

El principal objetivo de este trabajo de tesis doctoral es por tanto desarrollar sensores basados en el efecto magnetoelástico para detección tanto química como biológica. Para tal fin, las cintas amorfas se han recubierto con "materiales activos" de distinta naturaleza, polímeros, compuestos semiconductores y aluminosilicatos. En todos los casos, el objetivo final es llegar a desarrollar un sensor que deberá cumplir una serie de requisitos como son alta sensibilidad, buena reproducibilidad y estabilidad, rápida respuesta, bajo coste y, en algunos casos, buena resistencia a la corrosión.

Durante el transcurso de los experimentos se hizo evidente la importancia de que los resonadores magnetoelásticos presentaran una buena resistencia a la corrosión, no solo de cara al objetivo final que es la detección, sino también porque algunos procesos de recubrimiento transcurren por síntesis químicas en medios agresivos que dañan las cintas afectando a sus propiedades. Debido a este hecho, durante el transcurso de este trabajo se han fabricado nuevas cintas amorfas con un pequeño contenido en cromo, ya que se ha encontrado que mejora la resistencia a la corrosión. A fin de estudiar el comportamiento de los distintos resonadores magnetoelásticos frente a la corrosión se han realizado medidas de resistencia a la polarización, con un sistema de tres electrodos. A partir de los resultados obtenidos se puede determinar que las muestras que contienen cobalto presentan menor resistencia a la corrosión que las que presentan níquel, y que efectivamente la adición de un 2% de cromo en la aleación hace que la resistencia a la corrosión se vea mejorada.

Inicialmente los resonadores magnetoelásticos han sido recubiertos con un polímero, poliestireno. A partir de estas primeras pruebas se han estudiado los dos parámetros fundamentales que afectan al proceso de detección, la sensibilidad S y el factor de calidad Q y cómo estos

parámetros se ven afectados al incrementarse la masa del sensor. Siguiendo la evolución de la frecuencia de resonancia con respecto al incremento de la masa del sistema debida a las sucesivas deposiciones de poliestireno ha sido posible determinar el campo aplicado que presenta mayor sensibilidad, que es el campo de anisotropía, es decir, aquel donde se localiza la mínima frecuencia de resonancia durante el barrido en función del campo aplicado. Además la curva de frecuencia medida a este campo aplicado es la que presenta la mayor amplitud, a pesar de que su factor de calidad es el menor por tener la curva más anchura. Por otra parte, se ha estudiado cómo afecta la longitud de la cinta a la sensibilidad, recubriendo cintas de distintas longitudes y estudiando los cambios en la frecuencia de resonancia. Esto ha permitido concluir, tal y como era de esperar, que la cinta más sensible es la más pequeña, de 1 cm de longitud. Sin embargo, para futuros experimentos será necesario tener en cuenta no sólo la alta sensibilidad de cintas de menor longitud, sino el hecho de que al poseer estas menor volumen superficial, la cantidad de moléculas que será posible atrapar también será menor.

Para llevar a cabo la deposición del polímero sobre las cintas magnetoelásticas, ha sido necesario tratarlas con un ácido, a fin de disminuir la rugosidad superficial del material para que la adherencia con el polímero fuera mejor. En cuanto al proceso de deposición del polímero, el método empleado ha sido el "dip coating" y para ello se han empleado dos disolventes diferentes, tetrahidrofurano (THF) y tolueno. El THF presenta un menor punto de evaporación, debido a esto la velocidad a la que el disolvente se evapora formando la capa del film es más rápida que la del tolueno. Por este motivo, aunque el film de polímero parece homogéneo al usar THF como disolvente, al observar la topografía superficial por AFM se observa que no es tan homogénea y de hecho presenta poros que podrían afectar a la capacidad de detección del sistema si el compuesto objetivo a ser detectado penetra y reacciona con la cinta directamente. Debido a esto se ha propuesto como alternativa el tolueno, con mayor temperatura de evaporación, lo cual debe evitar o reducir la formación de esos poros superficiales en el film polimérico. Efectivamente, los resultados obtenidos han revelado una mayor homogeneidad superficial en el sistema depositado a partir de tolueno, sin embargo no se ha conseguido siguiendo el mismo proceso

experimental depositar una cantidad de masa similar, lo cual hace pensar que para cada tipo de deposición sea necesario un estudio inicial sobre las condiciones óptimas de deposición.

En lo relativo a la evolución de la frecuencia de resonancia debido a las sucesivas deposiciones de poliestireno, lo cual supone un incremento en la masa final del sistema, se ha observado que; para cambios relativos de masa pequeños, el sistema cumple con la aproximación teórica que establece una relación lineal, habiéndose obtenido una pendiente de -0.53 cuando la teórica es de -0.5. Sin embargo, cuando el cambio en la masa relativa es mayor, los datos experimentales no se ajustan correctamente a esta aproximación lineal, sino que es necesario desarrollar la expresión de la que se simplifica, obteniéndose así una ecuación polinómica de segundo orden que sí ajusta de manera apropiada los datos experimentales. A pesar de esto, los valores obtenidos para los parámetros de la ecuación no coinciden con los teóricos.

Por otra parte y con el objetivo de desarrollar un biosensor, los resonadores magnetoelásticos fueron recubiertos con óxido de zinc, ZnO. El óxido de zinc es un compuesto inorgánico semiconductor con gran cantidad de aplicaciones debido a sus propiedades. Presenta buena biocompatibilidad, baja toxicidad y buena biodegradabilidad; además de gran transparencia, alta movilidad electrónica, luminiscencia a temperatura ambiente y alta resistencias térmica y química. Nanoestructuras de óxido de zinc ya han sido usadas como sensores químicos para la detección de gases y de agentes biológicos. En este caso se empleará cómo soporte de la hemoglobina que será la capa activa que reaccionará con la molécula objetivo.

Se han estudiado distintas metodologías para recubrir las cintas a partir de las cuales se ha podido concluir que la mejor alternativa para realizar una deposición homogénea que recubra toda la superficie, consiste en realizar procesos de "casting" con una solución a partir de nanopartículas de ZnO previamente sintetizadas. La síntesis de nanopartículas de ZnO se ha llevado a cabo por síntesis hidrotermal y las partículas han sido caracterizadas por XRD y PL. A partir de las nanopartículas dispersas en etanol se han realizado deposiciones sucesivas de ZnO, de tal forma que siguiendo la evolución del

desplazamiento de la frecuencia de resonancia con la masa de ZnO depositada, ha sido posible determinar el valor de módulo de Young del film de ZnO depositado. El valor obtenido, 60 GPa, está en buen acuerdo con los valores obtenido por otros autores para otro tipo de nanoestructuras de óxido de zinc.

Este sistema ha sido empleado en experimentos de biodetección, para determinar la presencia de peróxido de hidrógeno, H_2O_2. Con este objetivo, sobre el film de ZnO se ha depositado hemoglobina, Hb, siguiendo un procedimiento similar al empleado en las deposiciones de ZnO. Se ha añadido una gota de solución de Hb, se ha dejado evaporar el disolvente y se ha eliminado el exceso lavando con solución salina. La hemoglobina es una hemoproteína encargada de la transferencia de oxígeno entre proteínas. Está compuesta por cuatro cadenas peptídicas cada una con un núcleo de hierro capaz de cambiar su estado de oxidación debido a su reacción con el oxígeno del medio. Esta habilidad del hierro de la Hb es lo que la hace adecuada para detectar H_2O_2. Los experimentos de biodetección se han llevado a cabo de manera simultánea por dos técnicas distintas; mediante medidas de resonancia magnetoelástica, sensible a cambios en la masa del sensor; y por métodos voltamétricos, capaces de detectar procesos electroquímicos como son oxidaciones y reducciones. Para esto se ha desarrollado un sistema experimental que permite combinar las dos técnicas, de tal forma que en la tapa de un vial se han colocado los tres electrodos necesarios para las medidas voltamétricas y ese vial a su vez ha sido cubierto con una bobina que será las responsable de las medidas magnetoelásticas. Así, a medida que se iba adicionando H_2O_2 en el vial sobre la solución salina se registraban ambas señales. Se ha registrado un incremento lineal en las corrientes de catálisis medidas en el intervalo 25-350 μM con un coeficiente de correlación de 0.99. Se ha determinado un límite de detección de 25-50 μM, y se ha observado una buena reproducibilidad y estabilidad del sensor, además de una rápida respuesta (30 s). Por otro lado, las medidas de resonancia magnetoelástica han mostrado un pequeño incremento de masa, de tendencia lineal con respecto al incremento en la concentración de H_2O_2 con una pendiente de 152 ng/μM. Este cambio de masa se debe probablemente a la absorción de H_2O_2 sobre el ZnO durante los procesos de reacción electroquímica.

Para finalizar, se han desarrollado sensores para la detección de o-xileno basados en zeolitas. El orto-xileno es un compuesto orgánico volátil muy peligroso en caso de contacto con la piel o los ojos y peligroso en caso de ingesta o inhalación ya que causa la depresión del sistema nervioso central. Su uso en procesos petroquímicos o como disolvente en pinturas, tintas o gomas está muy extendido a pesar de sus peligros ya que los disolventes alternativos son demasiado caros. Para la detección de este compuesto se han usado como "material activo" distintas zeolitas.

Las zeolitas son aluminosilicatos cristalinos porosos que pueden tener origen natural o sintético. Las zeolitas están constituidas por tetraedros de óxidos de aluminio y/o silicio dispuestos formando estructuras tridimensionales definidas por una serie de vacantes y canales de tamaño molecular. Es en estos donde las moléculas de o-xileno quedarán retenidas, dando lugar a un incremento en la masa del sistema que se traducirá en un desplazamiento de la frecuencia de resonancia hacia valores menores.

En función de la proporción de silicio/aluminio y de la forma en que estos se dispongan espacialmente se pueden formar distintos tipos de zeolitas con distintos tamaños de poros. En este trabajo se han sintetizado por métodos hidrotermales sobre las cintas amorfas tres tipos de zeolitas; Faujasite (FAU), Movil-five (MFI) y Lynde Type A (LTA) y se ha estudiado su capacidad para detectar o-xileno. A fin de que la formación de la membrana de zeolita sea homogénea por toda la superficie de la cinta, se ha realizado previo a la síntesis un proceso de deposición de nanopartículas previamente sintetizadas de cada tipo de zeolita mediante "casting", para que posteriormente estas nanopartículas actúen como puntos de nucleación para la formación de la membrana. Tras el proceso de síntesis hidrotermal las zeolitas han sido caracterizadas y su capacidad para detectar y atrapar xileno ha sido estudiada.

Los resultados obtenidos para la zeolita FAU han sido erráticos, lo cual nos lleva a pensar que la membrana no estaba bien formada durante la síntesis. En el caso de la LTA, si se ha observado sensibilidad a la concentración de o-xileno, sin embargo parece que la membrana se satura con las concentraciones que se han estudiado. Finalmente, los resultados obtenidos con MFI sí han mostrado un descenso de la

frecuencia de resonancia con el incremento de la concentración de o-xileno obteniéndose una sensibilidad de 0.69 Hz/ppm. El límite de detección parece estar en 13000 ppm con un cambio casi constante de 5.75 kHz. Por otra parte cabe destacar que los tiempos de recuperación del sistema no ha sido excesivamente largos en ninguno de los casos.

Agradecimientos

He aquí la parte más complicada de escribir de una tesis, según mi punto de vista… y no porque no tenga cosas que agradecer, sino porque según mi criterio esas personas que deben ser agradecidas por haber formado parte de esto y haberme apoyado o ayudado en cualquier aspecto ya lo han sido en el transcurso de estos años y no necesitan estas líneas. De todas formas aquí van mis agradecimientos, si alguna persona se me olvida o se ofende, en el primer caso lo siento, en el segundo…

En primer lugar y como no podía ser de otra forma quiero dar las gracias al director y tutor de esta tesis, Jon Gutiérrez. Gracias por las lecciones de física a esta química y por todo lo que me has enseñado durante este tiempo. Además de por la paciencia, dedicación, motivación y por estar siempre aportando ideas para continuar con el trabajo. Guardaré especial recuerdo del terremoto en Grecia y mi primer congreso en Turín. He aquí tu "media docena" de líneas…

Gracias también a mi directora de tesis María San Sebastián por su ayuda durante el desarrollo de la misma y al BCMaterials por darme la oportunidad de trabajar en este proyecto.

Tampoco me gustaría olvidarme de quien me inició en esto de la investigación, haciéndome un hueco en su laboratorio para realizar el proyecto de fin de máster, Carlos Cesteros, quien me enseño muchas cosas sobre hidrogeles y sus propiedades. Y por extensión la gente con la que tuve la oportunidad de coincidir en el departamento de Química Física, en ese y otros laboratorios.

Por otra parte, agradecer a esas personas, científicas o no, que se han ido cruzando en mi camino tanto de BCM como de EHU y que lo han hecho más agradable. No voy a nombrar a todas y cada una de las personas así que daros por agradecidos chavales.

Durante el transcurso de esta tesis he tenido la oportunidad de poder contar con ciertas personas que me han ayudado a continuar aprendiendo y trabajando. Gracias a: Iñaki Orue por ayudarme con las medidas de AFM y los ciclos de histéresis, Carol Redondo por permitirme hacer uso de su AFM, Luis Bartolomé (Txesko) de SGIKER por permitirme

pesar "mis deposiciones", Virginia Mutto por su trabajo con el Matlab y los ajustes de las Q, Javier Carrizo por acogerme en su laboratorio para tirar las nuevas cintas y Verónica Palomares por su ayuda con la celda electroquímica para las medidas de corrosión.

Μεγάλο μέρος των εργασιών της παρούσας διατριβής διεξήχθη κατά την παραμονή μου στην Πάτρα (Ελλάδα). Γι'αυτό το λόγο θα ήθελα να ευχαριστήσω τους ανθρώπους που μου έμαθαν ό, τι ξέρουν, που με βοήθησαν και μου διευκόλυναν τον δρόμο. Ειδικά τον Δημήτρης Κουζούδης (για τη φιλοξενία μου στο εργαστήριό του), τον Νικόλαος Μπουρόπουλος και τον Εμμανουήλ Τοπογλίδης, χωρίς να ξεχάσω τον απόστολος, τη Βασιά και τον Γεώργιο. Επίσης, τη Μαίρη και την Φιλάνθη με τις οποίες πέρασα λίγο λιγότερο χρόνο, αλλά με φροντίσαν με γλυκά. Επιπλέον, υπήρξε μια οικογένεια που με υποδέχτηκε σαν να ήμουν μέλος της, υπολογίζοντας με στις διήμερες αποδράσεις τους και στις εκδρομές τους στην παραλία, γεγονός που έκανε την παραμονή μου πιο ευχάριστη. Γι αυτό, ευχαριστώ την Amaia, τον Δημήτρη, την Ainhoa και τον Θωμά. Επίσης, ευχαριστώ την Helena, τον Μαρίνο και τον Atreyu για την φιλοξενία τους στην Αθήνα και γιατί μου μάθανε διάφορα για τον Ελληνικό πολιτισμό, μεταξύ άλλων, πώς γιορτάζεται το Πάσχα στην Ελλάδα.

Y por último, agradecer a las personitas que forman parte de mi vida, quienes durante estos años han estado incondicionalmente. Aita eskerrik asko batez ere zure laguntza eskaintzeagatik. Ama muchas gracias por creer en mí. Ainara, Ixone eta Udane, eskerrik asko beti irribar egiteko prest egoteagatik.

Sin olvidarme de Irene, pupete, tú siempre has estado ahí apoyándome y dándome ánimos, hasta cuando todo parecía oscuro... así que mil gracias y mil más por leerte esto antes que nadie para corregir y repasar. Al resto de personas con las que tengo la suerte de compartir mi día a día; Maite, Itxas, Axel; eskerrik asko rollos.

Y para acabar a quien convive conmigo y quien realmente ha visto cómo ha ido involucionando y evolucionando la tesis, Patxi. Muchas gracias por el apoyo y por todos los buenos momentos.

Y no quiero que se me olviden los peludos; Izotz, Negu y Eki, quienes siempre tienen un montón de lametones para cuando se necesitan.

Content

1. Introduction:

Magnetoelastic resonant platforms as sensing devices

This first chapter introduces the resonant sensors focusing on the use and benefits of employing magnetoelastic resonant platforms. It summarizes the importance of metallic glasses for developing a good sensor material. It explains the working principle of these magnetostrictive/ magnetoelastic materials to develop such a sensor, and the importance of several factors as the magnetoelastic coupling coefficient or the quality factor are. It analyses the state of art in the field of magnetoelastic sensors, especially for the ones that have been functionalized with polymers or inorganic compounds to sense different chemical or biological targets. Briefly, the importance of that needed functionalization will be described, as well as some different materials used for that purpose. Finally, the objectives and structure of this report are presented summarizing the content of the whole work.

1.1. Resonant devices for sensing purposes

The word *'transducer'* derives from the Latin verb *'traducere'*, which means 'to convert'. Therefore, a transducer can be defined as a device capable of converting energy from one form into another, which usually has higher capacity for its transmission, storage or processing. Transducers can be found both as the input as well as at the output stage of a measuring system. The input transducer is known as *sensor*, because it senses the desired physical quantity and converts it into other energy form. The output transducer is called *actuator*, as it converts the energy into a form to which another independent system can react[1].

Sensors were introduced time ago and by using them, we are able to observe, to measure and to control phenomena or parameters of our environment. They are used in a wide variety of fields such as electrical engineering, environmental detection, biomedical research or self-driving cars, for example, and they are essential partners in our daily life. Depending on the energy conversion that takes place or the type of material used for this purpose, there are different kinds of sensors and actuators. In this report, I will focus only on acoustic wave based devices. The acoustic sensing principle is based on the precise detection of changes on the properties (usually a resonant frequency) of an acoustic (mechanical) wave travelling through the bulk or the surface of the corresponding sensor material.

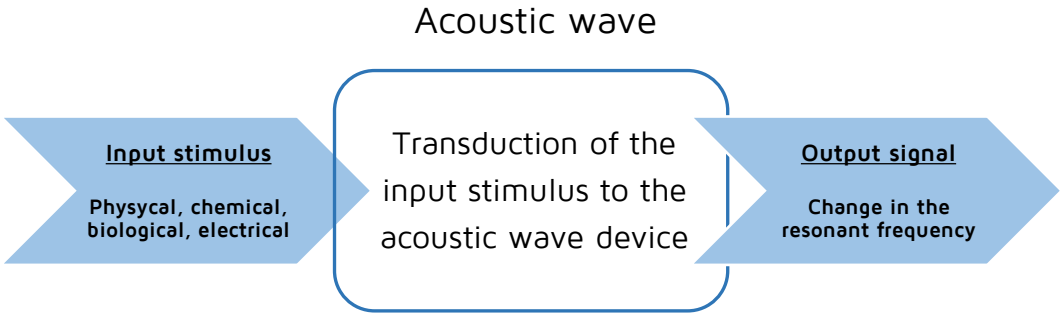

Figure 1.1. Acoustic wave sensors input and output signals.

There are different sensors that use this acoustic principle such as the quartz crystal microbalance, the microcantilevers and, as I will deeply analyse, the magnetoelastic resonant platforms. Each system together with its advantages and disadvantages will be described hereinafter.

❖ Quartz Crystal Microbalance (QCM)

Traditional acoustic wave sensors are based on piezoelectric crystals, which allow transduction between electrical and acoustic energies. A number of configurations of acoustic devices have been constructed, including Surface Acoustic Wave (SAW), Bulk Acoustic Wave (BAW), Flexural Plate Wave (FPW) or Thickness Shear Mode Resonators (TMS), the latter also known as Quartz Crystal Microbalance (QCM).

A quartz crystal microbalance typically consists of a thin disk of AT-cut quartz crystal, which is piezoelectric, with circular electrodes patterned on both sides as shown in Figure 1.2[2].

Figure 1.2. Both sides of a quartz crystal resonator and a quartz crystal microbalance system.

When an alternating current is applied between the electrodes, due to the piezoelectric properties and crystalline orientation of the quartz crystal, mechanical oscillations will be induced giving as a result an alternating deformation. This will generate a wave that will propagate through the sensor material (the quartz crystal).

The resonant frequency of this wave depends on the oscillating mass of the sensor and adhered layers. Therefore, if there is a change into the mass of the system both the resonant frequency and its amplitude will be modified proportionally.

QCM was originally used to measure metal deposition rates[3] and it has proved to be especially effective in the study of molecular interactions at solid interface[4]. Most recently, quartz crystal microbalance devices have been employed as physical[5], chemical[6] and biological[7] sensors. It has been also demonstrated that QCM devices can detect biological warfare agents, including bacterial spores after being coated with binding probes.

This method has clear advantages as its high sensitivity, continuously measurement mode and a quick detection time, with the specific binding to the electrodes the detection of a target analyte has been reported within minutes.

Nevertheless, the major disadvantage of the QCM sensors relays on the complex electronic circuitry needed for signal acquisition. Additionally, QCM sensors are sensitive to temperature, film stress and electrical noise.

- **Microcantilever (MC) like devices**

Micro-machined cantilevers were first fabricated and used as force probes on Atomic Force Microscopy (AFM). In 1994, researches from Oak Ridge National Laboratory and IBM Zurich found that a standard AFM cantilever could be used as a microsensor[8,9]. Depending on the material used to fabricate the microcantilever, they are classified in three types: silicon based MCs, piezoelectric based MCs and magnetostrictive based MCs. Figure 1.3 shows a scheme of how a microcantilever type system works.

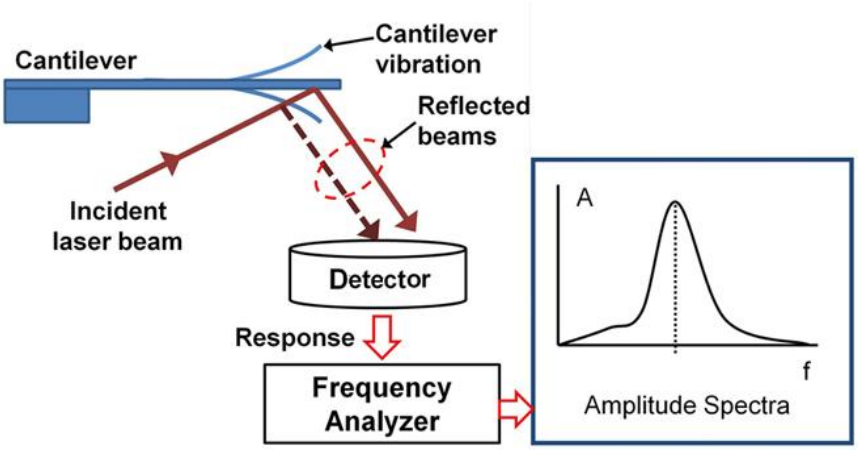

Figure 1.3. Schematic cantilever based detection system.

Silicon turns out to be an easy material for micro-machining. For silicon-based microcantilevers, an optical deflection technique is used to measure the deflections of the cantilever and the resonance frequency changes using a position sensitive detector that tracks the reflection of a laser beam on the surface of the microcantilever. As it can be expected, the optical system need to make such detections is very complex and it is not suitable for long duration measurements.

In the case of piezoelectric based microcantilevers, the resonance frequencies can be easily measured by an impedance analyser. When an electric field is applied, the piezoelectric layer changes its shape causing the bending of the whole structure. An alternating electric field makes the MC vibrate, resonating when the frequency of the AC power matches with the own mechanical vibration frequency of the beam. Piezoelectric base microcantilevers are easy to actuate and detect compared to silicon based ones. However, they are not suitable for measurements in liquids because of the need of electric connexions. Besides, the actuating electric field requires an extra insulation if it is going to be used in a conductive liquid, which makes the fabrication process more complicated and reduces the sensor performance.

Finally, magnetostrictive based microcantilevers developed by Z.Y. Cheng at Auburn University are composed[10], similar to the piezoelectric based ones, by one layer of magnetostrictive alloy and one layer of non-magnetostrictive metal. These MCs sensitivity is higher than in the other MC devices due to the material properties. Magnetostriction is a material

property that will be extensively described in the following, but one of the main advantages of this magnetostriction based microcantilever is the lack of complex electrical connections and possible short-circuits as they use the magnetic field to transfer signals.

Summarising, cantilevers have been researched to measure a wide range of physical, chemical and biological properties of materials and in solutions[11,12]. Nevertheless, they present the same problem as the QCM, the need of complex electrical connections or circuits as well as a complex and expensive equipment to measure the generated signals. In Table 1.1 the main characteristics of each kind of microcantilevers are summarised.

Table 1.1. Comparison of different materials used to fabricate microcantilevers working as sensor platforms[13].

	Silicon-based	***Piezoelectric***	***Magnetostrictive***
Structure	Simplest	Complicated	Simpler
Fabrication	Easy	Difficult	Easy
Actuating	Mechanical (difficult)	Electrical (connexions needed)	Magnetic (easy, wireless)
Sensing	Optical (bulk system)	Electrical (connexions needed)	Magnetic (wireless)
In air	Good	Good	Good
In liquids	Difficult	Very difficult	Works well
Q value	High	Low	Very high
Overall sensitivity	High	Low	High

❖ **Magnetostrictive/magnetoelastic materials**

The mechanical vibration of the magnetoelastic material would be generated by sending a time-varying magnetic signal; the magnetoelastic material would in response generate a time varying magnetic flux that could be detected with a set of pick-up coils. The vibration of the sample would additionally generate acoustic waves, which could be detected with a microphone. Furthermore, a laser beam could be reflected from the surface of the sensor, and the response of the sensor characterised by recording the changes in the returned beam intensity. Figure 1.4 illustrates the three different ways to monitor the magnetoelastic sensor response: magnetically, acoustically and optically. The magnetic detection method has the highest precision.

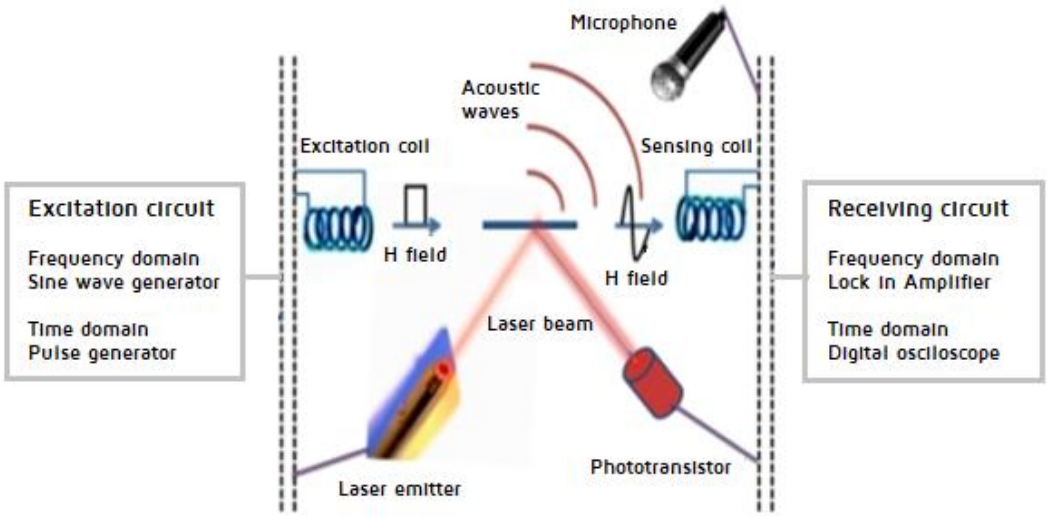

Figure 1.1. Magnetic excitation of a magnetoelastic sensor platform and response detected by magnetic, acoustic, or optical techniques[14].

Magnetoelastic sensor platforms were originally used for chemical and physical detections, such as liquid density[15], viscosity[16], pH[17,18], humidity or temperature[19]. Recently, detection of chemical gasses or biological molecules has been achieved. For these kinds of detection, the immobilisation of a selective and specific functional layer covering the magnetoelastic platform for binding of target analyte has been found necessary. Several sensors have been reported for different molecule

detection. For gases, for example there are NH_3 sensor[20], CO_2 sensor[21] and volatile organic compound (VOC) gas sensors[22]. In the case of biological detection, there are glucose sensors[23] but usually research is focused on bacteria detection, as for example *E.coli*[24], *Salmonella enterica typhimurium*[25] and *Bacillus Anthracis Sterne spores*[26].

Magnetoelastic sensor platforms present several advantages. Many magnetoelastic materials are very cheap, which greatly reduces the cost of this kind of sensors allowing them to be used in a disposable manner. Besides they have a simple structure and the fabrication process is not too laborious. The main advantage of using magnetoelastic sensors is the fact that no complicated electrical connexions or wires are required to give us information about the sensor environment. As I previously mentioned the excitation and detection processes work by applying an external alternating magnetic field, which allows us to measure it wirelessly and remotely.

1.2. Magnetoelastic resonant platforms (MRPs)

Ferromagnetic amorphous alloys, usually metallic glasses containing Fe, Ni and/or Co, are excellent magnetoelastic materials, despite their moderate magnetostriction value. These alloys present a good coupling between magnetic and elastic properties and, in fact, combine simultaneously excellent magnetoelastic and mechanical properties.

Magnetostrictive/magnetoelastic materials exhibit both the Joule effect and the Villari effect. In other words, these materials change their shape when subjected to a magnetic field and, conversely, suffer a magnetization change when a mechanical stress is applied to them. This bi-directional coupling provides the transduction capability when working as sensing devices. In the following, all these aspects will be extensively described.

1.2.1. Metallic glasses

Metallic glasses are ferromagnetic amorphous alloys. Amorphous materials are characterised because of the absence of long-range atomic order, which can be observed in X-ray diffraction (XRD) experiments. The XRD patterns of amorphous materials show a broad peak because the light scatters in many directions as the atoms are randomly oriented. On the contrary, the atoms of a crystalline material are periodically arranged in a 3D space what makes the X-rays scatter only in certain directions that will cause high intensity narrower peaks[27].

The amorphous state is a metastable state, which means that it is not in its thermodynamic equilibrium. In other words, any solid usually possesses less free energy in its crystalline state than in the amorphous one. So, during the fabrication process of amorphous alloys the solidification rate has to be quick enough to avoid the atoms to reach the thermodynamic equilibrium state that would evolve into a crystalline 3D structure. The group directed by Pol Duwez synthesised the very first amorphous ferromagnetic alloy prepared in a laboratory in Cal Tech in 1960[28]. Nowadays, there are different ways to fabricate such kind of materials, as electrodeposition, vapour deposition, sputtering or melt spinning technique.

The melt spinning technique is the most used one. Although to achieve the amorphous state for a pure metal the needed cooling down velocity would be really high (on the order of 10^{10} $K \cdot s^{-1}$), to obtain amorphous alloys with a 80% of metallic elements (Fe, Co, Ni, Cr, Au) and 20% of metalloids (B, Si, C, P) the cooling down velocity needs to reach the order of 10^{6} $K \cdot s^{-1}$. The fabrication method and the melt spinning technique will be more extendedly explained in Chapter 2.

Amorphous ferromagnetic alloys present some interesting properties such as high elastic limit, good corrosion resistance, high electrical resistivity and as they are soft magnetic materials, low coercive fields, low losses and high permeability due to the lack of magnetocrystalline anisotropy.

As I previously mentioned, one of the most common applications for metallic glasses is their use as a sensor, which is a device that converts one determined energy form in another one. Generally, most of the applications of these metallic glasses are based on the influence that the magnetic field and the mechanical stress have in the magnetic permeability. This influence is directly related with the amorphous structure, the elastic properties, the magnetostriction (λ_s) and the induced anisotropy (K_U) in the material due to the fabrication process or by applying a later heat treatment under magnetic field and/or mechanical stress. Three are the intrinsic magnetic properties of the metallic glasses, the saturation magnetostriction M_s, the Curie temperature T_c, and the saturation magnetostriction λ_s[29].

1.2.2. Magnetostriction and magnetoelasticity

Magnetostriction is a property of the ferromagnetic materials that causes deformation when such are under the influence of an external applied magnetic field. This phenomenon was first noticed by James P. Joule in 1842 when observing a sample of iron[30].

In these materials each magnetic domain is deformed according to each own magnetization which in absence of external magnetic field, point along the direction defined by the magnetic anisotropy. Due to magnetostriction, when applying an external magnetic field to a ferromagnetic material not only the spontaneous magnetization rotates but also all the magnetic domains rotate to orientate along the same direction. As a consequence, a change in the material dimensions will occur, as the material will tend to minimise its internal energy. That local distortions caused by the magnetostriction will turn into a macroscopic deformation of the material. The kind of deformation (elongation or contraction) will vary depending on the sign of the saturation magnetostriction of the material as shown in Figure 1.2A.

On the contrary, the phenomena that takes place when a material suffers a change in its magnetic state caused by an applied mechanical

stress is called magnetoelastic effect, also known as inverse magnetostrictive effect. It is also known as Villari effect because it was Emilio Villari who observed it first in 1865. The magnetoelastic effect is described in Figure 1.2B.

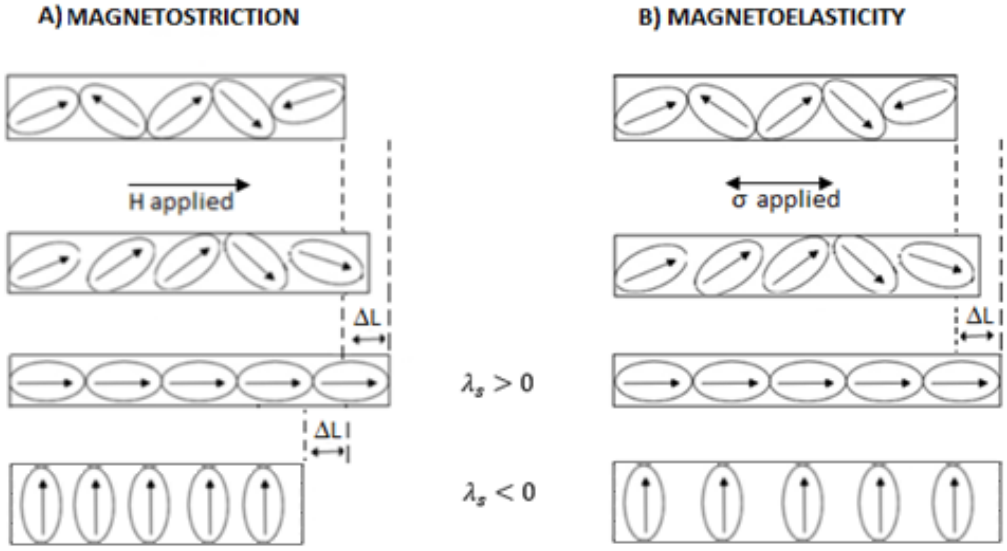

Figure 1.2. Magnetostrictive and magnetoelastic effects.

Summarising, a magnetostrictive material will elongate or contract under the action of an applied magnetic field and a magnetoelastic material will show a change in its magnetic state due to an applied mechanical stress. So, a magnetoelastic-magnetostrictive material is a ferromagnetic material which deforms continuously under the application of an external magnetic field.

The magnetoelastic effect is directly related with the magnetostriction or relative length variation of the material when it reaches the magnetic saturation. The magnetostriction of a ferromagnetic material is obtained by the following equation:

$$\lambda = \Delta L / L \qquad [1.1]$$

where ΔL is the deformation of the sample and L is the initial length of the sample.

The maximum deformation attained at magnetic saturation λ_s, is called saturation magnetostriction and it is a characteristic of the material. It is generally small of about some parts per million, as for example for iron, nickel or cobalt that is of 9 ppm, -40 ppm and -60 ppm respectively. There are some exceptions for the case of rare earth metals alloyed with iron, as the case of the Terfenol-D, containing dysprosium and terbium, which can reach values of saturation magnetostriction up to 2000 ppm. Depending on the material, the deformation manifests as an expansion or as a contraction, as it can be observed in Figure 1.5, which is reflected in the sign of the magnetostriction constant.

If the magnetostriction is positive ($\lambda s > 0$), the effect of a tensile stress is to favour the magnetization along the direction of the applied stress. The material is easier to magnetize in that direction and the permeability is increased. Therefore, the effect of a tensile stress in a material with positive magnetostriction is to favour an easy axis for the magnetization in the direction of the applied stress. However, if the magnetostriction is negative ($\lambda s < 0$), the stress favours magnetization along the perpendicular direction of its application. It is necessary a stronger magnetic field to magnetize the sample, that is, the magnetic permeability is reduced. Therefore, the effect of a tensile stress in a material with negative magnetostriction is to create an easy plane perpendicular to the direction of the applied stress[31].

The clearest and most interesting manifestation of magnetoelasticity is the dependence of the elastic constants with the external applied magnetic field, in particular for the Young modulus E. The variation of the Young modulus with the externally applied magnetic field is known as "*ΔE effect*" which can be calculated by the following equation:

$$\Delta E\ (\%) = \frac{E_s - E_{min}}{E_s} \cdot 100 \qquad [1.2]$$

where E_s is the Young modulus at the magnetic saturation state and E_{min} is the minimum value of the Young modulus. In normal

ferromagnetic materials, as nickel or iron, the ΔE *effect* is very small, 18% and 0.4% respectively, but it is very large in magnetostrictive metallic glasses (easily up to a 50%). Those materials with a high ΔE *effect* value will be useful for sensor applications as the elastic energy would be easily converted into magnetic energy and vice versa[32]. An easy way to determine quantitatively this effect is to use the so-called magnetoelastic resonance method.

1.2.3. The magnetoelastic resonance

The magnetoelastic resonance measurement method consists, as can be observed in Figure 1.1, in exciting a magnetoelastic material by a time varying magnetic field. In response, due to the magnetostrictive effect, the material would convert the magnetic energy into elastic energy, generating the propagation of elastic waves through the material. Those strain waves will cause the mechanical vibration of the material, which through the magnetoelastic effect, would in turn generate a time varying magnetic flux due to magnetization oscillations that can be detected by a pick-up coil. Under specific boundary conditions, the propagated waves become stationary, and if their frequency is such that the wavelength of the mechanical oscillation matches the dimension of the sample, the magnetoelastic resonance will take place. At this resonance frequency, large strain and maximum magnetization oscillation are induced and the apparent susceptibility of the material reaches the maximum. Therefore, by changing the excitation frequency of the applied external magnetic field (or bias) we could reach a particular frequency at which the magnetoelastic resonance takes place[33].

Theoretically, the resonance frequency for a sample vibrating with free ends under an applied magnetic field is given by the equation:

$$f_r^n = \frac{n}{2L}\sqrt{\frac{E(H)}{\rho(1-v^2)}} \qquad [1.3]$$

where n is the resonance mode number (harmonic), L is the length of the ribbon, ρ is the density of the metallic alloy, υ is the Poisson ratio and $E(H)$ is the magnetic field dependant Young modulus.

By using the magnetoelastic resonance method this resonance frequency is in practice easy to be measured and in most applications only the fundamental resonant frequency $f_0^1\ (n = 1)$ is considered because of the higher signal amplitude and the lower frequency, as it can be noticed in Figure 1.3.

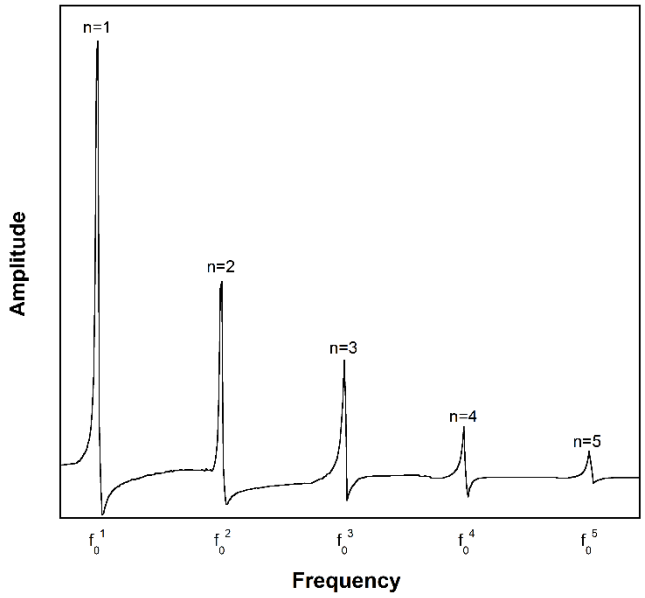

Figure 1.3. Curve obtained from the magnetoelastic resonance method.

From the first longitudinal vibration mode, for instance the Young modulus can be calculated as:

$$E(H) = \rho(2Lf_r)^2 \qquad [1.4]$$

By using this measurement method, other two important parameters can be calculated from the first fundamental resonant mode: the magnetoelastic coupling coefficient, k, and the quality factor, Q.

As I previously mentioned, in ferromagnetic materials there is a coupling between magnetic and elastic properties. So, there is an effective energy interchange from magnetic to elastic, and vice versa. The parameter that accounts for that energy interchange is known as magnetoelastic coupling coefficient, k, and in the case of a ribbon, it can be calculated by the given expression:

$$k^2 = \frac{\pi^2}{8}\left[1 - \left(\frac{f_r}{f_a}\right)^2\right] \qquad [1.5]$$

where f_r is the resonance frequency and f_a the antiresonance frequency (or signal zero value).

On the other hand, Q is the mechanical quality factor that quantifies the energy losses of the resonator, giving us information about how good the resonance curve is on the efficiency of the energy conversion. Consequently, whereas high Q values turn into a sharper and narrower resonance curve indicating a low rate of energy losses, small Q values give rise to a wider bandwidth and a higher rate of energy losses. Q factor can be estimated by the following relationship:

$$Q = \frac{f_r}{\Delta f} \qquad [1.6]$$

where f_r is the resonance frequency, and Δf is the bandwidth measured at $A_{max}/\sqrt{2}$, being A_{max} the maximum amplitude.

All the mentioned parameters, $E\ (H)$, $k\ (H)$ and $Q\ (H)$, measured as a function of the applied magnetic field, fully characterise the magnetoelastic behaviour of a magnetostrictive/magnetoelastic material.

1.3. Functionalization of the magnetoelastic resonant platforms

As I have previously explained, the magnetoelastic resonance method allows us to magnetically excite the magnetostrictive/magnetoelastic material, magnetically detect the generated flux and determine its resonant frequency. This resonance frequency shifts in response to different external physical parameters including pressure[34], magnetic field[35,36] temperature[37], stress, flow velocity[38], liquid viscosity[39], and mass loading. Equation [1.3] describes the resonant frequency as a function of mechanical properties. Nevertheless, the model can be extended to include the dependence to some external parameters by introducing different variables.

For example, a magnetoelastic sensor can respond to changes in ambient pressure. To enhance the pressure sensitivity it is fundamental to create out-of-plane vertical vibrations by appropriately bending the sensor. The idea is to induce stress on the magnetoelastic materials by which the magnetoelastic energy is coupled to create a basal plane vibration. So, the resonant frequency shift of the bent sensor as:

$$\Delta f = f - f_0 = -\frac{1}{\sqrt{3}}\frac{v^2}{1-v^2}\frac{m_g u}{k_B T d \rho_s} P \qquad [1.7]$$

where P is the pressure, d is the sensor thickness, u is the maximum vibration amplitude, v is the Poisson ratio, T is the temperature, k_B is the Boltzmann's constant and m_s is the mass of the acting gas. This equation indicates that the resonant frequency decreases with the increasing pressure and it was used to measure the atmospheric pressure[34].

For the case of the field and temperature dependant resonant frequency, we can consider that the elastic and magnetic properties of the material could be affected by the temperature. So, the resonant frequency will in this case be expressed as:

$$f_o\,(T,H) = \frac{1}{2L(T)}\sqrt{\frac{E_S(T)}{\rho_S(T)}}\left(1+\frac{9\lambda_s(T)H^2E_S(T)}{M_S(T)H_k^3(T)}\right)^{-1/2} \qquad [1.8]$$

This equation is more extendedly described in [35] and [36]. According to equation [1.8], the resonant frequency shift can be used to directly measure the temperature[37]. Thus, when working as a temperature sensor, an appropriate field H can be applied to the material to yield the optimum temperature sensitivity; for other sensing applications, the value of H can be chosen so the sensor has no temperature dependency.

A magnetoelastic sensor can also be used to measure liquid fluid flow rates since the flowing liquid creates a damping force, proportional to the flow rate, on the sensor surface and causes a shift in the sensor resonant frequency. The resonant frequency decreases quadratically at laminar liquid flow and increases again when the liquid switches from laminar to turbulent flow[38]. Other application for these magnetoelastic resonant platforms is to determine viscosities[39]. Among the different parameters that define the state of lubricant oil, viscosity is one of the most important. In this case, the measurements were performed using different commercial oils with viscosities ranging from 32 to 326 cSt.

In these previous examples, those physical parameters (pressure, temperature, viscosity, etc.) have been measured by the magnetoelastic resonant platform itself. However, in other cases, such as for chemical or biological sensing applications a responsive layer is needed to cover the magnetoelastic resonant platform in order to selectively detect the target molecule.

If a coating mass Δm is uniformly applied on the sensor surface, the density ρ can be replaced by $(m_s+\Delta m)/Ad$ where m_s is the mass of the sensor, A is the surface area, and d is the thickness of the sensor. This will yield a new fundamental resonant frequency that depends on the initial resonant frequency f_0 of the uncoated magnetoelastic material and on the loading (added) mass. The new equation for this resonance will be:

$$f = f_0\sqrt{\frac{1}{1+\Delta m/m_s}} \qquad [1.9]$$

In a general way, the displacement of the resonance curve of an uncoated resonant platform and a coated one can be observed in Figure 1.4. The new resonant frequency will always shift to lower values as the loading mass increases.

Considering this mass loading effect, if the resonant platform is coated by a mass-changing chemically or biologically responsive layer, the developed sensor will be able to monitor chemical or biological analyte concentrations. This active layer can provide a specific detection for the target molecule and a rapid response. Depending on the target parameter[17] (pH[18], humidity[19]) or molecule (a gas[22], a protein[23], a bacteria[25]), the nature of the active layer will be different. Active layers can be performed with different kinds of materials such as polymers or inorganic compounds, among others.

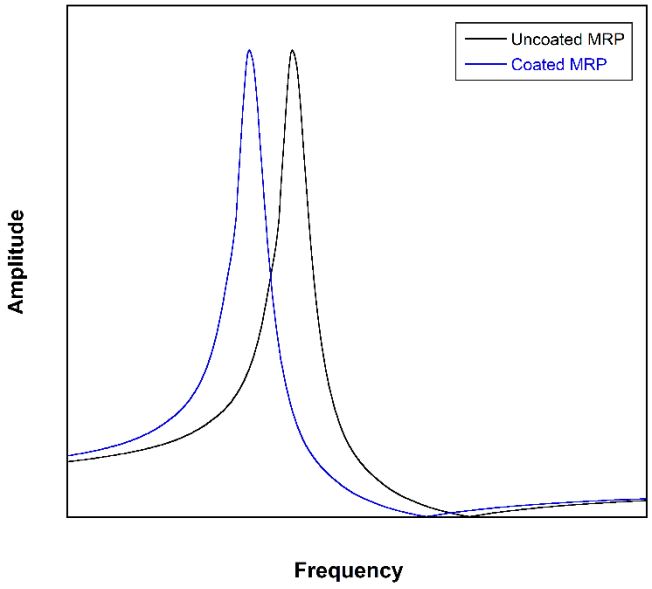

Figure 1.4. Shift in the resonance frequency of a magnetoelastic resonant platform due to a mass deposition.

1.3.1. Polymers

The word polymer comes from two Greek words: *poly-*, which means 'many' and *–mer,* from *meros,* meaning 'part' or 'member'. Hence, a polymer is a large molecule, usually called macromolecule, which means that it is a molecule of high relative molecular mass. The structure of a polymer essentially comprises the multiple repetition of units of low relative molecular mass. There are different ways to classify the polymers depending on their origin (natural or biological polymers and synthetic ones), on the polymer structure (linear, branched, cross-linked), or processability, among others.

Nowadays, a large number of polymers is widely used in various applications due to their versatile properties. This is mainly because they are available in a wide variety of compositions and forms (solid, fibre, film, gels), their properties can be tailored during the fabrication processes or by synthesis methods, they are easy to produce as well as being cost effective, and they can be fabricated into complex shapes and structures.

Polymer coatings continue to be used in even more increasingly diverse applications and sectors. From simple barrier coatings to elaborated nanotechnology based composites, polymers offer a bastion of functionalities for their underlying hosts. The attraction of these materials for sensing applications relies on their flexibility, biocompatibility and ease of deposition onto a substrate. In the case of amorphous magnetoelastic materials, probably the most important property of the polymer coating is the corrosion protection that they confer to the whole sensor system[40]. The selection of the optimal polymer coating has to be made according to several criteria. Polymer should be easily and reproducibly deposited onto the sensor surface. It must be resistant against oxidative processes at the detecting conditions; it will also serve as a protective layer against aggressive environments. In addition, they should ideally provide a rapid and linearly related response with the analyte concentration.

By using magnetoelastic materials, sensors have been developed for different purposes such as environmental contaminant detection or biomedical applications. A sensor coated with a copolymer formed by acrylamide and isooctylacrylate polymers has been reported to sense carbon dioxide[21]. A similar copolymer based on acrylic acid and isooctylacrylate was used to fabricate a pH sensor[41]. Additionally, a pH responsive polymer coating has been used to fabricate a sensor for organophosphate pesticides using the enzyme organophosphate hydrolase onto the polymer coating. The hydrolase catalyses the hydrolysis of the organophosphates changing the pH of the polymer hydrogel, which will swell or shrink producing a change on the resonant frequency of the whole system[42].

In the field of biomedicine, a sensitive polymer coated magnetoelastic sensor has been developed to in vivo measure the pH[43]. Other kind of biomedical sensors have been developed to sense glucose. This was fabricated by coimmobilizing glucose oxidase into a pH sensitive polymer coated magnetoelastic material. When the glucose is oxidised it produces gluconic acid inducing the shrinking of the pH sensitive polymer, which in turn decreases the polymer mass and therefore changing the response of the magnetoelastic material[44].

1.3.2. Inorganic compounds

Some inorganic materials have also been used as covering active layers for the magnetoelastic ribbons. Nanostructured materials are being intensively studied for applications in many different nanoscale functional devices. Nanostructure oxides, as TiO_2[45], have been used to build humidity sensors on a commercial Metglas ribbon. In this case, as the humidity increases, water vapour is absorbed into the oxide layer, increasing the effective mass on the sensor and decreasing the resonant frequency of the sensor. Similar results were obtained for alumina (Al_2O_3) covered samples[46].

Other inorganic materials, which present good properties to be used as active layers, are zeolites. Zeolites are porous crystalline aluminosilicates: silicon and aluminium combined with oxygen, originating a wide range of chains, rings, layers and three-dimensional arrays. Despite all the zeolites, share the same basic chemical composition the different arrangements of atoms and molecules lead to structures with different physical and chemical properties. These materials have found a wide range of applications as molecular sieves, catalysis, mechanical reinforcement, medical and biological applications, sensors, filtration membranes and energy storage, among others. The many applications are mainly related to their high surface area, excellent thermal/hydrothermal stability, high shape-selectivity and superior ion-exchange ability[47].

For their applications with sensing purposes, the aluminosilicate materials are constructed from linked tetrahedral joined through shared oxygen atoms forming three-dimensional frameworks that define a regular system of voids and channels of molecular dimensions. Depending on the size and shape of those channels, the zeolite will actuate as a molecular sieve to preferentially adsorb certain molecules and to exclude others. This selective detection applied to sense a wide range of volatile organic compounds (VOCs) has been reported for three different kinds of zeolites: MFI, LTA or FAU[48]. Other experiments also performed using magnetoelastic resonance methods allowed the determination of zeolites Young modulus and their flexibility [49,50].

1.4. Objectives and structure of this thesis

This work has as a general objective the development of sensors based on magnetoelastic resonant platforms. With this purpose in mind, magnetoelastic materials in the form of ribbons will be fabricated and characterized. The magnetoelastic amorphous alloys will be functionalized with different active materials in order to use them for chemical or biological detection purposes. These active materials should be selective to the target analyte changing the mass of the sensing

platform to allow us to measure the shift promoted in the resonant frequency of the magnetoelastic material. The deposition process of each coating material has to be optimised, a task for which the magnetoelastic resonance will be also very useful. The thesis is divided in different chapters related with the diverse materials used as active layers for the development of the magnetoelastic sensors.

Chapter 2 will focus on the experimental part of the thesis. To start, the fabrication process of the metallic glasses and subsequent characterization of the most important parameters will be explained. Additionally, magnetic and magnetoelastic characterization of the fabricated metallic alloys was performed by measuring the magnetostriction parameters, λ_s, the ΔE *effect* or the quality factor, Q. During the development of the thesis, the importance of the corrosion resistance has demonstrated to be a very important factor that should be taken into account when the alloy is going to be coated with a certain type of materials or when a later treatment needs special conditions to be carried out. Due to this, the corrosion behaviour of some previously fabricated ribbons was analysed in order to be able to fabricate other new magnetoelastic ribbons with higher corrosion resistance that will be also presented and studied in this chapter. Finally, the characterization techniques employed for the characterization of the active layer deposited onto the magnetoelastic materials. Functionalization of the previously fabricated resonant platforms with polymers or organic compounds is needed to use them for sensing applications so the characterization of the deposited layers must be performed.

Chapter 3 will be focused on monitoring the process of the functionalization of a MRP with the polymer polystyrene. Moreover, the main parameters affecting the sensing experiments will be introduced as they will be useful for this and next chapters. Polystyrene will be deposited onto two different composition alloys using the same deposition process, dip coating, but varying the solvent of the polymer to enhance the final deposited layer properties. A final comparison between the theoretical predictions for the deposited mass and the experimental results will also be presented. During the polymer deposition experiments, a nonlinear resonant frequency against

deposited mass behaviour has been observed, which made us to look to the up to date accepted theory that predicted a linear behaviour for small-deposited mass quantities.

The next two chapters will be focused on the coating process with inorganic materials. The work presented in those two chapters (4 and 5) has been developed at the University of Patras (Greece), in the Department of Chemical Engineering, in the Department of Material Science and in the Foundation of Research and Technology (Forth ICE-HT). Two different materials will be deposited onto magnetoelastic materials: zinc oxide, ZnO, with biological detection purposes, and zeolites for gas detection purposes.

Chapter 4 will focus onto the biological sensing process and will study several methods to functionalize the magnetoelastic ribbon metallic surface with zinc oxide. In this case, the magnetoelastic material is going to be a commercial one, Metglas 2826MB. By analysing and choosing the best functionalization procedure, ZnO will be deposited as nanosized nanoparticles to fabricate a thin film. By performing magnetoelastic resonance measurements, I will determine the elastic modulus of those final deposited zinc oxide thin films. Finally, some bio-detection experiments concerning hemoglobin and H_2O_2 will be carried out.

In Chapter 5, xylene detection will be performed with zeolite coated homemade magnetoelastic resonant platforms. The main objective of this chapter is to compare the obtained results with some previously ones, obtained when using as resonant platform the commercial Metglas 2826MB one. Therefore, I will compare the sensitivity of both systems and discuss the difference in terms of the resonant platform properties.

Finally, in Chapter 6, the conclusions derived from this work will be presented and open perspectives will be pointed out.

References

[1] Anton F.P. Van Putten, "Electronic Measurement Systems. Theory & Practice. [Chapter 6 Transducers]", Second Edition, Editorial: Institute of Physics Publishing (1996) 205-207. ISBN: 978-0750303408.

[2] http://www.testbourne.com/quartz-sensor-crystals (03/2017); http://openqcm.com/ (03/2017).

[3] G.Z.Z. Sauerbrey, "Use of quartz vibrator for weighing thin films on a microbalance", Z. Physics 155 (1959) 206-212. DOI: 10.1007/BF01337937.

[4] B.A. Cavicacute, G.L. Hayward and M. Thompson, "Acoustic waves and the study of biochemical macromolecules and cells at the sensor-liquid interface", Analyst 124 (1999) 1405-1420. DOI: 10.1039/A903236C.

[5] Y. Yao, H. Zhang, J. Sun, W. Ma, L. Li, W. Li and J. Du, "Novel QCM humidity sensors using stacked black phosphorous nanosheets as sensing film", Sensors and Actuators B: Chemical 244 (2017) 259-264. DOI: 10.1016/j.snb.2017.01.010.

[6] N.C. Speller, N. Siraj, K.S. McCarter, S. Vaughan and I.M. Warner, "QCM virtual sensor array: Vapor identification and molecular weight approximation", Sensors and Actuators B: Chemical 246 (2017) 952-960. DOI: 10.1016/j.snb.2017.02.042.

[7] S. Atay, K. Piskin, F. Yilmaz, C. Çakir, H. Yavuz and A. Denizli, "Quartz crystal microbalance based biosensors for detecting highly metastatic breast cancer cells via their transferrin receptors", Analytical Methods 8 (2016) 153-161. DOI: 10.1039/C5AY02898A.

[8] J.R. Barnes, R.J. Stephenson, M.E. Welland, C. Gerber and J.K. Gimzewski, "Photothermal Spectroscopy with Femtojoule Sensitivity Using a Micromechanical Device", Nature 372 (1994) 79-81. DOI: 10.1038/372079a0.

[9] T. Thundat and R.J. Warmack, "Thermal and ambient-induced deflections of scanning force microscope cantilever", Applied Physics Letters 64 (1994) 2894-2896. DOI: 10.1063/1.111407.

[10] S. Li, L. Orona, Z. Li and Y. Cheng, "Biosensor based on magnetostrictive microcantilever", Applied Physics Letters 88 (2006) 073507. DOI: 10.1063/1.2174092.

[11] L. Zhao, Y. Hu, T. Wang, J. Ding, X. Liu, Y. Zhao and Z. Jiang, "A MEMs resonant sensor to measure fluid density and viscosity under flexural and torsional vibrating modes", Sensors 16 (6) (2016) 630-645. DOI: 10.3390/s16060830.

[12] D. Lee, O. Zandieh, S. Kim, S. Jeon and T. Thundat, "Sensitive and selective detection of hydrocarbon/water vapor mixtures with a nanoporous silicon microcantilever", Sensors and Actuators B: Chemical 206 (2015) 84-89. DOI: 10.1016/j.snb.2014.09.036.

[13] K. Zhang, L. Zhang, L. Fu, S. Li, H. Chen and Z.Y. Cheng, "Magnetostrictive resonators as sensors and actuators", Sensors and actuators A: Physical 200 (2013) 2-10. DOI: 10.1016/j.sna.2012.12.013.

[14] C.A. Grimes, S.C. Roy, S. Rani and Q. Cai, "Theory, instrumentation and applications of magnetoelastic resonance sensors: a review", Sensors 11 (3) (2011) 2809-2844. DOI: 10.3390/s110302809.

[15] C.A. Grimes, D. Kouzoudis and C. Mungle, "Simultaneous measurement of liquid density and viscosity using remote query magnetoelastic sensors", Review of Scientific Instruments 71 (2000) 3822-3824. DOI: 10.1063/1.1315352.

[16] P.G. Stoyanov and C.A. Grimes, "A remote query magnetostrictive viscosity sensor", Sensors and Actuators A: Physical 80 (2000) 8-14.

[17] Q.Y. Cai and C.A. Grimes, "A remote query magnetoelastic pH sensor", Sensors and Actuators B: Chemical 71, (2000) 112-117. DOI: 10.1016/S0924-4247(99)00288-5.

[18] C. Schanzenbach, D. Ilver, J. Blomgren, C. Jonasson, C. Johansson, A. Krozer, L. Ye and B. Rustas, "Preparation and characterisation of a sensing system for wireless pH measurements in vivo, in a rumen of a cow", Sensors and Actuator B: Chemical 242 (2017) 637-644. DOI: 10.1016/j.snb.2016.11.089.

[19] M.K. Jain, S. Schmidt, K.G. Ong, C. Mungle and C.A. Grimes, "Magnetoacoustic remote query temperature and humidity sensor", Smart Materials and Structures 9 (2000) 502-510. DOI: 10.1088/0964-1726/9/4/314.

[20] Q.Y. Cai, M.K. Jain and C.A. Grimes, "A wireless, remote query ammonia sensor", Sensors and Actuators B: Chemical 77 (2001) 614-619. DOI: 10.1016/S0925-4005(01)00766-3.

[21] Q.Y. Cai, A. Cammers-Goodwin and C.A. Grimes, "A wireless, remote query magnetoelastic CO_2 sensor", Journal of Environmental Monitoring 2 (6) (2000) 556-560. DOI: 10.1039/B004929H.

[22] T. Baimpos, L. Gora, V. Nikolakis and D. Kouzoudis, "Selective detection of hazardous VOCs using zeolite/metglas composite sensors", Sensors and Actuators A: Physical 186 (2012) 21-31. DOI: 10.1016/j.sna.2011.12.030.

[23] P. Pang, Y. Zhang, S. Ge, Q.Y. Cai and C.A. Grimes, "Determination of glucose using bioenzyme layered assembly magnetoelastic sensing device", Sensors and Actuators B: Chemical 136 (2009) 310-314. DOI: 10.1016/j.snb.2008.11.044.

[24] A.L. Possan, C. Menti, M. Beltrami, A.D. Santos and F.P. Missel, "Effect of surface roughness on performance of magnetoelastic biosensors for the detection of *Escherichia coli*", Materials Science and Engineering: C 58 (2016) 541-547. DOI: 10.1016/j.msec.2015.08.029.

[25] I. Chen, S. HoriwAKA, k. Bryant, R. Riggs, B.A. Chin and J.M. Barbaree, "Bacterial assessment of phage magnetoelastic sensors for *Salmonella enterica Typhimurium* detection in chicken meat", Food Control 71 (2017) 273-278. DOI: 10.1016/j.foodcont.2016.07.003.

[26] Jiehui Wan "Development and study of phage coated magnetoelastic biosensors for the detection of *Bacillus Anthracis Sterne spores*" PhD dissertation, Graduate Faculty of Auburn University, 2008.

[27] B.D. Cullity, "Elements of X Ray Diffraction" Addison-Wesley Publishing Company (1956) 101-102 (Figure 3-18). Library of Congress Catalog No 56-10137.

[28] P. Duwez and S.C.H. Lin, "Amorphous Ferromagnetic Phase in Iron-Carbon-Phosphorus alloys" Journal of Applied Physics 38 (1967) 4096-4097. DOI: 10.1063/1.1709084.

[29] J. Gutiérrez, "Propiedades magnéticas y magnetoelásticas de nuevas aleaciones amorfas de interés tecnológico", PhD dissertation, Universidad del País Vasco/Euskal Herriko Unibertsitatea (UPV/EHU), 1992.

[30] J.P. Joule, "On a new class of magnetic forces" The Annals of Electricity, Magnetism and Chemistry 8 (1842) 219-224.

[31] A. García-Arribas, J.M. Barandiarán and J. Gutiérrez, "Magnetoelastic sensors" in Encyclopedia of Sensors vol. X, 1-21. Edited by C.A. Grimes, E.C. Dickey and M.V. Pishko. American Scientific Publishers: California, USA (2006). ISBN: 1-58883-056-X.

[32] Lasheras, "Magnetoelectric metallic glass/polymer laminated composites: from fabrication to applications", PhD dissertation, Universidad del País Vasco/Euskal Herriko Unibertsitatea (UPV/EHU), 2015.

[33] Garcia-Arribas, J. Gutiérrez, G.V. Kurlyandskaya, J.M. Barandiarán, A. Svalov, E. Fernández, A. Lasheras, D. de Cos and I. Bravo-Imaz, "Sensor applications of soft magnetic materials based on magneto-impedance, magneto-elastic resonance and magneto-electricity", Sensors 14 (2014) 7602-7624. DOI: 10.3390/s140507602.

[34] D. Kouzoudis and C.A. Grimes, "The frequency response of magnetoelastic sensor to stress and atmospheric pressure" Smart Materials and Structures 9 (2000) 885-889. DOI: 10.1088/0964-1726/9/6/320.

[35] C.A. Grimes, C.S. Mungle, K. Zeng, M.K. Jain, W.R. Dreschel, M. Paulose and K.G. Ong, "Wireless magnetoelastic resonance sensors: a critical review" Sensors 2 (2002) 294-313. DOI: 10.3390/s20700294.

[36] J.D. Livinston, "Magnetomechanical properties of amorphous metals", Physica Status Solidi A 70 (1982) 591-596. DOI: 10.1002/pssa.2210700228.

[37] C.S. Mungle, C.A. Grimes and W.R. Dreschel, "Magnetic field tuning of the frequency temperature response of a magnetoelastic sensor", Sensors and Actuators A: Physical 101 (2002) 143-149. DOI: 10.1016/S0924-4247(02)00179-6.

[38] D. Kouzoudis and C.A. Grimes, "Remote query fluid-flow velocity measurement using magnetoelastic thick-film sensor", Journal of Applied Physics 87 (9) (2000) 6301-6303. DOI: 10.1063/1.372686.

[39] I. Bravo-Imaz, A. García-Arribas, E. Gorrotxategi, A. Arnaiz and J.M. Barandiarán, "Magnetoelastic viscosity sensor for on-line status assessment of lubricant oils", IEEE Transactions on Magnetics 4 (2013) 113-116. DOI: 10.1109/TMAG.2012.2217117.

[40] J.R. Smith and D.A. Lamprou, "Polymer coating for biomedical applications: a review" Transactions of the IMF, The International Journal of Surface Engineering and Coatings 92(1) (2014) 9-19. DOI: 10.1179/0020296713Z.000000000157.

[41] Q.Y. Cai, and C.A. Grimes, "A remote query magnetoelastic pH sensor", Sensors and Actuators B: Chemical 71 (2000) 112-117. DOI: 10.1016/S0925-4005(00)00599-2.

[42] M. Zourob, K.G. Ong, K. Zeng, F. Mouffouk and C.A. Grimes, "A wireless magnetoelastic biosensor for the direct detection of organophosphorus pesticides", Analyst 132 (2007) 338-343. DOI: 10.1039/B616035B.

[43] Schanzenbach, S. Ilver, J. Blomgren, C. Jonasson, C. Johansson, A. Krozer, L. Ye and B.O. Rustas, "Preparation and characterisation of a sensing system for wireless pH measurements in

vivo, in a rumen of a cow", Sensors and Actuators B: Chemical 242 (2017) 637-644. DOI: 10.1016/j.snb.2016.11.089.

[44] Q. Cai, K. Zeng, C. Ruan, T.A. Sedai and C.A. Grimes, "A wireless, remote query glucose biosensor based on a pH sensitive polymer", Analytical Chemistry 76 (2004) 4038-4043. DOI: 10.1021/ac0498516.

[45] C.A. Grimes, D. Kouzoudis, E.C. Dickey, D. Qian, M.A. Anderson, R. Shahidian, M. Lindsey and L. Green, "Magnetoelastic sensor in combination with nanometer-scale honeycombed thin film ceramic TiO_2 for remote query measurement of humidity", Journal of Applied Physics 87 (9) (2000) 5341-5343. DOI: 10.1063/1.373341.

[46] M.K. Jain, S. Schmidt, K.G. Ong, C. Mungle and C.A. Grimes, "Magnetoacoustic remote query temperature and humidity sensors", Smart Materials and Structures 9 (2000) 502-510. DOI: 10.1088/0964-1726/9/4/314.

[47] A.C. Lopes, P. Martins and S. Lanceros-Mendez, "Aluminosilicate and aluminosilicate based polymer composites: Present status, applications and future trends", Progress in Surface Science 89 (2014) 239-277. DOI: 10.1016/j.progsurf.2014.08.002.

[48] T. Baimpos, L. Gora, V. Nikolakis and D. Kouzoudis, "Selective detection of hazardous VOCs using zeolite/Metglas composite sensors", Sensors and Actuators A: Physical 186 (2012) 21-31. DOI: 10.1016/j.sna.2011.12.030.

[49] T. Baimpos, D. Kouzoudis, L. Gora and V. Nikolakis, "Are zeolite flexible?" Chemistry of Materials 23 (6) (2011) 1347-1349. DOI: 10.1021/cm1025206.

[50] T. Baimpos, V. Nikolakis and D. Kouzoudis, "A new method for measuring the adsorption induced stresses of zeolite films using magnetoelastic sensors", Journal of Membrane Science 390-391 (2012) 130-140. DOI: 10.1016/j.memsci.2011.11.031.

2. Experimental part:

Materials and methods

This second chapter describes first the procedure employed to fabricate the magnetoelastic ferromagnetic amorphous ribbons by using the melt spinning technique. These homemade alloys were magnetic and magnetoelastically characterized and corrosion resistance measurements were also performed with some selected samples compositions. Corrosion resistance has been proved to be an important factor that must be taken into account when trying to coat the magnetoelastic ribbons with the active layer, as one of the main problems observed was related with the oxidation of the samples in certain liquid media. Afterwards, the parameters that affect the sensing ability of the resonant platforms will be explained, especially for chemical and biological detection purposes.

2.1. The Magnetoelastic Resonant Platforms (MRPs)

Ferromagnetic amorphous alloys with five different compositions have been used as magnetoelastic resonant platforms throughout this work. Those compositions and properties of the ribbons depended on the application of the developed system.

The first alloy was a commercially available material. This is the Metglas 2826MB3 purchased from Hitachi Metals Europe GmbH (Dusseldorf, Germany). It is an iron-nickel based alloy of composition $Fe_{40}Ni_{38}Mo_4B_{18}$, with medium saturation induction, low magnetostriction and higher corrosion resistance, sold for applications in field sensors, shielding applications, high frequency cores or magnetomechanical sensors[1]. This alloy was used as a reference material for the corrosion resistance measurements and also for the measurements made for biodetection purposes.

The iron-cobalt and iron-nickel rich alloys used were fabricated by Dr. Andoni Lasheras during his PhD thesis work. Those compositions were chosen due to their expected low anisotropy field, high magnetization value (which implies a high magnetic susceptibility) and due to their relative high saturation magnetostriction. Metallic glasses were fabricated by the melt spinning technique. The alloys prepared by Dr. Andoni Lasheras were fabricated at the Institute of Metal Physics of the Ural Federal University (Russia). The compositions of the three alloys employed were $Fe_{64}Co_{21}B_{15}$ (used for gas sensing applications), $Fe_{64}Co_{17}Si_{6.6}B_{12.4}$ (used for the first studies depositing polymer) and $Fe_{55}Ni_{25}B_{20}$ (used for the corrosion resistance measurements).

The last alloy of composition $Fe_{54}Ni_{24}Cr_2Si_{10}B_{10}$ was specially fabricated for this PhD thesis work in order to improve the corrosion resistance of the magnetoelastic materials, while keeping good magnetic and magnetoelastic properties of the material in order to be able to be used for possible sensing applications.

2.1.1. Fabrication of metallic glasses

The chromium-containing alloy which was the one fabricated specially for this PhD thesis work was fabricated at the laboratories located at BCMaterials, at the University of the Basque Country and at the University of Oviedo. First of all the metal constituents were cut (at BCMaterials) following the corresponding stoichiometric calculations in order to obtain the desired alloy. The metals were purchased from Alfa Aesar, in rod form for iron (99.95%), nickel (99.5%), cobalt (99.95%) and silicon (99.99%), and in pieces in the case of boron (99.5%) and chromium (99.99%). The needed quantities were cut with a Desktop Crystal Cutter: Model: CU-01 (Crystal systems corporation, Japan) that can be seen in Figure 2.1.

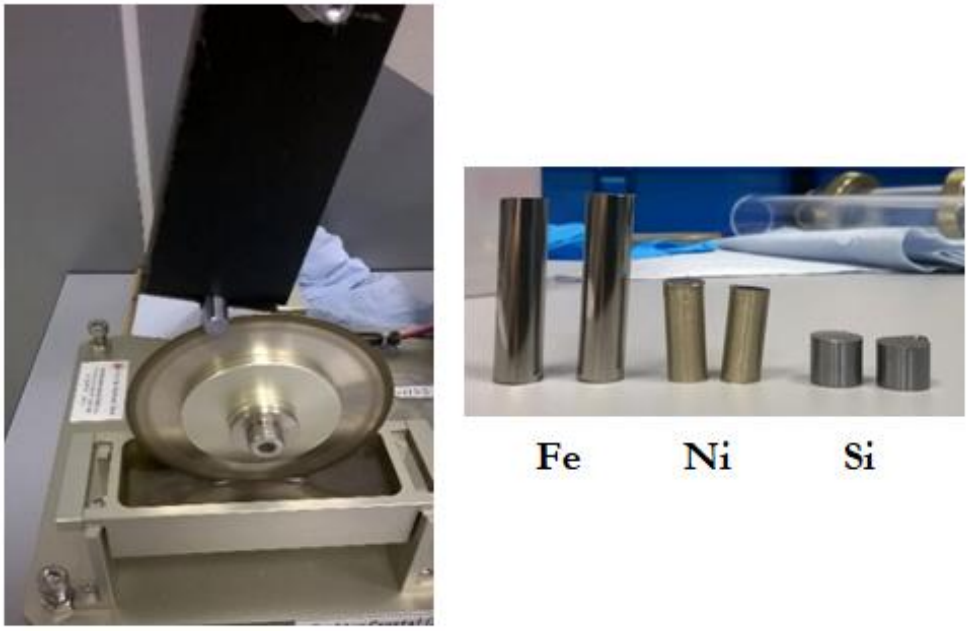

Figure 2.1. First step of the fabrication process: cutting of the metallic constituents.

The next step of the fabrication process consisted on fabricating what is known as the "master" alloy, prior to the final amorphous ribbon shape fabrication. For this purpose, an induction furnace (Induret Compact, Reitel) was employed and 18 g of each composition were prepared (at the University of the Basque Country). The induction furnace

consists of two main spaces. The upper space contains a thick helicoidal coil, that is refrigerated with water and surrounds a ceramic crucible; at the lower part where a copper mould will be placed. The whole instrument is presented in Figure 2.2. The heating process happened due to the dissipative Joule effect caused by the induction of Eddy currents in the metals. These currents arise from a high frequency electric current circulating through the coil that generated so a high frequency electromagnetic field acting directly in the metallic (and so conductive) sample. In order to favour the melting process, the elements were carefully placed inside the ceramic crucible as compact as possible at the centre. This ceramic crucible has a hole below which will keep closed with a stopper during the melting process. Inside this stopper, the thermocouple was placed to monitor and control the temperature.

Figure 2.2. Second step of the fabrication process: fabricating the alloy.

Once the elements were properly place, the chambers were closed and vacuum was made inside the chambers by using the Venturi effect. Previously, the chambers must be purged with argon several times in order to clean the atmosphere as better as possible.

The melting process could be directly visualised through a window located above the crucible (Figure 2.3). When the alloy was completely melted and homogeneous (approximately at 1200 ℃ for the prepared

alloys), the crucible stopper was elevated opening the hole and an argon pressure of 3 – 4 bar was suddenly introduced, forcing the melted alloy fall down to the copper mould. The obtained ingot inside the copper mould can be observed in Figure 2.3. The melting process was repeated twice in order to obtain totally homogeneous alloys.

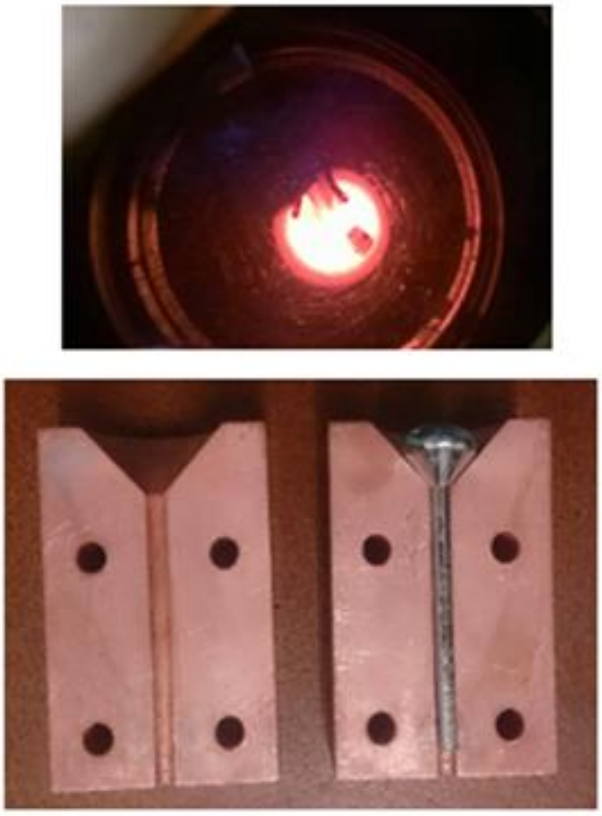

Figure 2.3. The melted alloy and the obtained ingot inside the copper mould.

The third step of the process, once the ingots of the alloys were fabricated, was to fabricate the amorphous ribbons by the melt spinning technique. The samples were fabricated at the University of Oviedo, under the supervision of Dr. Javier Carrizo. The melt spinning system employed is shown in Figure 2.4: as it can be observed the melt spinning technique consists of a copper wheel, which rotates at high speed. Pieces of the alloys were introduced into a quartz tube which was located above the wheel at a certain distance. The whole system was left under vacuum reaching $5 \cdot 10^{-5}$ mbar, and then the melting of the alloys started. As aforementioned, by applying a high frequency electromagnetic field, the

induced eddy currents were able to melt the alloy. The diameter of the outlet hole of the quartz tube, where the alloy is melted, measured around 2 mm, and the distance between the hole and the wheel was 1-2 mm. The alloys were ejected with an overpressure of argon of 200 mbar when the melting temperature was of about 1250 ℃.

Figure 2.4. Third step of the fabrication process: the melt spinning technique.

One example of the obtained material is presented in Figure 2.5. As it can be observed the samples were obtained in the form of long ribbons with different geometry parameters (mainly width and thickness), as different alloy compositions were obtained in different laboratories. Detailed geometry parameters for all the compositions used in this PhD work are given in Table 2.1.

Figure 2.5. View of the $Fe_{54}Ni_{24}Cr_2Si_{10}B_{10}$ amorphous ribbon obtained by the melt spinning technique.

Table 2.1. Geometry parameters and density of the alloys used in this PhD work.

Sample composition	***Width (mm)***	***Thickness (μm)***	***Density (kg/m³)***
$Fe_{40}Ni_{38}Mo_4B_{18}$	6.0	30	7544
$Fe_{64}Co_{21}B_{15}$	2.6	23	7644
$Fe_{64}Co_{17}Si_{6.6}B_{12.4}$	1.6	28	7450
$Fe_{55}Ni_{25}B_{20}$	2.1	32	7668
$Fe_{54}Ni_{24}Cr_2Si_{10}B_{10}$	1.8	30	7455

The composition of the chromium containing fabricated alloy was analysed using a SEM-EDX (Hitachi TM3000) electronic microscope, that is shown in Figure 2.6 and the obtained data was analysed with the Quantax 70 software.

Energy Dispersive X-ray spectroscopy (EDX) is an analytical technique used for the elemental analysis or chemical characterization of a sample. It relies on an interaction of some source of X-ray excitation and the sample. Its characterising capabilities are due to the fundamental

principle that each element has a unique atomic structure allowing a unique set of peaks on its electromagnetic emission spectrum which is the main principle of spectroscopy.

Figure 2.6. Hitachi TM 3000 SEM-EDX apparatus.

An EDX setup consists of four primary components: an excitation source (electron beam or x-ray beam), an x-ray detector, a pulse processor and an analyser. To stimulate the emission of characteristic X-rays from a specimen, a high-energy beam of charged particles such as electrons or protons, or a beam of X-rays, is focused into the sample being studied. In our case the beam is the same used in the SEM. The incident beam may excite an electron in an inner shell, ejecting it from the shell while creating an electron hole where the electron was. An electron from an outer, higher-energy shell then fills the hole, and the difference in energy between the higher-energy shell and the lower energy shell may be released in the form of an X-ray. The number and energy of the X-rays emitted from a specimen can be measured by an energy dispersive spectrometer. As the energies of the X-rays are characteristic of the difference in energy between the two shells and of the atomic structure of the emitting element, EDX allows to measure the elemental composition of the specimen. The excitation and emission processes that allows the composition characterization in EDX analysis are very briefly shown in Figure 2.7.

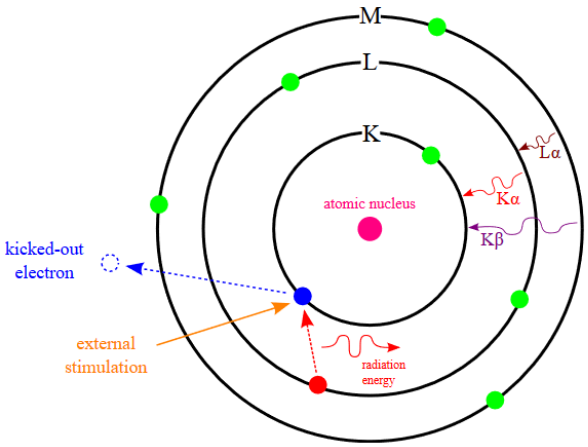

Figure 2.7. Basic principle of X-ray emission process due to an external excitation on a material.

Therefore, the EDX analysis allows us to know the composition of the fabricated alloy in order to ensure that the chromium has been incorporated to the amorphous glass alloy and that no significant quantity of chromium has been lost. In Table 2.2 the obtained results for this fabricated composition after the melt-spinning process can be observed. The resolution of the used SEM-EDX is not sensitive enough to be able to properly distinguish boron from carbon. Due to this, the obtained weight percentages were 'not normalised', assuming that the amount that rests to reach the 100% corresponds to the non-measured boron percentage.

Table 2.2. SEM-EDX obtained results for the $Fe_{54}Ni_{24}Cr_2Si_{10}B_{10}$ composition.

Metals	***Expected mass (% wt)***	***EDX results (% wt)***
Fe	61.32	60.39
Ni	28.65	26.92
Cr	2.11	2.09
Si	5.71	5.52
B	2.19	-

As it can be observed in the obtained EDX values (Table 2.2), the chromium content of the prepared strips is similar to the expected one. This indicates that during the fabrication process there are no significant chromium losses. Even more, the obtained percentages for all the elements of this alloy are in good agreement with the expected values obtained from the initial composition calculations.

2.1.2. Magnetic and magnetoelastic characterization

2.1.2.1. Hysteresis loop

Hysteresis loops of the ribbons were measured by using a Vibrating Sample Magnetometer (VSM) model EZ7 from Microsense, LLC that is shown in Figure 2.8.

Figure 2.8. Vibrating Sample Magnetometer located at BCMaterials used to obtain the hysteresis loops.

The VSM was developed by S. Foner in 1959[2] after the development of the Vibrating-Coil Magnetometer by D.O. Smith in 1956[3]. A simplify scheme of the basic operating principle of the VSM is presented in Figure 2.9. The sample is placed within a uniform magnetic field *H* generated by an electromagnet that induces a magnetic moment *m* in the sample, while a perpendicular oscillation is applied to the sample, normally by means of a piezoelectric or a linear actuator. The resulting oscillating magnetic field of the vibrating sample induces a voltage in the sensing pickup coils proportional to the magnetic moment of the sample, and from measurements of this voltage the magnetic properties of the sample can be deduced. The resulting signal is amplified and recorded by standard techniques.

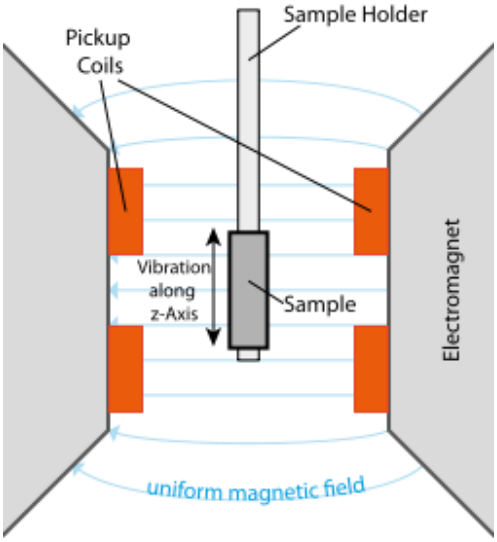

Figure 2.9. VSM operating principle.

The obtained magnetic polarization $\mu_0 M$ (in Tesla) versus magnetic field (in A/m) graph corresponding to the commercial Metglas 2826MB3 is shown in Figure 2.10 (saturation magnetization value given by the seller company: 0.88 T). Obtained results for all the samples used in this PhD work are summarised in Table 2.3.

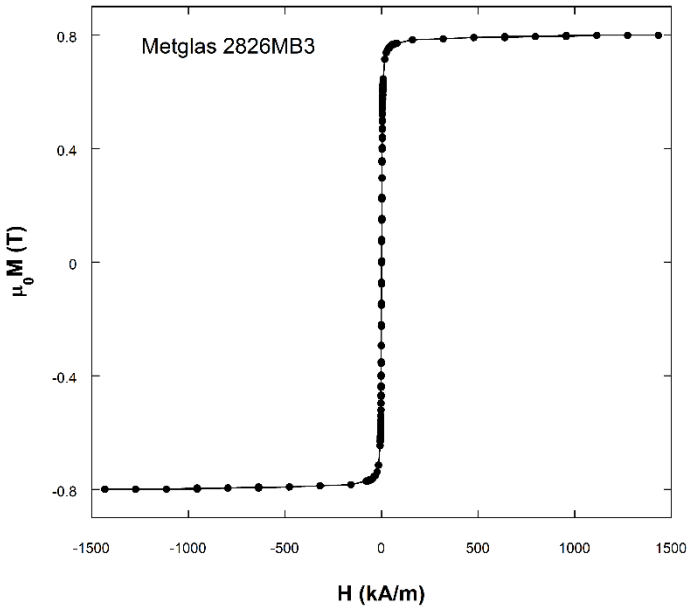

Figure 2.10. Room temperature measured hysteresis loop of Metglas 2826MB3 obtained with the VSM technique.

2.1.2.2. Magnetostriction

The magnetostriction of the samples was measured using strain gauges connected to an electronic Wheatstone bridge working in half bridge configuration and including a passive gauge for passive compensation. The employed device was a Portable Strain Indicator Model P-3500 (Instruments division), the strain gauges were purchased from Kiowa Electronics Instruments Co., Ltd., and attached to the ribbons using a M-Bond 600 adhesive purchased from Micro-Measurements. The employed strain gauges were chosen as small as possible to correctly stick to the ribbons which can be seen in Figure 2.11. They were squared shaped of 0.2 mm side, with a gauge factor of 1.99 and a resistance of 120 Ω.

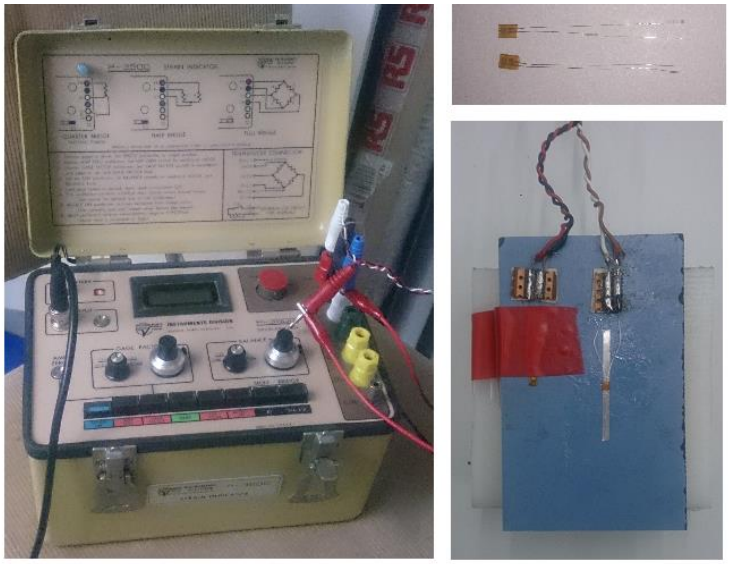

Figure 2.11. Pictures of the P-3500 Strain indicator apparatus (left) and the employed gauges (right-up) and the half bridge configuration to measure the ribbons (right-down).

The elongation detection mechanism is based on the changes of the ohmic resistance of the stain gauge conductor due to the elongation, or piezoresistive effect. This strain is calculated from the following expression:

$$\varepsilon = \frac{\Delta L}{L} = \frac{\Delta R/R}{GF} \qquad [2.1]$$

being $\Delta R/R$ the ratio of fractional change in electrical resistance and GF the gauge factor of the strain gauge.

The applied magnetic field was generated with the coil system shown down below in Figure 2.12. The magnetic field was generated by a pair of Helmholtz coils and driven by a bipolar power supply (KEPCO BOP 20-20M). The sample in half bridge configuration, as shown in Figure 2.11, was placed in the central region within the coils set-up and the change of the electrical resistivity suffered by the strain gauge was measured at the strain indicator, and recorded in the computer.

Figure 2.12. General view of the Helmholtz coils and measurement system.

Figure 2.13 shows the obtained magnetostriction measurement for the Metglas 2826MB3 (value given by the seller company: 12 ppm). The magnetostriction values obtained for all the employed samples are summarised in Table 2.3.

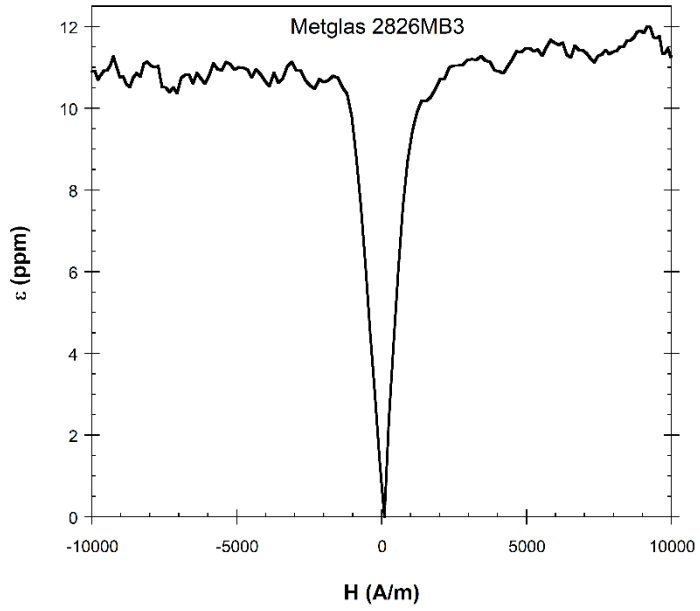

Figure 2.13. Magnetostriction curve for Metglas 2826MB3 sample.

2.1.2.3. Magnetoelastic resonance and ΔE effect

The magnetoelastic resonance (MR) characterization curves and the derived *ΔE effect* were measured using an experimental set-up consisting of three coaxial solenoids. The external solenoid generates a static magnetic field (bias) of 11 kA/m (138.2 Oe/A). The so-called primary coil was located within this solenoid and applied an AC magnetic field of 2.94 kA/m per ampere (36.9 Oe/A). A secondary coil was placed within the primary one and picked up the induced signal, which was then visualised in a HP 3589A spectrum analyser and recorded in a computer. The whole experimental set-up is presented in Figure 2.14.

The spectrum analyser does not only allow to observe the magnetoelastic resonance curve in a wide range of frequencies between 10 Hz and 150 MHz, but also provides the AC voltage to excite magnetically (via the primary coil) the ferromagnetic ribbons. The DC magnetic field was applied by using a HP 6653A power supply. The MR frequency was determined by applying an excitation field of constant amplitude and by switching its frequency from 30 kHz to 400 kHz, while keeping the DC magnetic field amplitude constant.

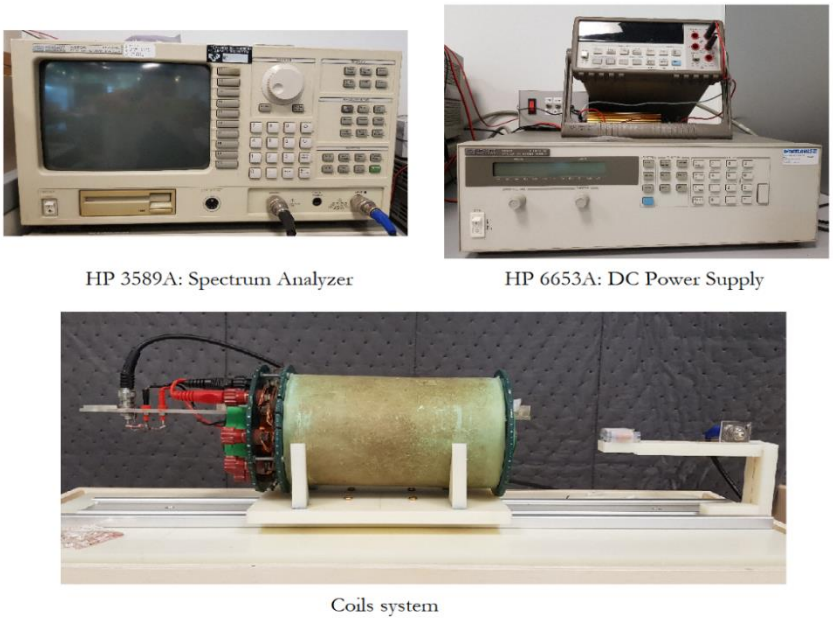

Figure 2.14. General view of the set-up employed to measure the magnetoelastic resonance.

Figure 2.15 shows the resonance frequency curves obtained for different length ribbons of composition $Fe_{64}Co_{17}Si_{6.6}B_{12.4}$. This sample shows good magnetoelastic properties. Each curve was measured at the applied DC field where the resonance frequency amplitude was maximum. These resonance frequencies evidently increased as diminishing the length of the magnetoelastic strips, as it can be concluded from Equation 1.3.

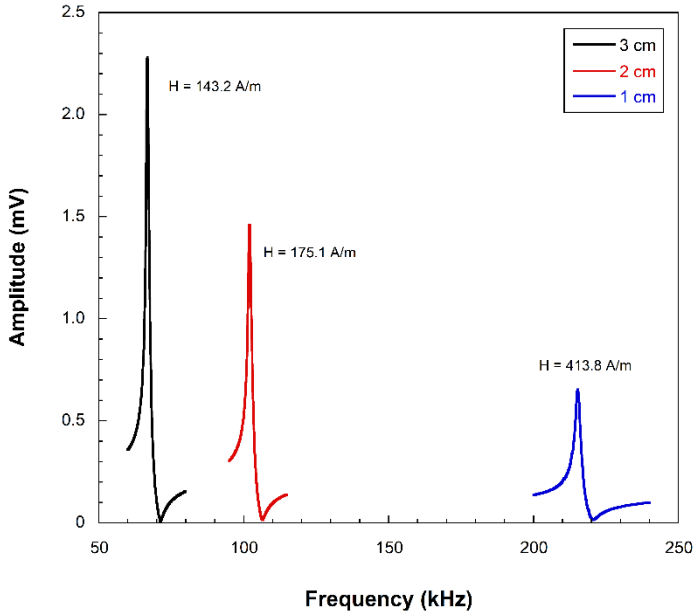

Figure 2.15. Obtained magnetoelastic resonance curves for different lengths of the $Fe_{64}Co_{17}Si_{6.6}B_{12.4}$ sample.

From those magnetoelastic resonance curves of the ribbons, the main magnetoelastic parameters can be obtained. Using Equations 1.4, 1.5 and 1.6, the Young modulus E, the magnetoelastic coupling coefficient k and the quality factor Q can be obtained. As resonance frequency changes with the applied magnetic field, the magnetoelastic parameters also will change as a function of the applied magnetic field. Typical dependences of the Young modulus $E(H)$, the magnetoelastic coupling coefficient $k(H)$ and the quality factor $Q(H)$ with the applied magnetic field are shown in Figure 2.16.

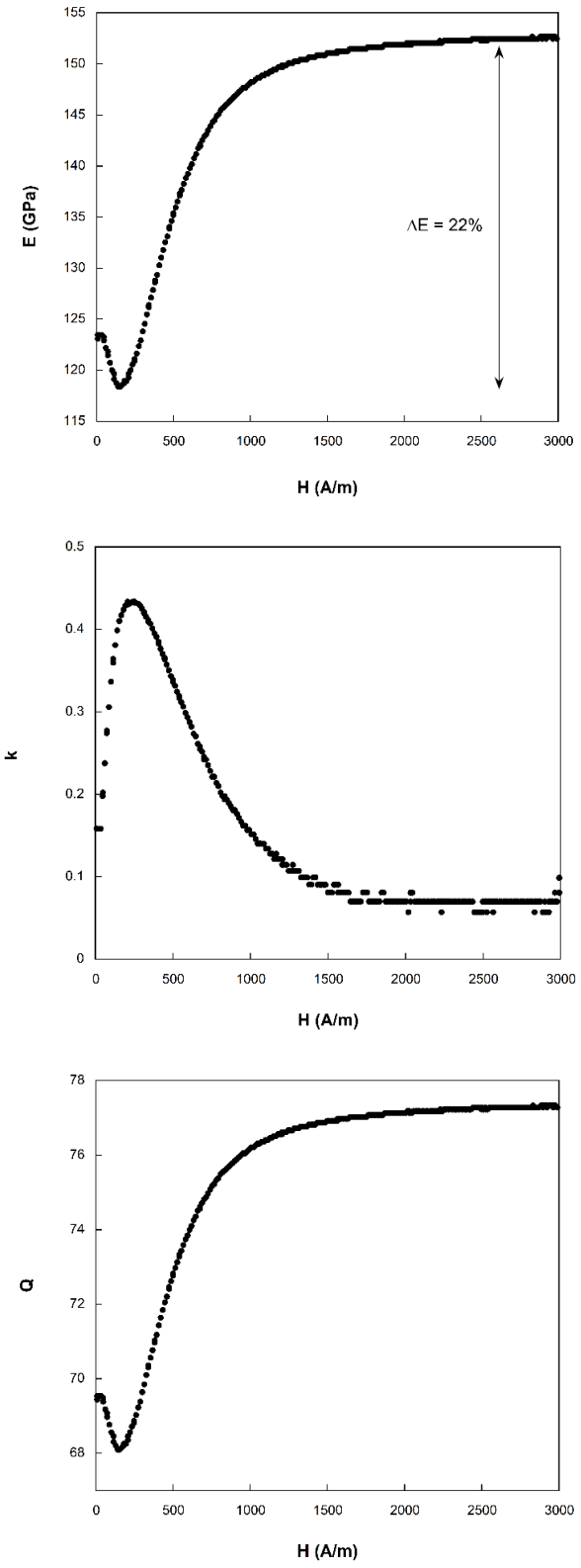

Figure 2.16. *ΔE effect* or $E(H)$ dependence (upper), magnetoelastic coupling coefficient k (middle) and quality factor Q (lower) as a function of the applied magnetic field for a $3\ cm$ long ribbon of composition $Fe_{64}Co_{17}Si_{6.6}B_{12.4}$.

The obtained values for all the magnetic and magnetoelastic characterization for all the studied samples are presented in Table 2.3. The presented ΔE effect values and the magnetostriction ones were obtained for 3 cm length ribbons.

Table 2.3. Saturation magnetization and magnetostriction, and ΔE *effect* values obtained for each alloy used in this PhD work.

Sample composition	$\mu_0 M_S\ (T)$	$\lambda_S\ (ppm)$	$\Delta E\ effect\ (\%)$
$Fe_{40}Ni_{38}Mo_4B_{18}$	0.88	11	2.5
$Fe_{64}Co_{21}B_{15}$	1.03	20	11
$Fe_{64}Co_{17}Si_{6.6}B_{12.4}$	1.65	20.5	22
$Fe_{55}Ni_{25}B_{20}$	1.41	16	0.9
$Fe_{54}Ni_{24}Cr_2Si_{10}B_{10}$	1.22	11.5	6.8

The magnetic and magnetoelastic properties are affected by the composition of the amorphous metallic alloys. As expected, the addition of Cr decreases the saturation magnetization and magnetostriction. Nevertheless, a good ΔE *effect* has been measured for those samples showing a little dependence of the Young modulus with the applied magnetic field.

On the other hand and concerning magnetoelastic measurements performed at the University of Patras (Greece) the used system is shown in Figure 2.17. This magnetoelastic sensing instrumentation box, designed for measuring and characterizing magnetoelastic sensors, measures the impedance of a solenoid coil that is used for sensor interrogation. During the sensor interrogation, a constant AC current is applied to the coil, which generates an almost uniform AC magnetic field (inside the coil). When a magnetoelastic strip is put inside the coil, with its length parallel to the coil axis, it responds to the AC magnetic field and longitudinally vibrates as a result of the magnetostriction. The

longitudinal vibration of the sensor generates in turn a changing magnetic flux due to the magnetoelastic effect, resulting in an impedance change of the coil. The resonance behaviour of the sensor is characterized by analysing the impedance spectrum.

So, in this case, to take the measurements, a microcontroller-controlled frequency generator drove a current amplifier connected to a single coil. This coil does not only generate the alternating magnetic field, but also detects the magnetic flux generated by the magnetoelastic material. A scheme of the remote query nature of the magnetoelastic sensors and a picture of the magnetoelastic sensor "reader box" used are shown in Figure 2.17. The "reader box" was connected via a RS 232 port to a computer for data display and storage[4]. When the frequency of the vibration matches with the natural frequency of the sensor, resonance occurs, and the maximum measured at that point is easily followed by the automated set-up[5]. A graphical user interface designed using Microsoft® Visual Basic® allowed the user to digitally specify all measurement parameters, such as the frequency sweep range, the frequency steps, the dc biasing field and the ac excitation voltage.

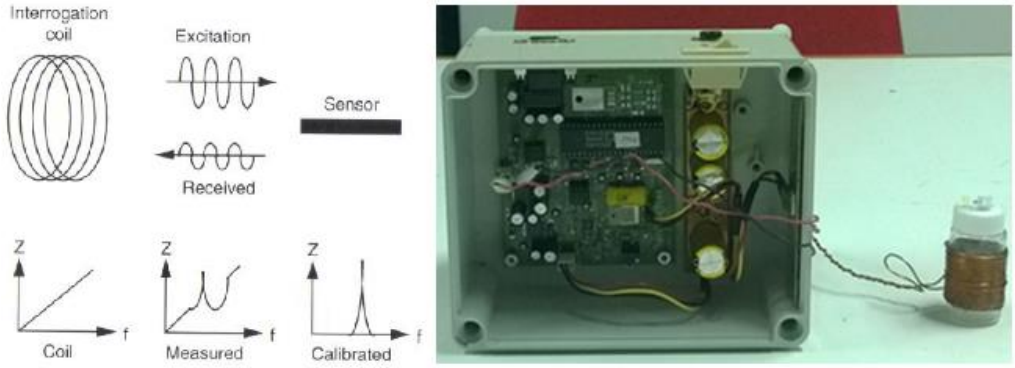

Figure 2.17. Homemade coil and magnetoelastic resonance measurement box.

This set-up system was used for the measurements presented in Chapter 4, related to the zinc oxide depositions, Young modulus calculations and hydrogen peroxide sensing experiments, and in Chapter 5 for the o-xylene detection using three different zeolite types.

2.1.3. Corrosion behaviour of selected compositions

Magnetoelastic resonators are generally surface functionalized ribbon-shaped strips with different recognition layers that provides diverse target detection possibilities: aqueous chemical detection such as pH[6], glucose concentration[7], as well as inorganic salts deposition[5]. Also gas analytes as humidity[8], carbon dioxide[9], or volatile organic compounds[10] as benzene or xylene among others can be detected. Even more, they have been successfully used as biosensors for different pathogens as Salmonella[11] or Escherichia Coli[12]. Independently of the target to be sensed, in many cases such detection processes must be performed in aqueous solution or aggressive media, when arising corrosion produces subsequent degradation of the material affecting the magnetic properties and sensing capability.

Iron rich glasses show outstanding magnetic and magnetoelastic properties that increase the sensitivity to those detection processes due to their excellent magneto-mechanical properties and high magnetoelastic coupling effect. Nevertheless, they also show tendency to corrosion as the corrosion resistance usually is not high. Metallic glasses show better corrosion resistance if compared with crystalline samples that can be attributed to the homogeneous single glass phase, the alloy chemistry and the presence of metalloids. Even more, the absence of grain boundaries, dislocations, and other defects where corrosion can preferentially occur allow the growth of a uniform protective layer. The homogeneity in both the chemical composition and microstructure promotes amorphous oxide formation on the surface which retards ionic transport, and therefore corrosion. Corrosion can be affected by several parameters as: the amorphous structure, chemical and structural homogeneity, chemical composition, among others. Figure 2.18 shows a clear example of the composition influence: in order to functionalize the substrates, two equal length strips of commercial Metglas 2826MB3 ($Fe_{40}Ni_{38}Mo_4B_{18}$, high corrosion resistance), and a homemade metallic glass of composition $Fe_{64}Co_{17}Si_{6.6}B_{12.4}$ were immersed in a water solution. After 4 hours, the corrosion effect is clearly visible for the homemade Fe-rich ribbon case.

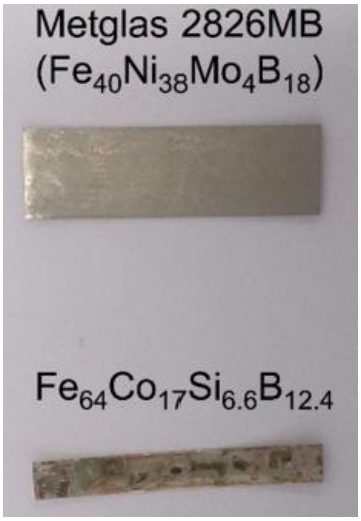

Figure 2.18. Corrosion effect in commercial Metglas 2826MB3 and a homemade metallic glass of composition $Fe_{64}Co_{17}Si_{6.6}B_{12.4}$.

Since the first Fe-based metallic glass was synthesised by liquid quenching in 1967[13], rapidly quenched alloys became a new class of engineering materials for which the knowledge of their Glass Forming Ability (GFA) and corrosion resistance behaviour turned out to be fundamental aspects[14]. In particular, corrosion behaviour of these materials has been shown to be mainly controlled by the presence or absence of a protective, passive layer. This passive layer may act as a protective barrier against aggressive environments improving the corrosion resistance of the material. The best corrosion resistance is achieved when the passive layer is stable, not only in the media where it was generated but also in other aggressive environments to which it may be exposed.

The employed ferromagnetic alloys are mainly composed of an 80% of metallic elements and a 20% of non-metallic, and the corrosion behaviour of the material is determined by the composition of the alloy. For that purpose, special compositions can be fabricated by substituting part of the commonly used metallic elements: Fe, Ni or Co, or by changing the metalloids: Si or B.

Many studies already established that the use of Ni instead of Co[xi] improve the corrosion resistance. The addition of a small amount of other

metallic elements to the alloy such as Cr [11,15,16,17] , Zr[18], Y[19], Mo[20], among others greatly improve the corrosion resistance of metallic glasses. Generally, the minor addition of elements such as Cr, Mo or Y, will provoke the formation of a passive layer, resulting in an improvement of the corrosion resistance [15,21,22] , but as the composition changes some magnetic and magnetoelastic properties degrade. This passive layer must be stable and protect the material against external environmental parameters. Nevertheless, the role of the metalloids is not completely clear, as the effect of a given metalloid depends on the rest of the components and on the solution composition of the corrosion experiment. An increase of the B content in some alloys has been used to improve the corrosion resistance of a glassy alloy[23]. With P addition the kinetics of passivation and composition of passive film were improved in acid solution, while with Si replacement of P, the corrosion resistance can be enhanced[24].

Bearing all this in mind and due to some corrosion problems that occurred when trying to deposit some materials as zeolites, the fabrication of samples with an improved corrosion resistance resulted to be needed. The well-known, commercial metallic glass with high corrosion resistance, Metglas 2826MB3 ($Fe_{40}Ni_{38}Mo_4B_{18}$), widely used for such biological and chemical detection purposes, will be used as reference for comparison of the obtained corrosion resistance values of our homemade metallic glasses.

Corrosion is an unwanted spontaneous electrochemical reaction occurring between a material, (usually a metal or metallic alloy), and its environment that can lead to structural degradation of the material. As electrochemical reaction is the sum of two half reactions: an oxidation process (electron loss) and a reduction process (electron gain). In corrosion, the oxidation reaction is always the destructive oxidation of the metal which losses electrons, while the reduction is usually caused by water reduction or dissolved oxygen reduction. Corrosion represents a huge problem in daily life and it has been the cause of many catastrophic damages, as for example the sinking of the Erika ship, which broke in two spilling 30 kilotons of heavy fuel oil to the sea. In fact in 2013 the

United States estimate the direct cost of corrosion to be about 1 trillion dollars per year.

In order to measure the corrosion resistance, electronic chemistry methods such as potentiodynamic polarization are applied in most researches, where considerable information on the electrode processes can be attained, such as corrosion potential (E_{corr}), corrosion current density (I_{corr}), corrosion rate, pitting behaviour, passivity, and the cathodic behaviour. A schematic curve of the theoretical anodic polarization and the calculation of corrosion potential and corrosion current density can be observed in Figure 2.19.

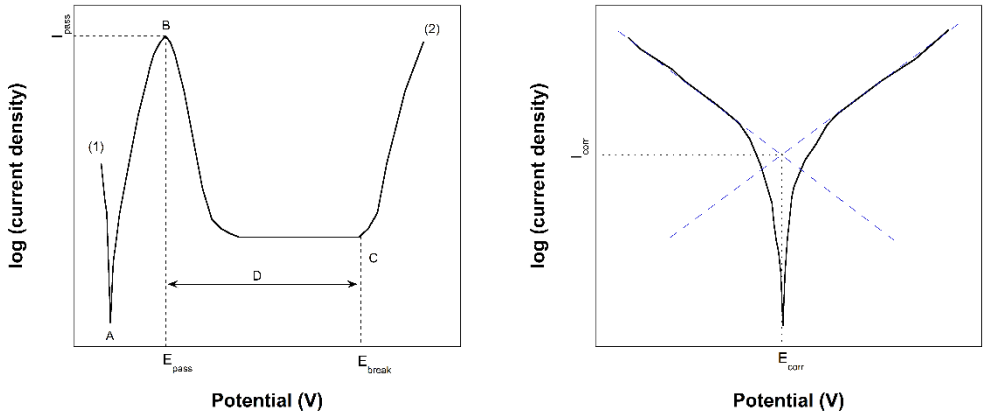

Figure 2.19. Schematic diagram of potentiodynamic polarization: theoretical curve (right) and calculation of corrosion potential and corrosion current density (left).

The potentiodynamic experimental curve shown in Figure 2.19 (right) starts at point (1) and progresses in the positive potential direction until reaching point (2), that is at anodic polarization. The open circuit potential (OCP) is located at point A: at this potential the sum of the anodic and cathodic reaction rated on the electrode surface is zero. As a result, the measured current will be closed to zero. With the increase of the potential, it moves towards the active region. In this region, metal oxidation is the dominant reaction until point B is reached, which corresponds to the passivation potential. As the applied potential increases above that value, the current density decreases until a low, passive current density is achieved in passive region D. Once the

potential reached a sufficiently positive value, point C, sometimes called the breakaway potential, the applied current rapidly increases.

Around the open circuit potential, corrosion parameters can be obtained by fitting two lines according to the linear regions of the polarization curves as it can be observed in Figure 2.19 (left). The current density at that obtained point will be the corrosion current density (I_{corr}) and the potential at which it falls is the corrosion potential (E_{corr}), that can also be calculated by using the Tafel fit of the polarization resistance (R_p) of the material. R_p is defined as the inverse of the slope of the current density against the potential curve at the free corrosion potential. It is generally agreed that the higher the corrosion potential, the more difficult is the occurrence of the oxidation reaction for the metals; moreover, the larger the corrosion current density is, the higher the corrosion rate will be, that is, the lower corrosion resistance for metallic glasses[25].

In our case, Linear Polarization Resistance (LPR) technique was used to monitor the corrosion processes in the samples. This technique is specially designed for the determination of the E_{corr}, i_{corr} and R_p of a material through potential steps around the corrosion potential. All the anodic polarization curves of the amorphous metallic alloys were performed with a BioLogic VMP3 Potensciostat/Galvanostat in the three electrode conventional cell that can be observed in Figure 2.20. As working electrode (WE) the amorphous metallic strip was used, as reference electrode (RE) an Ag/AgCl ingold electrode purchased from Methrom and as counter electrode (CE) a platinum foil electrode purchased from Methrom. As electrolyte solution, a saline phosphate buffer solution (PBS) (0.138 M NaCl and 0.0027 M KCl) purchased from Sigma. The measurements were made at room temperature (25 ℃) and at pH 7.3 with a scan rate of 0.5 mV/s. Before measuring the corrosion resistance behaviour, the samples were cleaned with acetone in sonication for 5 minutes and dried at room temperature in order to avoid any contamination form the fabrication or manipulation processes.

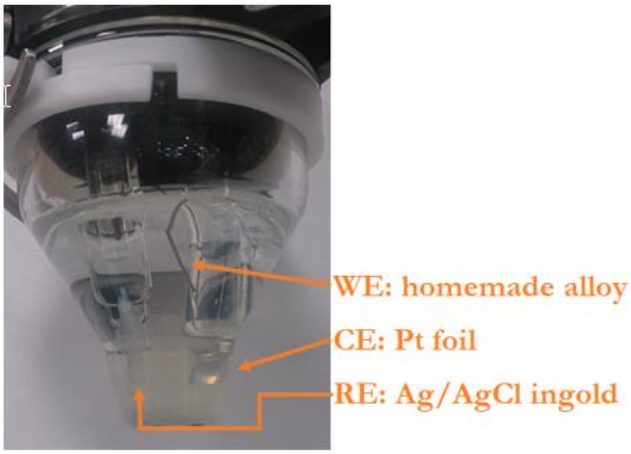

Figure 2.20. Cell used for the corrosion experiments with the three electrodes on it.

To perform the measurements the sample were left to stabilise for $30\ minutes$, measuring the open circuit potential (OCP), and afterwards the working electrode was forced to decrease -250 mV from the OCP and scan the potential in the anodic direction at 0.5 mV/s until 250 mV above that OCP. By analysing the obtained curves with the software EC-Lab (in particular Tafel fit and R_p fit) values for the corrosion potential (E_{corr}), the corrosion current density (i_{corr}) and the corrosion resistance (R_p) were obtained. The obtained curves are presented in Figure 2.21.

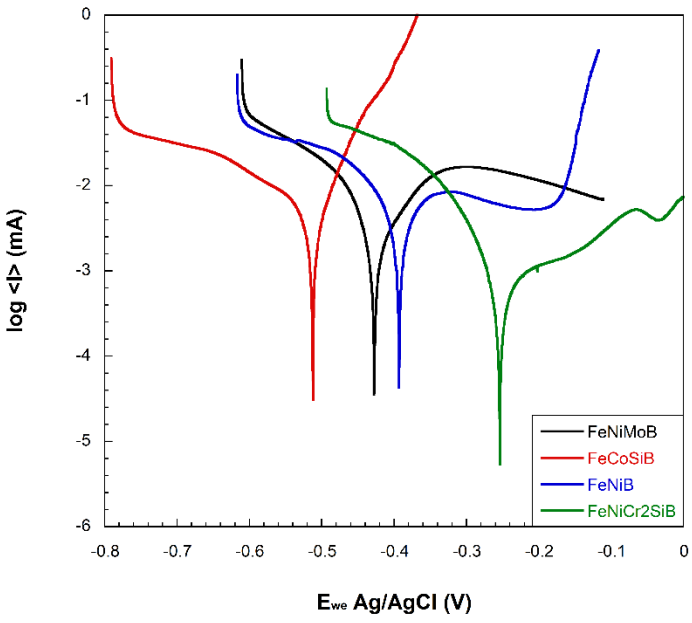

Figure 2.21. LPR curves measured for all the studied samples.

As expected Co containing alloy has shown the worst corrosion resistance, with the lowest values of corrosion potential. Substitution of Co by Ni improves the corrosion resistance as it has been experimentally demonstrated. However, the alloy with the best corrosion behaviour is the one containing Cr, as the addition of certain amount of Cr greatly improves the corrosion resistance behaviour of these amorphous alloys. The values for corrosion potential corrosion current density and polarization resistance obtained by fitting the LPR curves are summarised in Table 2.4.

Table 2.4. Corrosion potential, corrosion current and polarization resistance values obtained for all the studied samples.

Sample composition	$\boldsymbol{E_{corr}}$ $(\boldsymbol{V})$	$\boldsymbol{J_{corr}\ 10^{-6}}$ $(\boldsymbol{A/cm^2})$	$\boldsymbol{R_p\ 10^3}$ $(\boldsymbol{\Omega\ cm^2})$
$Fe_{40}Ni_{38}Mo_4B_{18}$	−0.42	8.15	6.47
$Fe_{64}Co_{17}Si_{6.6}B_{12.4}$	−0.51	8.18	11.74
$Fe_{55}Ni_{25}B_{20}$	−0.39	13.07	7.41
$Fe_{54}Ni_{24}Cr_2Si_{10}B_{10}$	−0.25	2.54	53.22

Other kinds of processes that can occur during corrosion can be studied, such as pitting or passivation by performing cyclic-potentiodynamic polarization (CPP) experiments. A schematic cyclic polarization curve is shown in Figure 2.22. A potential scan is started below the corrosion potential, E_{corr} where the current density goes to zero, and then increases to a low and approximately constant anodic value in the passive range. In this range, the passive film, a thin oxide/hydroxide film, protects the material from high corrosion rates. If the current density decreases when the potential scan direction is reversed, as in path 1, the material is shown to be immune to pit corrosion. However, if on the potential up scan, the current density suddenly increases, then remains high on the down scan, until it finally decreases to the passive-region value, as in path 2, where the material is shown to undergo a form of pitting corrosion. The potential at which

the current density suddenly increases (pitting initiation) is known as the pit potential, E_{pit}, and the potential at which the current density returns to the passive value is known as the repassivation potential or the protection potential, E_{pp}. Between E_{pit} and E_{pp}, pits are initiating and propagating. In the case of path 2, pits will not initiate at E_{corr}, the natural corrosion potential; and, therefore, the material will not undergo pitting corrosion under natural corrosion conditions. If, on the other hand, path 3 is exhibited, where $E_{pp}$is below E_{corr}, the material will undergo pitting corrosion at surface defects.

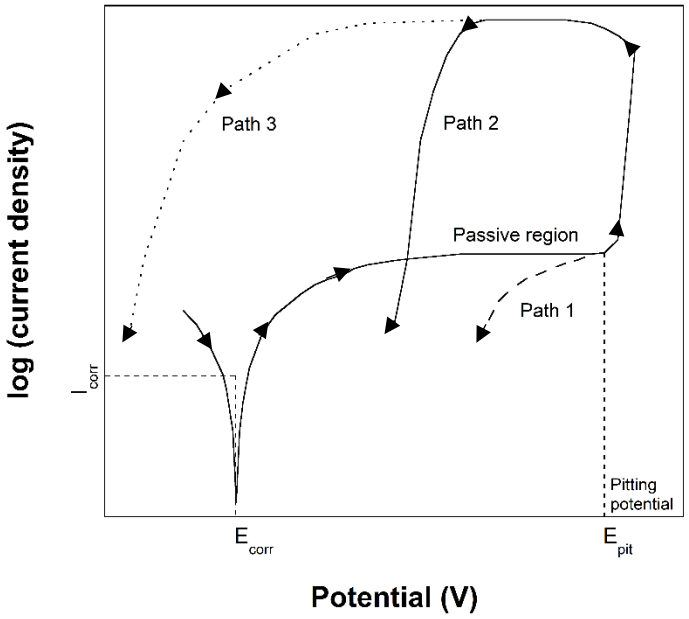

Figure 2.22. Schematic diagram of cyclic potentiodynamic polarization curve.

CPP measurements are used for general corrosion studies. In this type of corrosion, anodic dissolution is uniformly distributed over the entire metallic surface. The corrosion rate is nearly constant at all locations.

The corrosion behaviour of three fabricated samples were studied by electrochemical methods, and the obtained values were compared with the commercial high corrosion resistance Metglas 2826MB3 ($Fe_{40}Ni_{38}Mo_4B_{18}$). The homemade samples were $Fe_{64}Co_{17}Si_{6.6}B_{12.4}$, $Fe_{55}Ni_{25}B_{20}$ and $Fe_{54}Ni_{24}Cr_2Si_{10}B_{10}$. The obtained values for corrosion

potential, current density, and polarization resistance, are given and discussed in terms of Ni and Cr content.

As it can be observed in Figure 2.23, the Fe-Co sample does not present any passive region where passivation processes take place, as it happens with the other samples. In the Fe-Co sample the obtained curve is wholly caused by the oxidation process of the alloy. In Fe-Ni containing samples, there is a passive region which extension depends on the other elements of the composition. As it was expected the Cr containing alloy is the one with the larger passivation plateau, since that chromium tends to form a stable passive layer. Even more, in all the samples the protection potential is higher than the corrosion potential which means that pitting processes will undergo at surface flaws, as it has been previously explained in Figure 2.22.

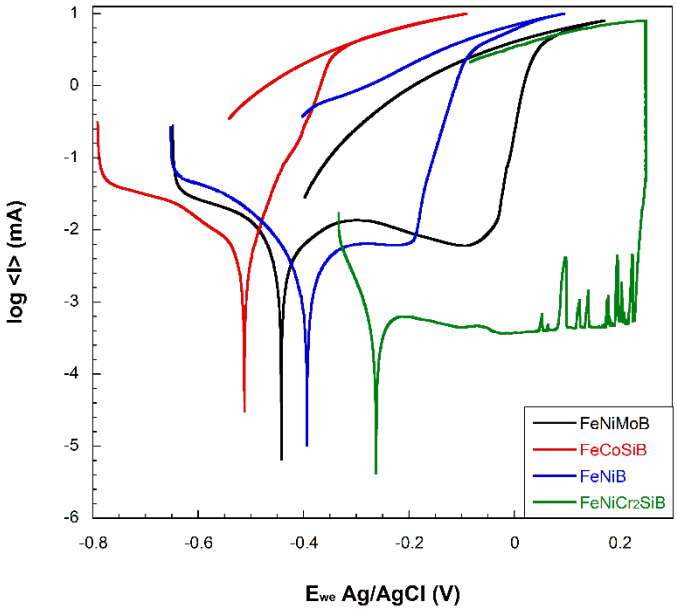

Figure 2.23. Cyclic Potentiodynamic Polarization for all the studied samples.

The polarization resistance experiments, made to study the corrosion behaviour of the different magnetoelastic amorphous alloys $Fe_{40}Ni_{38}Mo_4B_{18}$ (commercial Metglas 2826MB3), $Fe_{64}Co_{17}Si_{6.6}B_{12.4}$, $Fe_{55}Ni_{25}B_{20}$, $Fe_{54}Ni_{24}Cr_2Si_{10}B_{10}$, have demonstrated that the alloy with the best behaviour against corrosion is $Fe_{54}Ni_{24}Cr_2Si_{10}B_{10}$in a PBS media

at 25 ℃ and a pH of 7.3. This sample has the highest corrosion potential, with the lower corrosion current density and a high polarization resistance. Besides, it also has a good *ΔE effect*, not as good as the other homemade alloys but the addition of chromium, which improves the corrosion resistance behaviour decreases the magnetoelastic properties of the material. Nevertheless, it is still better than the commercial alloy making this alloy also interesting for sensing applications. The obtained results let us assume that we have improved the corrosion resistance of our homemade magnetoelastic material, not affecting too much the magnetostrictive properties which still make these alloys suitable for developing sensor with chemical or biological detection purposes.

As a visual proof of our observations, Figure 2.24 shows pictures taken at different times for the studied alloys, in which the development of the corrosion process can be observed.

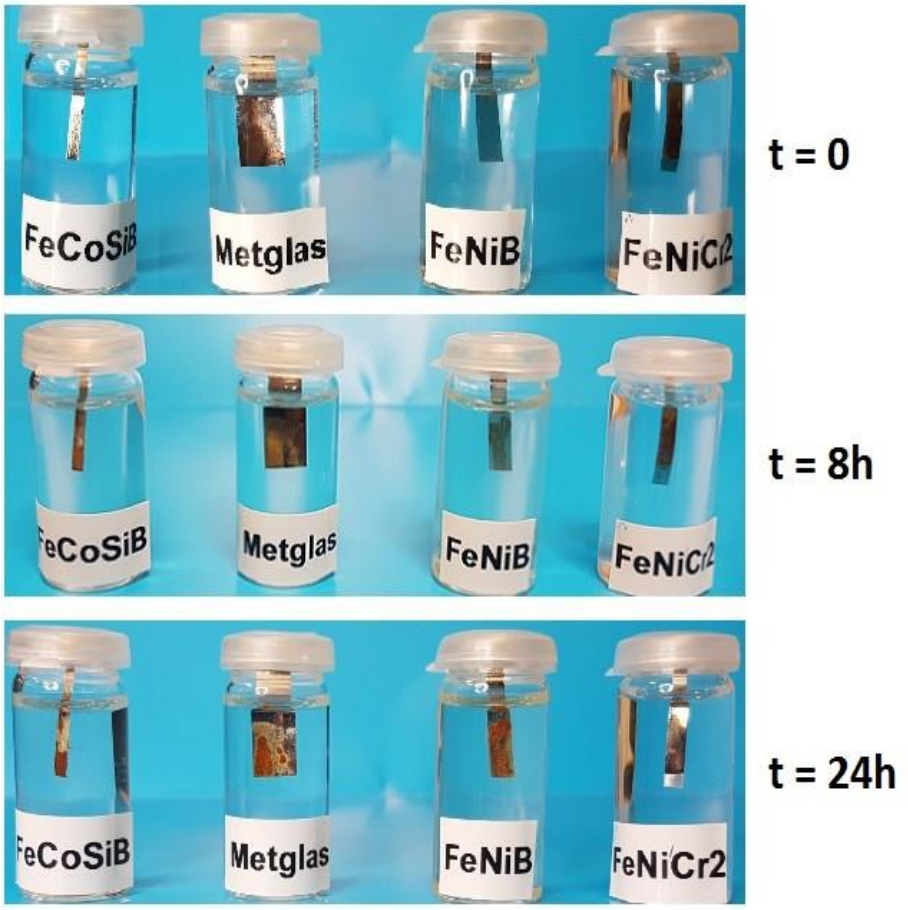

Figure 2.24. Pictures taken at different times (initial time, after 8 hours and after 24 hours) for all the studied samples to visually observe the corrosion process.

2.2. Characterization of the active layers onto the magnetoelastic resonant platforms

2.2.1. X-Ray Diffraction (XRD)

XRD is a powerful non-destructive analytical technique for characterizing crystalline solids and powders. It provides information on crystal structures, phases, preferred crystal orientations, chemical composition and physical properties of the materials. A primary use of this technique is the identification and characterization of compounds based on their diffraction pattern. XRD is based on constructive interferences of monochromatic X-rays and the sample. Those X-rays are generated by a cathode ray tube, filtered to produce monochromatic radiation, collimated to concentrate, and directed toward the sample. In materials with regular structure, the interaction of the incident rays with the sample produces constructive interference (and a diffracted ray) when conditions satisfy Bragg's law:

$$n\,\lambda = 2\,d\,sin\theta \qquad [2.3]$$

where n is an integer, λ is the wavelength of the X-rays, d is the interplanar spacing generating the diffraction, and θ is he diffraction angle. This law relates the wavelength of electromagnetic radiation to the diffraction angle and the lattice spacing in a crystalline structure. A schematic representation of the diffraction principle can be observed in Figure 2.25.

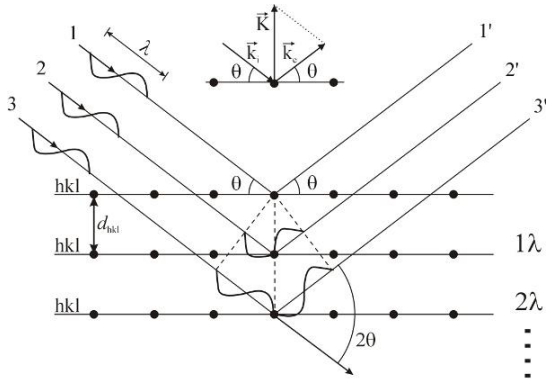

Figure 2.25. X-Ray Diffraction principle.

The directions of the possible diffractions depend on the size and shape of the unit cell of the material. The intensities of the diffracted waves depend on the kind and arrangement of the atoms in the crystalline structure. In this work, the XRD difractograms were useful to identify the nature of the formed precipitate/films. By scanning the sample through a range of 2θ angles, all possible diffraction direction of the lattice should be attained. The conversion of the diffraction peaks to d-spacings allows the identification of the compound, as each compound has a set of unique d-spacings[26]. Typically, this is achieved by comparison of d-spacings with standard reference patterns, as it will be shown later.

X-ray diffractometers consist of three basic elements: an X-ray tube, a sample holder and a X-ray detector. X-rays are generated in a cathode ray tube by heating a filament to produce electrons, accelerating the electrons toward a target by applying a voltage, and bombarding the target material with the electrons. Those electrons have enough energy to dislodge inner shell electrons of the target material and characteristic X-ray spectra are produced. Copper is the most common target material for single-crystal diffraction. These X-rays are collimated and directed onto the sample. As the sample and the detector are rotated, the intensity of the reflected X-rays is recorded. When the geometry of the incident X-rays impinging the sample satisfies the Bragg equation, a constructive interference occurs as well as a peak in intensity. The geometry of a diffractometer is such that the sample rotates in the path of the collimated X-ray beam at an angle θ while the detector is mounted on an arm to collect the diffracted X-rays and rotates at an angle of 2θ.

XRD measurements were made with a Bruker D8 advanced diffractometer, shown in Figure 2.26, operated at 40 kV and 40 mA using CuKα radiation with a scanning speed of 0.35 sec/step for 2θ in a range from 15 to 70 for zinc oxide measurements and in a range of 5 to 40 for zeolite measurements.

Figure 2.26. Bruker D8 diffractometer at FORTH institute.

2.2.2. Scanning Electron Microscopy (SEM)

The scanning electron microscope produces images of a sample by scanning the surface of the sample with a focused beam of electrons. It is a powerful magnification technique that can provide topological, morphological and compositional information. Even more, it is useful to detect and analyse surface fractures, to provide information about microstructures, to examine surface contamination or to reveal spatial variations in chemical compositions or to provide qualitative chemical analyses among others. Therefore, SEM technique has found a variety of applications in a number of scientific and industry related fields.

In a SEM imaging run, the electrons interact with the atoms at various depths within the sample producing various signals that contain information about the sample surface topography and composition. Due to the very narrow electron beam, SEM micrographs have a large depth of field yielding a characteristic three-dimensional appearance useful for understanding the surface structure of the sample.

In a typical SEM instrument, the electron beam is thermo-ionically emitted from an electron gun fitted with a tungsten filament cathode. Tungsten is usually employed in thermos-ionic electron guns because it has the highest melting point at lowest vapor pressure of all metals, thereby allowing it to be electrically heated for electron emission, and because of its low cost. This generated electron beam is accelerated down and passed through a combination of lenses and apertures to produce a focused beam of electrons which hits the surface of the sample. The beam passes through pairs of scanning coils which are responsible for controlling the position of the electron beam on the sample or pair of deflector plates in the electron column, typically above the objective lens, which deflect the beam so that it scans over a rectangular area of the sample surface. This scanning beam enables information about a defined area of the sample to be collected. As a result of the electron-sample interaction, a number of signals are produced and detected by appropriate detectors. The sample is mounted on a stage in the chamber area, and both, the column and the chamber are evacuated by a combination of pumps. The level of vacuum required will depend on the design of the microscope. A simple scheme of a SEM instrument structure can be observed in Figure 2.27.

The morphology and structure of the fabricated particles formed and the homogeneity of the deposited layers appearing in this PhD report were studied by using SEM microscopy with a Zeiss SUPRA 35VP instrument operated at 10 kV, that can be seen in Figure 2.28.

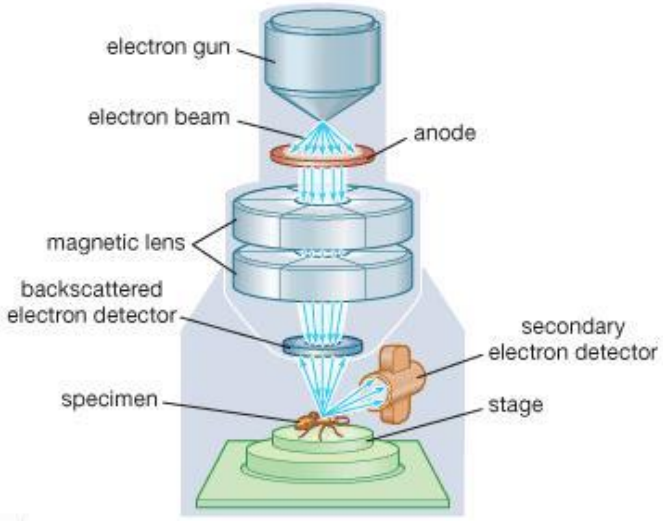

Figure 2.27. Simplified scheme of a scanning electron microscope.

Figure 2.28. Zeiss Supra 35VP Scanning Electron Microscope.

2.2.3. Photoluminescence emission (PL)

Photoluminescence emission phenomena involve the energy absorption and subsequent light emission, the later generically known as luminescence. That is when a laser type light illuminates a material, both Raman scattering and photoluminescence can occur. PL comprises both fluorescence and phosphorescence processes and originates from an absorption/emission process between different electronic energy levels

in the material. One example of luminescent materials are phosphors that emit light when excited by radiation and which are usually fabricated as microcrystalline powders or thin films designed to provide visible colour emission.

Photoluminescence, fluorescence and phosphorescence occur when a material is excited by absorbing photons and then emits them with a decay time that is characteristic of the sample environment. Photoluminescence is the term that physicists use to describe the absorption and emission of light by a certain kind of material such as semiconductors. Fluorescence is a term used by chemists when the absorbing and emitting species are atoms or molecules. Usually fluorescence is "fast" (ns time scale). Phosphorescence is similar to fluorescence, except that it is "slow", this means that the time between absorption and emission is longer than in fluorescence (up to hours or even days). Figure 2.29 describes those different phenomena.

Dispersing the photoluminescence light to form a spectrum is a good optical method to probe the electron transitions between high and low energy states, allowing investigation of the impurities, defects, and bandgaps in semiconductor materials. This method does not only show the energy states, but also the electron densities of states for electron transitions, which supply more electronic information[27].

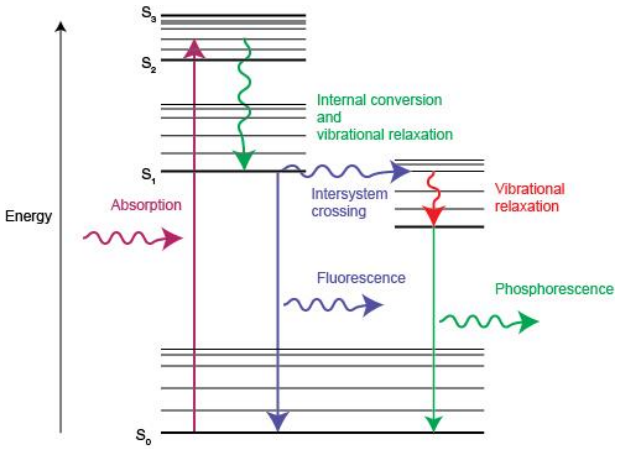

Figure 2.29. Luminescence phenomena.

As proof of the quality of the ZnO layers deposited onto the magnetoelastic strips, PL spectra were also recorded at room temperature with a Hitachi F2500 Fluorescence Spectrophotometer, working from 350 to 600 nm at an excitation wavelength of 325 nm, instrument that can be seen in Figure 2.30.

Figure 2.30. Hitachi F2500 Fluorescence Spectrophotometer.

2.2.4. Atomic Force Microscopy (AFM)

Atomic force microscopy (AFM) is a very high resolution type of scanning probe microscopy (SPM). The information is gathered by "feeling" or "touching" the surface of the studied material with a mechanical probe. The AFM was invented by IBM scientist Gerd K. Bennig in 1982[28]. The AFM precursor, the scanning tunnelling microscope (STM) was developed by Gerd Binnig and Heinrich Rohrer in the early 1980s at IBS Research-Zurich, a development that earned them the 1986 Nobel Prize for Physics.

Figure 2.31 shows the typical configuration and working principle of an AFM: an atomic force microscope consists of a cantilever (1) with a sharp tip (probe) (4), that are carried by a support (2). The cantilever is typically silicon or silicon nitride with a tip radius of curvature of the order of the nanometres. Optionally, a piezoelectric element (3) oscillates the cantilever. The sharp tip is fixed to the free end of the cantilever. When

the tip is brought into proximity of the sample surface, forces between the tip and the sample lead to a deflection (displacement with respect to the equilibrium position) of the cantilever according to Hooke's law. The detector (5) measures the deflection of the cantilever and converts it into an electrical signal. The intensity of this signal will be proportional to the displacement of the cantilever. The detector used to be a position-sensitive photodetector where the deflections of the light of the laser are collected. The sample (6) is mounted on the sample stage (8) and it is displaced in the three directions x, y, and z with respect to the tip due to a 'xyz drive' (7). Although Figure 2.31 shows the drive attached to the sample, the drive can also be attached to the tip, or independent drives can be attached to both, since it is the relative displacement of the sample and tip that needs to be controlled[29].

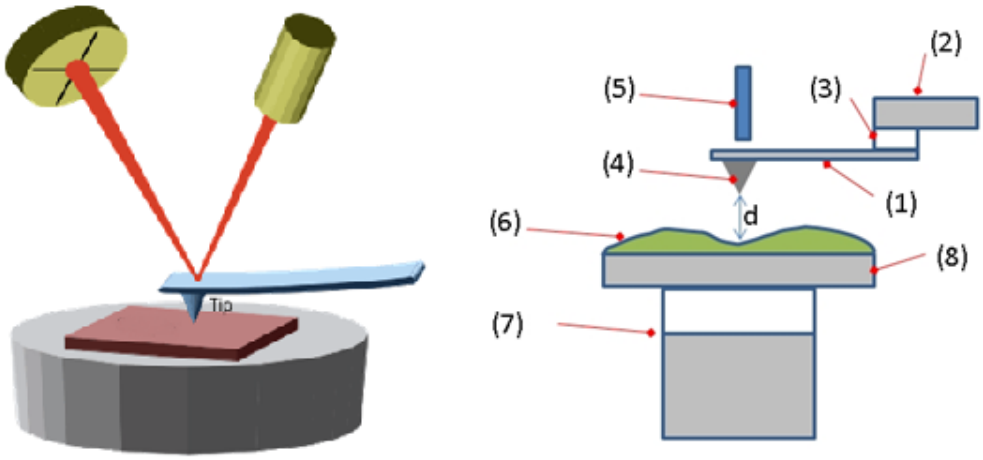

Figure 2.31. Configuration and working principle of the Atomic Force Microscope.

According to the configuration described above, the interaction between tip and sample, which can be an atomic scale phenomenon, is transduced into changes of the motion of cantilever which is a macro scale phenomenon. Several different aspects of the cantilever motion can be used to quantify the interaction between the tip and sample, most commonly the value of the deflection, the amplitude of an imposed oscillation of the cantilever, or the shift in resonance frequency of the cantilever. In fact, the AFM can be operated in a number of modes, depending n the application. In general, possible imaging modes are

divided into static or contact modes and a variety of dynamic or tapping (non-contact) modes where the cantilever is vibrated or oscillated at a given frequency.

The AFM has three major abilities: force measurement, imaging, and manipulation. In force measurement, AFMs can be used to measure the forces between the probe and the sample as a function of their mutual separation. This can be applied to perform force spectroscopy, to measure the mechanical properties of the sample, such as the sample's Young's modulus, a measure of stiffness. For imaging, the reaction of the probe to the forces that the sample imposes on it can be used to form an image of the three-dimensional shape (topography) of a sample surface at a high resolution. This is achieved by a raster scanning the sample position with respect to the tip and recording the height of the probe that corresponds to a constant probe-sample interaction. In manipulation, the forces between tip and sample can also be used to change the properties of the sample in a controlled way. Examples of this include atomic manipulation, scanning probe lithography and local stimulation of cells.

The AFM has been applied to problems in a wide range of disciplines of the natural sciences, including solid-state physics[30] (identification of atoms at a surface, evaluation of interactions of atoms), semiconductor science and technology[31], molecular engineering, polymer chemistry and physics[32], surface chemistry[33], molecular biology (study of the protein complexes), cell biology (distinguish cancer and normal cells[34]), and medicine.

Concerning the work presented in this PhD report, AFM images will be taken to observe the topography of the deposited polystyrene layers when using two different solvents: tetrahydrofuran and toluene, respectively.

References

[1] https://metglas.com/magnetic-materials/ (07/2017).

[2] S. Foner, "Versatile and sensitive Vibrating-Sample Magnetometer", The Review of Scientific Instruments 30 (1959) 548-557. DOI: 10.1063/1.1715538.

[3] D.O. Smith, "Development of a Vibrating-Coil Magnetometer", The Review of Scientific Instruments 27 (1956) 261-268. DOI: 10.1063/1.1716679.

[4] X. Gao, R. Zhen, Y. Zhang and C.A. Grimes, "Detecting penicillin in mil with a wireless magnetoelastic biosensor", Sensor Letters 7 (2009) 6-10. DOI: 10.1166/sl.2009.1002.

[5] N. Bouropoulos, D. Kouzoudis, C.A. Grimes, "The real-time, in situ monitoring of calcium oxalate and brushite precipitation using magnetoelastic sensors", Sensors and Actuators B: Chemical 109 (2005) 227–232. DOI: 10.1016/j.snb.2004.12.054.

[6] C.A. Grimes, W.R. Seitz, J. Horn, S.A. Doherty and M.T. Rooney, "A remotely interrogatable magnetochemical pH sensor", IEEE Transactions on Magnetics 33 (1997) (5) 3412-3414. DOI: 10.1109/20.617961.

[7] C.A. Grimes, C.S. Mungle, K. Zeng, M.K. Jain, W.R. Dreschel, M. Paulose and G.K. Ong, "Wireless magnetoelastic resonance sensors: A critical review", Sensors 2 (2002) (7) 294-313. DOI: 10.3390/s20700294.

[8] C.A. Grimes, D. Kouzoudis, E.C. Dickey, D. Kiang, M.A. Anderson, R. Shahidain, M. Lindsey and L. Green, "Mangetoelastic sensors in combination with annometer-scale honeycombed thin film ceramic TiO2 for remote query measurement of humidity", Journal of Applied Physics 87 (2000) (9) 5341-5343. DOI: 10.1063/1.373341.

[9] Q.Y. Cai, A. Cammers-Goodwin and C.A. Grimes, "A Wireless, remote query magnetoelastic CO2 sensor", Journal of Environmental Monitoring 6 (2000) 556-560. DOI: 10.1039/B004929H.

[10] T. Baimpos, L. Gora, V. Nikolakis and D. Kouzoudis, "Selective detection of hazardous VOCs using zeolite/Metglas composite sensors", Sensors and Actuators A: Physical 186 (2012) 21-31. DOI: 10.1016/j.sna.2011.12.030.

[11] R. S. Lakshmanan, R. Guntupalli, J. Hu, D. J. Kim, V. A. Petrenko, J. M. Barbaree, and A. B. Chin, "Phage immobilized magnetoelastic sensor for the detection of Salmonella typhimurium," Journal of Microbiological Methods 71(2007) (1) 55–60. DOI: 10.1016/j.mimet.2007.07.012.

[12] C. Ruan, K. Zeng, O. K. Varghese, and C. A. Grimes, "Magnetoelastic immunosensors: Amplified mass immunosorbent assay for detection of Escherichia coli O157:H7," Analytical Chemistry 75 (2003) (23) 6494–6498. DOI: 10.1021/ac034562n.

[13] P. Duwez and S. C. H. Lin, "Amorphous ferromagnetic phase in iron-carbon-phosphorus alloys," Journal of Applied Physics 38 (1967) 4096. DOI: 10.1063/1.1709084.

[14] Y.Waseda and K. T. Aust, "Corrosion behaviour of metallic glasses," Journal of Material Science 16 (1981) 2337–2359. DOI: 10.1007/BF01113569.

[15] E.F. Marzo, A.R. Pierna, J. Barranco, G. Vara, A. Lorenzo, A. Pérez and J.A. García, "Corrosion behaviour of Fe/Co based amorphous metallic alloys in saline solutions: new materials for GMI based biosensors", Portugaliae Electrochimica Acta 25 (2007) 131-137. DOI: 10.4152/pea.200701131.

[16] R. B. Diegle, D. M. Lineman, and M. T. Thomas, "Repassivation kinetics of glassy alloys", Electrochemical Society Extended Abstract 82 (1982) 143.

[17] M. F. López, M. L. Escudero, E. Vida, and A. R. Pierna, "Corrosion behaviour of amorphous Fe-Cr-Ni-(Si, P) alloys", Electrochimica Acta 42, 659–665 (1997). DOI: 10.1016/S0013-4686(96)00211-3.

[18] M. Xu and Q. Wang, "Thermal stability and magnetic properties of Fe-Co-M-Zr-Nb-Ge-B (M = Mo, Cr) bulk metallic glasses", Progress in Natural Science: Materials International 24 (2014) 116–120. DOI: 10.1016/j.pnsc.2014.03.004.

[19] Z.M. Wang, Y.T. Ma, J. Zhang, W.L. Hou, X.C Chang and J.Q. Wang, "Influence of yttrium as a minority alloying element on the corrosion behaviour in Fe-based bulk metallic glasses", Electrochimica Acta 54 (2008) 261-269. DOI: 10.1016/j.electacta.2008.08.017.

[20] S. J. Pang, T. Zhang, K. Asami, and A. Inoue, "Bulk glassy Fe-Cr-Mo-C-B alloys with high corrosion resistance", Corrosion Science 44 (2002) 1847–1856. DOI: 10.1016/S0010-938X(02)00002-1.

[21] A. Pardo, M.C. Merino, E. Otero, M.D. López and A. M'hich, "Influence of Cr additions on corrosion resistance of Fe- and Co-based metallic glasses and nanocrystals in H2SO4", Journal of non-crystalline solids 352 (2006) 3179-3190. DOI: 10.1016/j.noncrysol.2006.05.021.

[22] C.S. Kiminammi, C.A.C. Souza, L.F. Bonavina, L.R.P. de Andrade Lima, S. Sariñach, M.D. Baró, C. Bolfrini and W.J. Botta, "Partial crystallization and corrosion resistance of amorphous Fe-Cr-M-B (M = Mo, Nd) alloys", Journal of non-crystalline solids 356 (2010) 2651-2657. DOI: 10.1016/j.jnoncrysol.2010.04.051.

[23] S.J. Pang, T. Zhanf, K. Asami and A. Inoue, "Bulk glassy Fe-Cr-Mo-C-B alloys with high corrosion resistance", Corrosion Science 44 (2002) 1847.1856. DOI: 10.10/S0010-938X(02)00002-1.

[24] M.F. López, M.L. Escudero, E. Vida and A.R. Pierna, "Corrosion behaviour of amorphous FeCrNi(Si, P) alloys", Electrochimica Acta 42, (1997) 659-665. DOI: 10.1016/S0013-4686(96)00211-3.

[25] Behrooz Movahedi, "Metallic glasses – Formation and Properties [Chapter 4: Corrosion resistance and electrocatalytic properties of metallic glasses]", (S. Wang), Inthech (2016). ISBN: 978-953-51-2511-2. DOI: 10.5772/63677.

[26] A.A. Bunaciu, E.G. Udristioiu and H.Y. Aboul-Enein, "X-ray diffraction: instrumentation and applications", Critical Reviews in Analytical Chemistry 2015, 45, 289-299. DOI: 10.1080/10408347.2014.949616.

[27] J.H. Lin, R.A. Patil, R.S. Devan, Z.A. Liu, Y.P. Wang, C.H. Ho , Y. Liou and Y.R. Ma, "Photoluminescence mechanism of metallic Zn nanospheres, semiconducting ZnO nanoballoons, and metal-semiconductor Zn/ZnO nanospheres", Scientific reports 4, (2014) Article number 6967. DOI: 10.1038/srep06967.

[28] Gerd K. Bennig, "Atomic force microscope and method for imaging the surfaces with atomic resolution", Patent US4724318.

[29] G. Haugstd, "Atomic Force Microscopy: Understanding basic and advanced applications" [Chapter 1; Overview of AFM 1-32], Willey Online Library (2012). ISBN: 9780470638828.

[30] Y. Sugimoto, P. Pou, M. Abe, P. Jelinek, R. Pérez, S. Morita and O. Custance, "Chemical identification of individual Surface atoms by atomic force microscopy", Nature 446 (2007) 64-67. DOI: 10.1038/nature05530.

[31] R. Magno and B.R. Bennett, "Nanostructure patterns written in III-V semiconductors by an atomic force microscope", Applied Physics Letters 70 (1997) 1855. DOI: 10.1063/1.118712.

[32] K. Polak-Krasna, C. Fuhrhop, S. Rochat, A.D. Burrows, A. Georhiadis, C. R. Bowen and T.J. Mays, "AFM imaging and nanoindentation of polymer of intrinsic microporosity PIM-1", International Journal of Hydrogen Energy 42 (2017) (37) 23915-23919. DOI: 10.1016/j.ijhydene.2017.04.081.

[33] H. Huang, I. Doryden, P.A. Thoren, L. Ejenstam, J. Pan, M.L. Fielden, D.B. HAviland and P.M. Claesson, "Local surface mechanical properties of PDMS-silica nanocomposite probed with Intemodulation AFM", Composites Science and Technology 150 (2017) 111-119. DOI: 10.1016/j.compscitech.2017.07.013.

[34] N.V. Guz, M.E. Dokukin, C.D. Woodworth, A. Cardin and I. Sokolov "Towards early detection of cervical cancer: Fractal dimension of AFM images of human cervical epithelial cells at different stages of progression to cancer" Nanomedicine: Nanotechnology, Biology and Medicine 11 (2015) 1667-1675. DOI: 10.1016/j.nano.2015.04.012.

3. Study of the functionalization process of the magnetoelastic resonant platforms with polymers

This chapter is focused on the performed studies with the magnetoelastic resonant platforms concerning the two main factors affecting their sensing ability. The magnetoelastic ribbons were coated with a polymer, polystyrene (PS), in order to study how the mass deposition affects the resonance frequency and to determine the best conditions of the resonant platform for the future sensing applications. The important parameters ruling the magnetoelastic sensing ability are the sensitivity S and the resonance quality factor Q. The sample resonance frequency was measured at different applied magnetic fields, in order to compare the sensitivity and the quality factor under different applied magnetic field conditions, in order to achieve the best resonant frequency signal. Additionally, resonators with different ribbon lengths were compared in order to determine the one with the highest sensitivity to this mass deposition.

3.1. Introduction

As it has been previously explained, magnetoelastic materials can be use for sensing applications if they are coated with an active layer. This layer will be part of smart functionalized system that must selectively detect and trap the target molecule or analyte desired to be detected. As a consequence of the target molecule trapping, the concentration can be detected through a change in the resonant frequency of the hybrid system[1, 2, 3].

For these first studies, polystyrene will be deposited on our homemade magnetoelastic ribbons in other to observe how it gets attached to the amorphous metallic glass and in order to analyse the best resonant conditions by studying the parameters affecting the magnetoelastic resonance detection method.

3.2. Parameters affecting the chemical and biological detection processes

As previously explained, magnetoelastic materials need an active layer which is the responsible for selectively detecting and trapping the target molecules or analytes that want to be detected and/or quantified. That active layer will be deposited covering the surface of the magnetoelastic ribbon changing therefore the mass and resonant frequency of the whole sensor. This will be the starting point for the detection measurements. In order to test how the mass deposition affects the material magnetoelastic response, experiments covering magnetoelastic material with polymers have been performed and will be presented throughout this chapter.

When a magnetoelastic resonant platform is used for sensing purposes the main parameters governing the detection process are two; the quality factor, Q, and the sensitivity, S.

❖ Quality factor Q

The Q factor is the mechanical quality factor that quantifies the energy losses of a resonator, giving information about how good the resonance curve is concerning the efficiency of the energy conversion. Consequently, whereas high Q values turn into a sharper and narrower resonance curve and indicate a low rate of energy losses, small Q values give rise to a wider bandwidth and a higher rate of energy losses. Q factor is usually estimated by the following relationship:

$$Q = \frac{f_r}{\Delta f} \qquad [3.1]$$

where f_r is the resonance frequency at which amplitude is maximum A_{max} and Δf is the bandwidth measured at $A_{max} / \sqrt{2}$. In Figure 3.1 an example of the quality factor for two different resonance curves is shown.

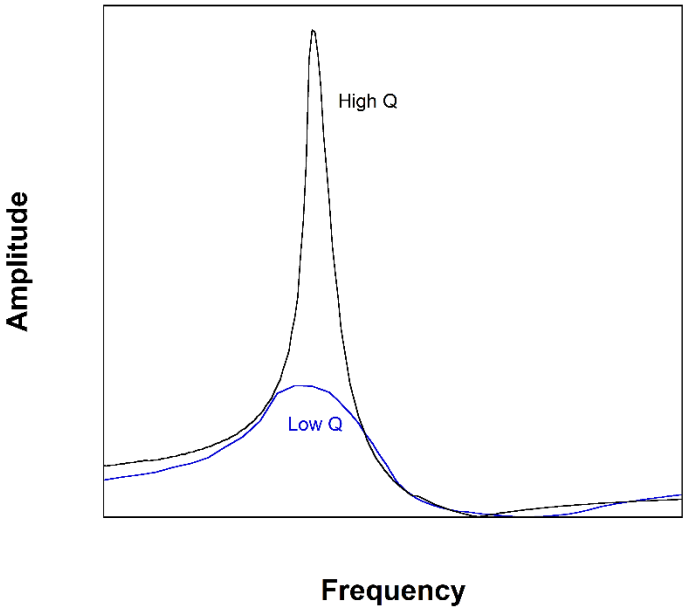

Figure 3.1. Two resonance curves with different Q value.

The quality factor is a dimensionless parameter that can be calculated and / or approximated by different methods. The mathematical expression for the Q parameter for a resonant system is given in Equation [3.1]. Kaczkowski demonstrated that by using this equation the error in Q determination could be as high as a 20% So, he modified this classical expression in order to be able to determine the Q factor of a magnetostrictive/magnetoelastic material working at its magnetoelastic resonance from impedance measurements[4]. He stablished an equation for the Q determination from the motional impedance circle diagram, which relates the resonance frequency and maximum and minimum frequency values of the real part of the resonance curve. Kaczkowski compared both methods and stablished a much higher accuracy by using his motional impedance circle.

We are now studying the best way to determine the quality factor Q taking into account the factors by which this parameter can be affected, so in this thesis report the calculation of the Q is going to be performed by using Equation 3.1.

While all Q values appearing in this report are calculated by using Equation 3.1 a deep study about Q determination has been actually performed[5].

❖ Sensitivity S

The other important parameter that affects the detection and sensing process is the sensitivity. Sensitivity, S is defined as the shift in the resonance frequency of the magnetoelastic resonator due to the attachment of a unit mass load on its surface. A higher S means a larger shift in the resonant frequency for the same mass load. A first estimation of S is given by[6]:

$$S = -\frac{\Delta f}{\Delta m} = \frac{-f_r \Delta m / 2m_0}{\Delta m} = -\frac{f_r}{2m_0} \qquad [3.2]$$

where Δf and Δm are the changes on the resonance frequency and the loading mass respectively and f_r and m_0 correspond to the resonance frequency of the unloaded resonant platform, respectively. In all the cases, it will be assumed that the mass is uniformly distributed on the whole surface of the magnetoelastic ribbon.

As it has been previously presented in Chapter 2, the resonant frequency of a magnetoelastic ribbon changes as a function of the applied magnetic field. This fact can be observed in Figure 3.2. For the first studies presented in this chapter different parameters affecting the sensing capability will be studied and presented. These experiments were made by using a 3 cm length ribbon of composition $Fe_{64}Co_{17}Si_{6.6}B_{12.4}$.

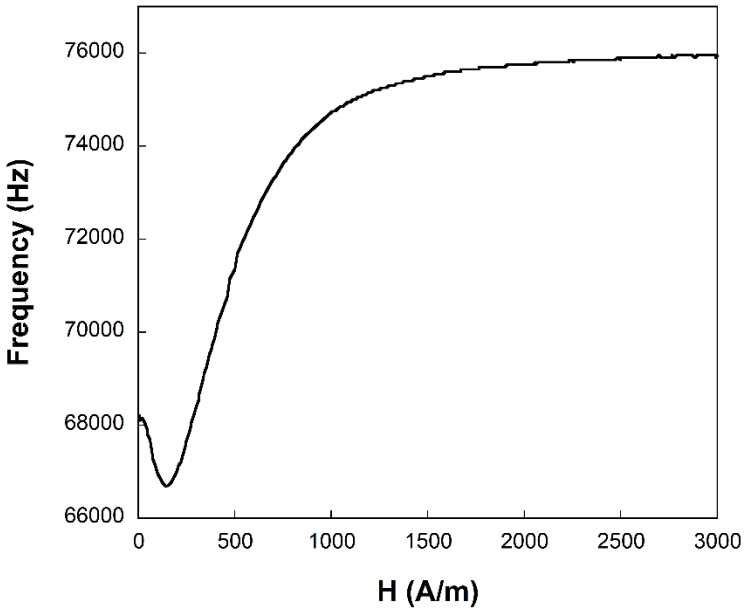

Figure 3.2. Change of the frequency of a magnetoelastic strip with the applied magnetic field.

The values of the applied magnetic field where the resonance curves were obtained and the obtained resonance frequency curves for each applied magnetic field are shown in Figure 3.3.

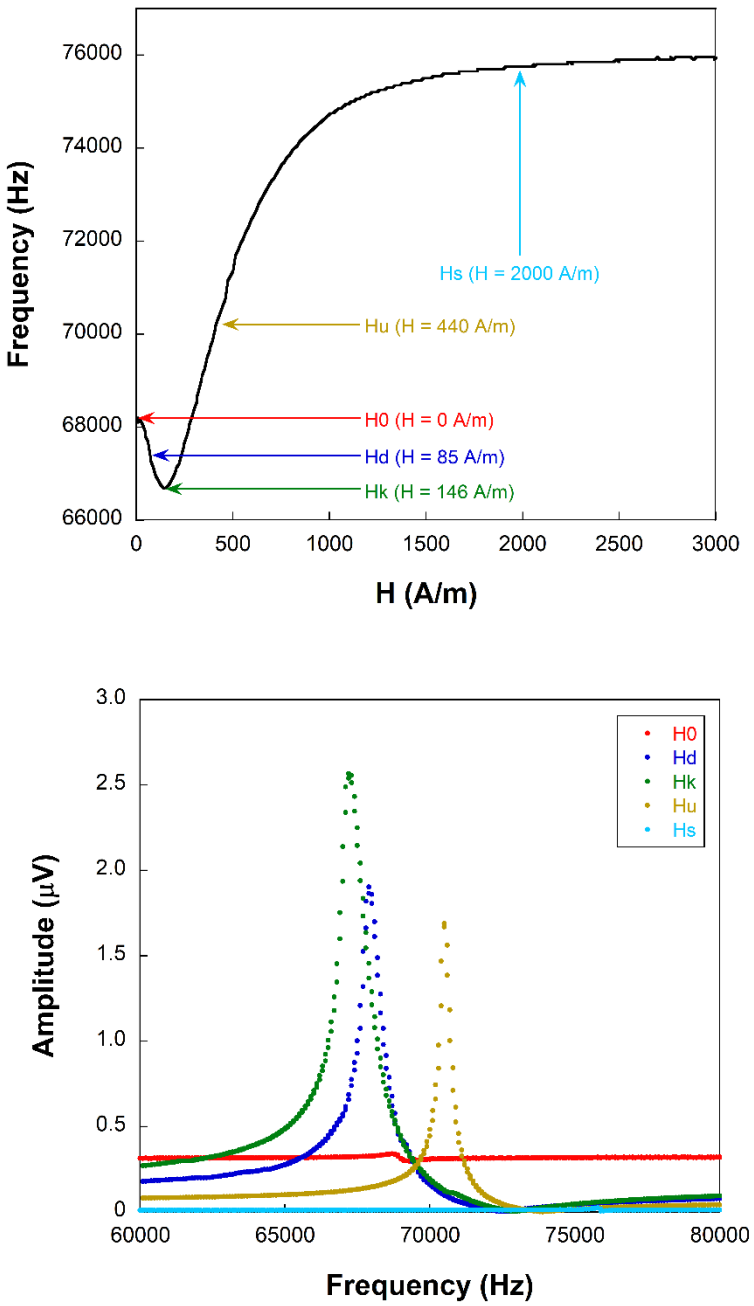

Figure 3.3. Frequency vs applied magnetic field with the selected measurement fields marked (up). Resonance frequency curves obtained at those applied magnetic field values (down).

Five different applied magnetic field values were selected for the resonance frequency measurements in order to cover the whole range of the obtained frequency versus magnetic field change. The first value where the applied magnetic field is the minimum (almost 0), H0; a

second curve was obtained during the decrease of the frequency before reaching the minimum, Hd; the third one at the called anisotropy field, Hk, where the resonance frequency is the minimum; the forth one at the increase of the frequency before reaching the magnetic saturation, Hu; and the last curve was obtained at this saturation, Hs. The quality factor of each curve was graphically calculated by using Equation [3.1] and the obtained values are presented in Table 3.1.

As it can be observed, the first and the last resonance curves obtained (H0 and Hs) have a very small amplitude, and therefore those two points were discarded for the present study.

Table 3.1. Quality factor and sensitivities calculated for the as quenched magnetoelastic ribbon at different applied magnetic fields studied.

	$H_{applied}\ (A/m)$	Q	$\lvert S\rvert\ (Hz/\mu g)$
H0	≈ 0	–	6.95
Hd	85	135	6.87
Hk	146	96	6.80
Hu	440	350	7.13
Hs	2000	190	7.67

The objective of these experiments was to determine the applied magnetic field at which the sensitivity S was the highest. Simultaneously, the resonant frequencies at different applied magnetic fields were studied during some polymer deposition experiments. All the samples were cut (at the desired length), cleaned (under sonication in methanol and acetone) and dried (with a stream of nitrogen) before making any measurement in order to remove any dirt arisen from the fabrication or handling process. To cover these samples with polystyrene, PS, a previous acid treatment was needed. Our first experiments trying to cover the as-quenched amorphous ribbons failed, as the polymer detached from the metallic surface. Therefore, in order to improve the polymer adherence to the magnetoelastic substrate, several treatments were performed, as acid or basic surface treatments.

As it was later observed by AFM topographical images, it was needed to decrease the roughness of the strips surface, in order to increase the adhesion of the polymer. To do this, an acid treatment turn out to be the best option. As the acid attacks the metallic surface, it decreases the rugosity of the surface making it smoother for the polymer deposition. The acid treatment consisted on immersing the samples in $1M\ HCl$ solution for 1 hour under sonication. The topography of the surfaces of the ribbons observed by AFM is presented in Figure 3.4, and also the obtained profiles for those samples. The ribbons roughness decreased from 140 nm in the as-quenched state to 30 nm in the acid treated ones.

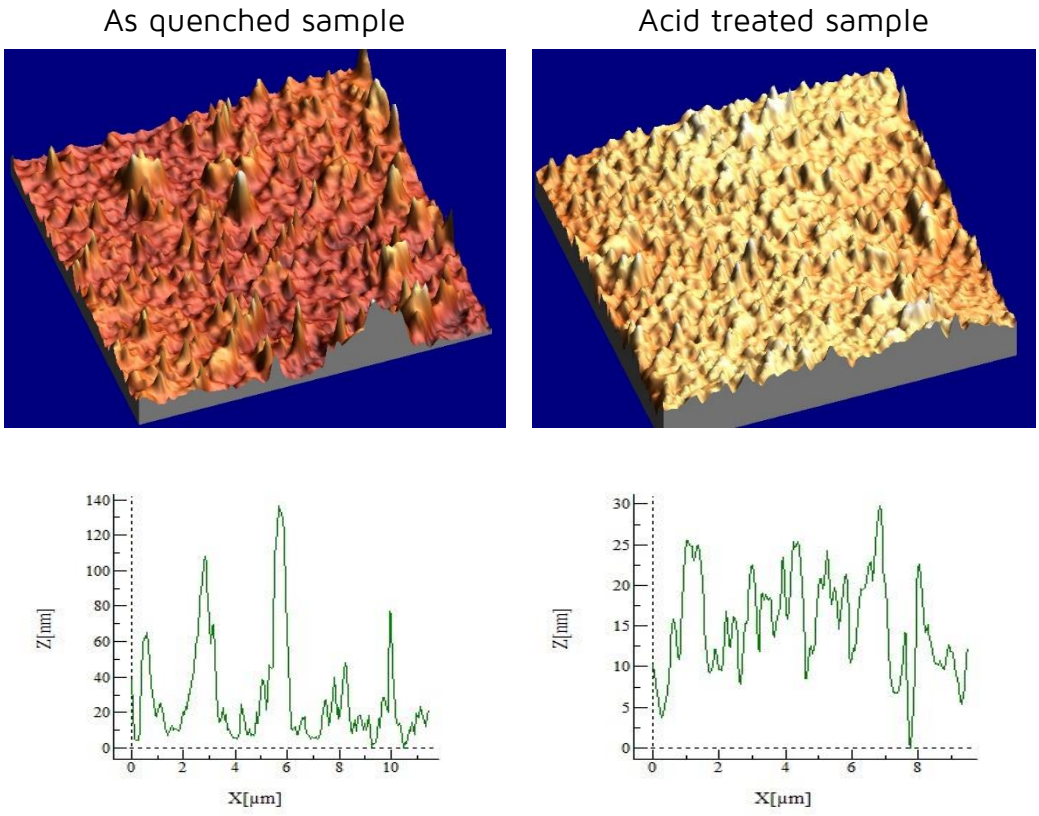

Figure 3.4. $100\ \mu m\ x\ 100\ \mu m$ AFM images for the as quenched and cleaned magnetoelastic ribbon (left) and for the acid solution treated sample (right) and their corresponding profiles.

After the cleaning process and the acid treatment, the samples were coated with polystyrene, dissolved in tetrahydrofuran (THF). These first experiments were performed by using a PS 10^{-3} M solution by using the

dip coating technique that will be later explained in detail. The samples were immersed for 30 seconds in the solution and the solvent was left to evaporate at room temperature. Several depositions were made by following the same procedure and after each deposition, not only the resonance frequency at the selected applied field values, but also the weight of the deposited polymer mass were measured.

In this way, these first experiments allowed us to study the sensitivity of the resonance frequencies obtained at different applied magnetic fields with the deposited mass. As it was expected, the resonance frequency decreased when the deposited mass of polymer increased. As it was expected and as it can be observed, the resonant frequency decreases as the mass of the materials increases Nevertheless, it is clear that this process has failed, since there is no clear correlation between the number of PS depositions (N) and the corresponding mass change. The obtained dependence of the resonance frequency with the mass for one of the applied magnetic field studied is shown in Figure 3.5.

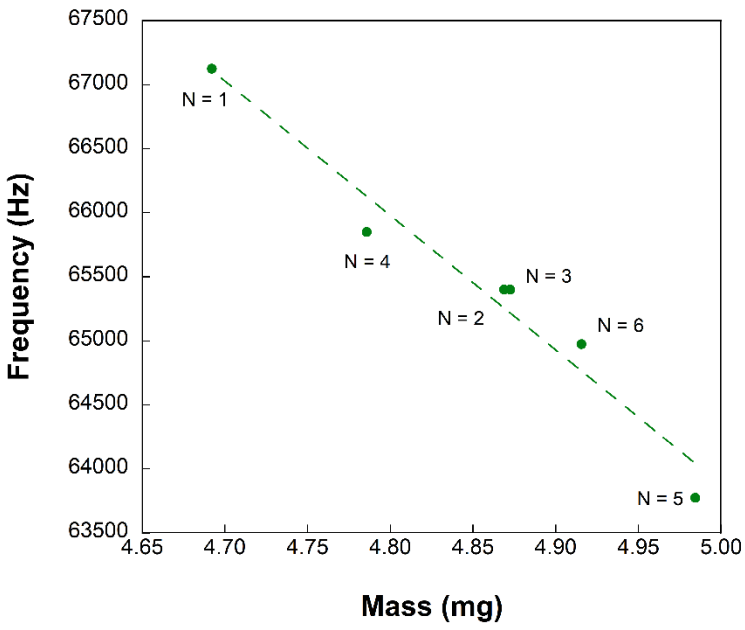

Figure 3.5. Decrease of the resonance frequency of a 3 cm length ribbon as a consequence of the mass increment during successive PS depositions.

The only clear conclusion for this initial polymer deposition study is that the highest sensitivity is obtained at Hk, although the Q is not the highest one. On the other hand, the polymer coating process has to be improved in order to achieve the increase of the deposited mass with the increasing number of depositions.

3.3. Polystyrene functionalized MRPs

In order to coat the ribbons with polystyrene, PS, the samples must be cut and cleaned. After cutting the ribbon pieces, they were cleaned to remove any dirt from the fabrication or manipulation processes. Cleaning was carried out by sonicating the samples in methanol and afterwards in acetone during 10 minutes each. Samples were dried with a stream of nitrogen. As it has been previously mentioned, in order to be able to coat the magnetoelastic resonant platforms with PS an acid treatment is needed. Samples were treated in HCl 1 M for 1 hour in sonication. The magnetic and magnetoelastic responses were not affected by the acid treatment.

The polymer active layer was deposited onto the magnetoelastic material by the dip coating technique[7]. Dip coating consists in immersing the resonant platform in an adequate polymeric solution in order to achieve the deposition of a polymeric layer. The dip coating process can be separated into five stages[8]:

1.- Immersion; the substrate is immersed in the solution of the coating material at a constant speed.

2.- Start-up; the substrate has remained inside the solution for a while and it is starting to be pulled up.

3.- Deposition; the thin layer deposits itself on the substrate while it is pulled up. The withdrawing is carried out at a constant speed to avoid any jitters. The speed determined the thickness of the coating[9].

4.- Drainage; the excess liquid will drain from the surface.

5.- Evaporation; the solvent evaporates from the liquid, forming the thin layer. For volatile solvents, such as alcohols, evaporation starts already during the deposition and drainage steps.

Many factors contribute to determine the final stage of the dip coating of a thin film. A large variety of repeatable dip coated film structures and thicknesses can be fabricated by controlling many factors as the functionality of the initial substrate surface, submersion time, withdrawal speed, number of dipping cycles. In which concerns the solution and for a successful dip coating process, also solution composition, concentration and temperature, number of solutions in each dipping sequence and environment humidity must be strictly controlled.

PS depositions onto the magnetoelastic resonant platforms can be followed by measuring the resonance frequency change associated with the corresponding PS deposition number. The PS deposition has to be done in two different ways:

1) Dipping the sample in a constant concentration solution several times. (This was done for previous experiments).

2) Dipping the sample in different solutions with increasing PS concentrations. (That will be the next procedure to be employed).

From our observations, procedure 1) does not assure an increase of the deposited mass, since after several depositions, an equilibrium state between the dissolved and deposited polymer is achieved, giving rise to saturation of the added mass. This has occurred during the measurements at different applied fields. Procedure 2), instead, gives a systematic increase of the deposited mass of PS after each dip coating process. For the dip coating processes described hereinafter the second procedure was used.

3.3.1. Fe-Co-Si-B metallic glass functionalized with polystyrene

For these experiments the ribbon of composition $Fe_{64}Co_{17}Si_{6.6}B_{12.4}$ was selected, as it has good magnetic and magnetoelastic properties ($\mu_0 M_S = 1.65\,T, \lambda_S = 20\,ppm, \Delta E\ effect \approx 22\%$). The melt spinning fabricated ribbon has a width of 1.6 mm and a thickness of 28 μm. The influence of the length on the sensitivity was studied: 3 cm, 2 cm and 1 cm length strips were coated with PS.

As previously explained, polystyrene depositions were made by the dip-coating technique. The magnetoelastic strips were immersed for 5 seconds in a polymer solution and let them dry at room temperature until total evaporation of the solvent. Successive depositions were made to follow the evolution of the change on the resonance frequency with the deposited mass. The samples were weighted after each deposition process and the resonance frequency was measured. A balance with a resolution of 0.1 μg was used to weight the amount of PS deposited in each dip coating process. For the polymer deposition, solutions of different polystyrene concentrations were prepared, from 10^{-5} M to 10^{-4} M, using tetrahydrofuran as solvent.

Tetrahydrofuran (THF) is an organic compound, specifically a cyclic ether with formula $(CH_2)_4O$. Being polar and having a wide liquid range is a versatile solvent, mainly used as a precursor to polymers. As it is a colourless, water miscible organic liquid with low viscosity it is also widely used as solvent for most organic compounds. It has been previously used for PS depositions onto metallic surfaces[10, 11]. It has low boiling point of 66 ℃, making it suitable for dip coating processes as it can be easily evaporated at room temperature.

After 6 deposition processes, the final topography of the obtained polymer film was observed by AFM. As it can be observed in Figure 3.6., the coated surface is not homogeneous; in fact, it seems that bubbles have formed during the evaporation process.

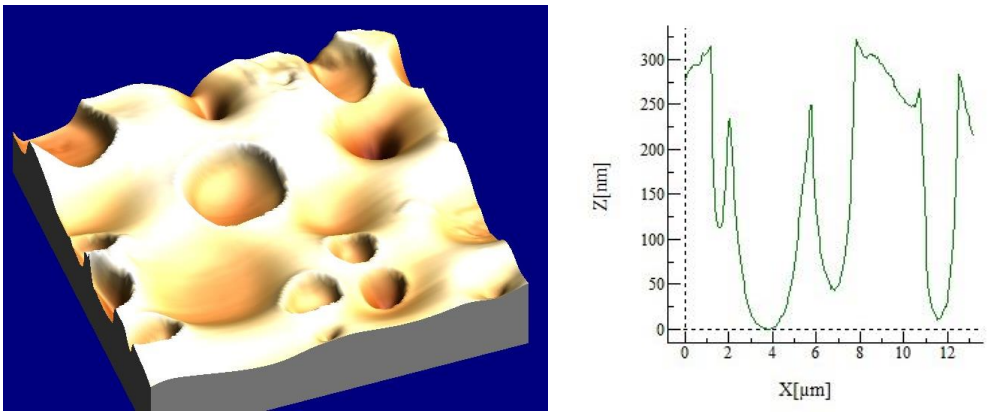

Figure 3.6. $100\ \mu m\ x\ 100\ \mu m$ AFM picture for PS (in THF) coated ribbon and its profile.

The presence of those spherical holes all over the PS film is probably due to the rapid evaporation of the THF. Besides, as THF is a water miscible solvent, and as the deposition and evaporation processes carried out without a controlled atmosphere, the obtained structure may be considered as breath figures. In a general breath figure process, a polymer solution in a high volatile solvent (as THF is) is cast onto a substrate under adequate humidity. The fast evaporation of the solvent temporally cooled down the solvent/air interface. This process induces the condensation of water from the humid air. Water droplets are arranged onto the surface ideally into a honeycomb pattern[12]. In this evaporation process as the humidity was not controlled and stable, the obtained structure is not well ordered, and the obtained holes have different sizes.

These large holes are an undesired consequence of a badly performed dip coating process occurring within the deposited film. Those holes can reach directly the surface of the amorphous ribbons and as a consequence leave the surface of the metallic ribbon exposed to any chemical agent of the atmosphere resulting in false resonance value that mistakes the desired detection, if any reaction takes place directly due to the contact with the metallic element.

A convenient alternative to THF solvent can be toluene, which is a non polar solvent with a higher boiling point (111 ℃). For the depositions with the new samples toluene will be used as solvent.

3.3.2. Fe-Ni-Cr-Si-B metallic glass functionalized with polystyrene

For these new set of experiments, the homemade corrosion resistance samples containing chromium will be used, in particular the one of composition $Fe_{54}Ni_{24}Cr_2Si_{10}B_{10}$ ($\mu_0 M_S = 1.22\,T, \lambda_S = 11.5\,ppm$, $\Delta E\ effect \approx 7\,\%$). The melt spinning fabricated ribbon has a width of 1.8 mm and a thickness of 30 μm, and in this case, samples of 1 cm length will be coated with PS.

As in the previous experiments with polystyrene, successive polymer depositions were made by the dip coating process with solutions of increasing concentrations. The 1 cm length samples were cleaned and treated as in the previous experiments in order to ensure a good attachment between the PS and the ribbon surface. Solutions of different PS concentrations were prepared, from 10^{-5} M to 10^{-4} M, using toluene as solvent. The ribbons were immersed for 5 seconds in the polymer solution and let them dry at room temperature. In this case, due to the solvent higher boiling point, the samples required more time to totally evaporate the solvent. After making the deposition the samples were weighted and the resonance frequency was measured with the spectrum analyser.

Toluene is a mono substituted benzene derivative, consisting of a methyl group attached to a phenyl group. The non polar character of the toluene and it higher boiling point will make it to evaporate at a slower rate than THF, and even more, as it is water-insoluble liquid breath figures should not be formed during the solvent evaporation consequently avoiding the hole formation observed in the THF case.

After 9 deposition processes, the final topography of the obtained polymer film was observed by AFM. As it can be observed in Figure 3.7. the polymer coating obtained using toluene as solvent of the polystyrene is more homogeneous than the obtained using THF as solvent. It is not totally smooth, but there is no signal of the previously obtained holes, so it can be supposed that the ribbon surface is totally covered with the

polymer. Therefore, the deposition process has been improved by changing the PS solvent.

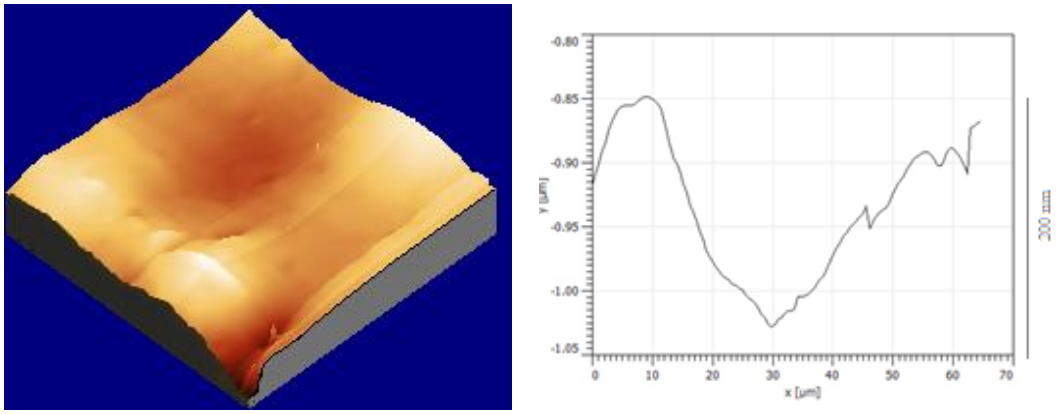

Figure 3.7. $100\ \mu m\ x\ 100\ \mu m$ AFM picture for PS (in toluene) coated ribbon and its profile.

The result obtained for the resonance frequency will be shown and discussed in Section 3.4.

3.4. A comparison between theoretical predictions and experimental results

3.4.1. PS depositions onto Fe-Co-Si-B resonant platforms

As theory predicts, the resonance frequency depends on the length of the ribbon Equation [1.3]. So the shorter the ribbon, the higher its magnetoelastic resonance frequency value, as it has been determined by measuring those resonance frequencies at 67, 102 and 206 kHz for the 3, 2 and 1 cm ribbon lengths, respectively (see Figure 3.8). These samples are covered with PS using THF as solvent.

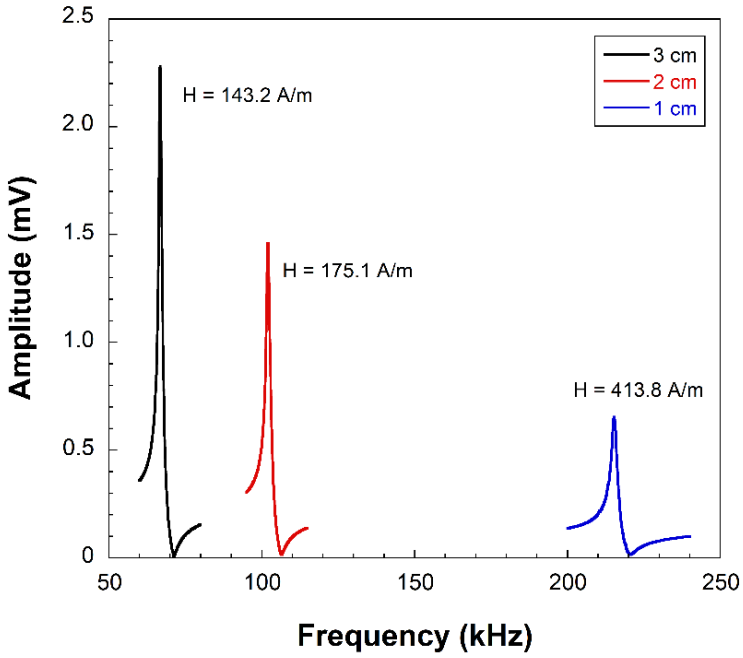

Figure 3.8. Magnetoelastic resonance curves obtained for the clean studied ribbons at an applied H_k corresponding to the minimum in measured ΔE curves.

As it has been previously explained, the sensitivity is a key factor when the magnetoelastic resonator is used for sensing purposes. Table 3.2. shows the calculated sensitivity values for the different length samples after several deposition processes.

Table 3.2. Sensitivities obtained for the different length samples covered with polystyrene dissolved in THF.

$L\ (mm)$	$\lvert S\rvert\ (Hz/\mu g)$	$1/\lvert S\rvert\ (ng/Hz)$
30	7.5	133.3
20	181	55.2
10	52.4	19

As expected, the most sensitive device to the deposited polymer mass is the smallest one, L = 1 cm with 19 ng/Hz detected mass value

per resonance frequency change. This has been also the device with the highest $Q = 155$ value.

Concerning the change of the resonant frequency of the samples with the deposited polymer mass, it is widely accepted that the basic equation that governs the magnetoelastic resonance based detection processes is:

$$\frac{\Delta f}{f_0} = -\frac{1}{2}\frac{\Delta m}{m_0} \qquad [3.3]$$

where m_0 is the original mass of the magnetoelastic platform that resonates at f_0 and $\Delta f = f - f_0$ is the resonant frequency change when a Δm uniformly deposited mass quantity is attached to the device. However, Equation [3.3] is just an approximation of a more general expression[13]:

$$\frac{f}{f_0} = \left[1 + \frac{\Delta m}{m_0}\right]^{-1/2} \qquad [3.4]$$

that can be expanded as:

$$\frac{\Delta f}{f_0} \approx -a\left(\frac{\Delta m}{m_0}\right) + b\left(\frac{\Delta m}{m_0}\right)^2 \qquad [3.5]$$

with $a = 0.5$ and $b = 0.375$. Such a second order expression agrees with our experimental observations for the relative change in the resonant frequency of each resonant platform as subsequent depositions were performed, and so the deposited mass increases in a continuous way for each of them. The obtained curves are shown in Figure 3.9.

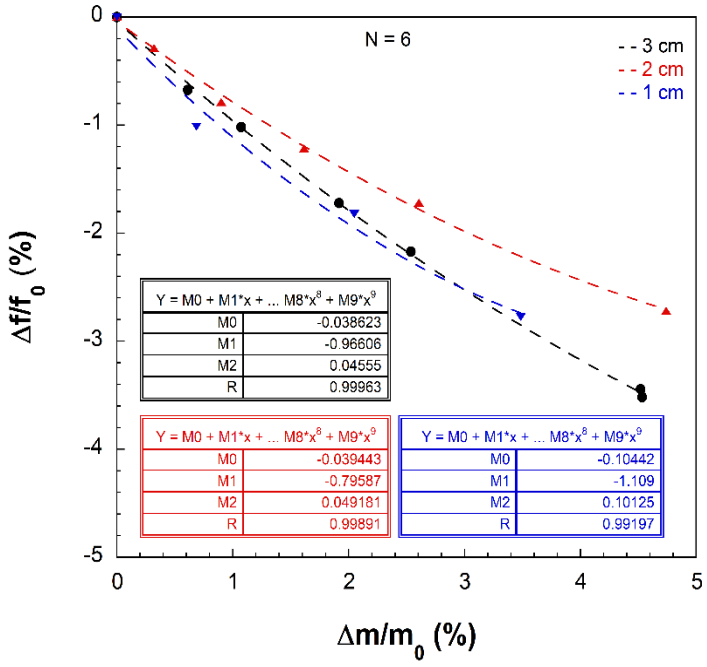

Figure 3.9. Change of resonant frequency versus deposited PS mass change, for all the different length ribbon.

Nevertheless, the values of the coefficients *a* and *b* obtained from such numerical fits presented in Table 3.3 (all of them with a 0.99 regression factor) clearly differ from the expected values.

Table 3.3. *a* and *b* coefficients obtained from the fit of equation 3.3 to the experimental data shown in Figure 3.9.

$L\ (mm)$	a	b
30	0.966	0.045
20	0.796	0.049
10	1,109	0.101

In Figure 3.10. it can be directly seen how the estimated height changes with the number of depositions N made (average, of course, since the formed holes by the solvent bubbles during the evaporation process have not been taken into account). As expected, the relative deposited mass amount is higher for L=1 cm than for L=3 cm, and therefore in this graph the increasing trend quickly separates from linearity (in the case L=1 cm).

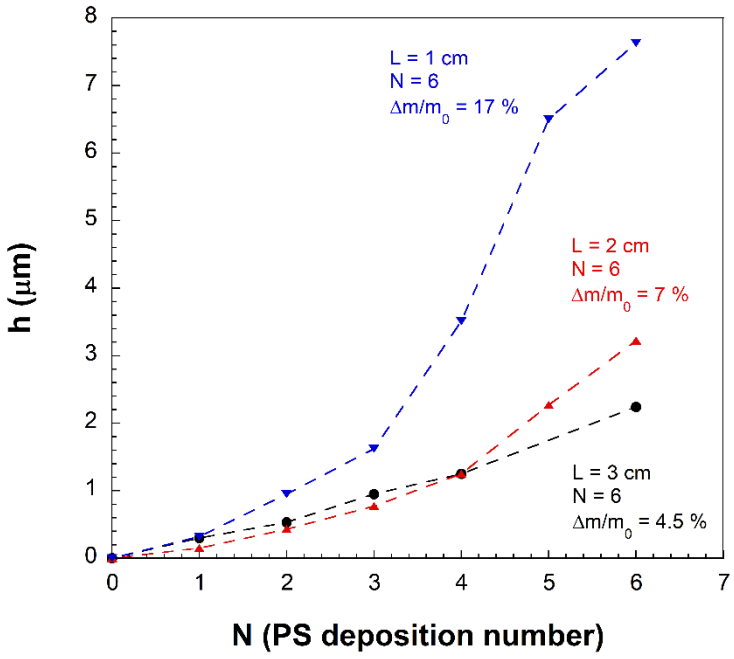

Figure 3.10. Change on the height of deposited polystyrene with the increasing number of depositions N for the three studied lenghts.

In Figure 3.11. the previous data shown in Figure 3.10. have been normalized, taking as parameter the relative change in mass for both tape lengths. It can be observed that the expected linearity in the resonance frequency change is achieved only for low relative mass changes, up to 4.5% as the upper limit in this change. For larger mass relative changes, this good initial linearity is lost.

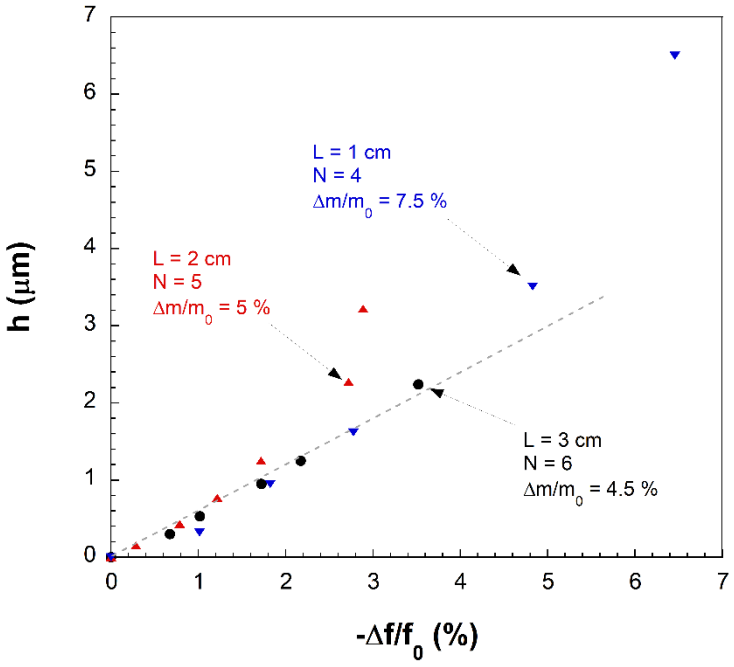

Figure 3.11. Mass changes on the height with the increasing number of depositions N, up to a 4 – 5 % as the upper limit of the linearity.

3.4.1. PS depositions onto Fe-Ni-Cr-Si-B resonant platforms

In the case of the $Fe_{54}Ni_{24}Cr_2Si_{10}B_{10}$ resonant ribbons, in which the PS depositions were made using toluene as solvent, only 1 cm ribbons were used since they show the highest sensitivity. The results obtained for the change of the resonant frequency with the increasing deposited polymer mass are shown in Figure 3.12.

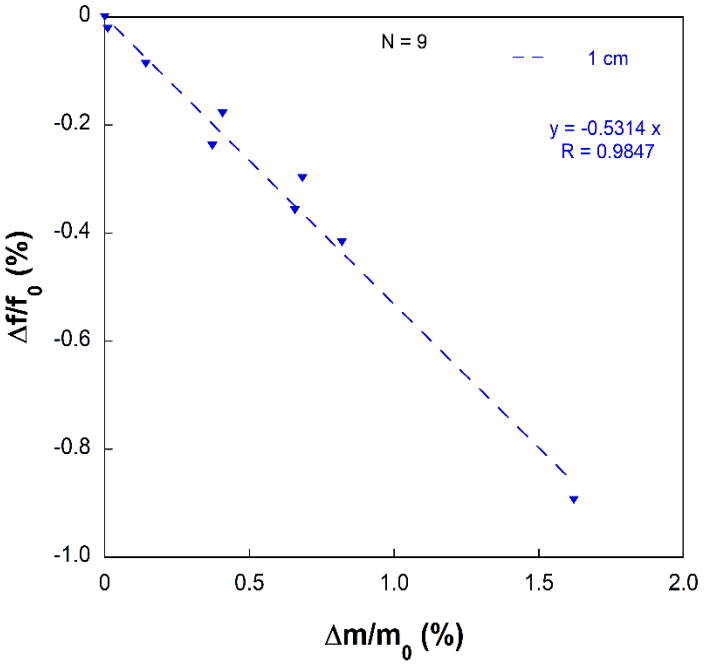

Figure 3.12. Change of resonant frequency versus deposited PS mass change for the toluene solvent sample.

Two facts deserve further explanation: firstly, the differences between the deposited mass amount in both cases, using different solvents; and secondly the obtained correlation between the mass increment and the resonance frequency displacement.

Concerning the polymer deposition, the dip coating process being followed has been the same for both samples by using different solvents. In both cases, solutions of increasing polymer concentration have been used to ensure the mass increase with the increasing number of coating processes. Nevertheless, for the FeCoSiB sample with 6 deposition processes the mass increment achieved was of about 5 %, while for the FeNiCrSiB with 9 depositions has been less than 2 %. This fact can be attributed to the solvent differences. Both solvents are cyclic organic compounds where PS is soluble, however THF is a polar solvent which is miscible with water while toluene is a non polar solvent which is water insoluble. The polarity and solubility differences between the solvents can influence the wettability of the resonant platform being the responsible of the polymer adherence onto the surface of the magnetoelastic material. If the wettability of the surface to a solvent is

low, the PS will have worse adherence to the ribbon surface, as the solvent will not spray all over the surface, and therefore the deposited mass will be smaller. On the contrary, if the wettability is high, the PS solution will spray through the whole surface letting the PS properly adhere to the metallic ribbon and increasing the deposited mass amount. But this cannot be the only factor, it can also be influenced by the ribbon composition, as the PS adherence can be improved or not depending on the substrate composition.

On the other hand, and concerning the mass versus resonance frequency shifts, it has been observed that when the mass change is less than 2 %, the experimental data obtained fits the linear expression of Equation [3.3]. Furthermore, the obtained slope value -0.53 is really close to the theoretical one, which is -0.5. Nevertheless, when the coating material mass is higher the experimental data fits better with the polynomial expression given in Equation [3.5], as it has been observed for the THF solvent samples. Following this line of reasoning, it can be concluded that the linear expression can be useful when the relative mass change is small, while for situations where the relative mass change is higher the second order polynomial expression must be employed.

3.5. Summary and conclusions

The results shown in this chapter demonstrated that it is possible to coat a magnetoelastic material with a polymer as polystyrene acting as active layer. It has been observed that due to the high rugosity of the as quenched amorphous ribbons, a previous acid treatment is needed to ensure the good adherence between the magnetoelastic strip and the polymer.

It has also been observed that there are several factors affecting the polymer depositions by the dip coating technique. For example, in order to homogeneously coat the magnetoelastic ribbons solutions of

increasing concentrations are needed in order to be sure that the polymer deposited mass will systematically increase. If the samples are dipped in a constant concentration solution for several times, after several depositions, an equilibrium state between the dissolved and the deposited polymer can be achieved, giving rise to saturation of the added mass. To avoid this problem, the dipping process must be performed with solutions of increasing polymer concentrations.

Another important parameter that must be taken into account, is the solvent used to prepare the polymer solutions. It has been observed that depending on the solvent nature, the obtained film will be different. For the THF, which is a polar solvent with a boiling point of 66 ℃, an inhomogeneous film surface was obtained. As it was observed in the AFM images, the topography of the deposited polymer film was full of bubbles and holes, due to the solvent high evaporation rate at room temperature, and probably due to humidity. On the contrary, the toluene solvent samples, presented a more uniform polymer layer, as toluene is a nonpolar solvent with a higher boiling point, of 111 ℃, comparing with the THF and that is less miscible in water, so it is less affected by ambient humidity.

However, it has not been possible to deposit as much mass using toluene as THF, probably due to the differences between the solvents and the nature of the chosen magnetoelastic materials. As the polarity and water miscibility of the employed solvents are different, it has affected PS deposition processes. For the THF coated samples, the mass increment has reached 5 %, while for the toluene samples it has been less than 2 %. This fact can be attributed to the solvent wettability, due to its polarity properties. Probably, the ribbon wettability with toluene is lower, therefore, PS solution does not spray properly through the metallic platform and PS adherence becomes worse what leaves less polymer coating the resonant platforms in each dip coating process. More studies about the influence of the solvent and the influence of the substrate must be performed.

Concerning the studied magnetoelastic parameters, the most sensitive device to the deposited mass is, as expected the smallest one (L=1 cm) with in fact the highest Q value. Linearity has been observed in

the initial deposition processes when the deposited mass is actually small. Nevertheless, theoretical prediction about the linear dependence of higher mass change values to resonant frequency change with expected slope (-0.5) needs of a deep revision.

References

[1] C.A. Grimes, W.R. Seitz, J.L. Horn, S.A. Doherty and M.T. Rooney, "A remotely interrogatable magnetochemical pH sensor", IEEE Transactions on Magnetics 33 (1997) 5, 3412-3414. DOI: 10.1109/20.617961.

[2] P.G. Stoyanov, S.A. Doherty, C.A. Grimes and W.R. Seitz, "A remotely interrogatable sensor for chemical monitoring", IEEE Transactions on Magnetics 34 (1998) 4, 1315-1317. DOI: 10.1109/20.706533.

[3] C.A. Grimes, C.S. Mungle, K. Zeng, M.K. Jain, W.R. Dreschel, M. Paulose and K.G. Ong, "Wireless magnetoelastic resonance based sensors: a critical review", Sensors 2 (2002) 7, 294-313.DOI: 10.3390/s207002294.

[4] Z. Kaczkowski, "Piezomagnetic dynamic as new parameter of magnetostrictive materials and transducers", Bulletin of the Polish Academy of Sciences: Technical Sciences (1997) 45 (1), p. 17-42. ISSN: 0239-7528.

[5] A.C. Lopes, A. Sagasti, J. Gutiérrez, V. Muto, A. Lasheras and J.M. Barandiarán, "Determining the Q-factor in magnetoelastic resonant sensors" (in preparation)

[6] K. Zhang, L. Zhang, L. Fu, S. Li, H. Chen and Z.Y. Cheng, "Magnetostrictive resonators as sensors and actuators", Sensors and Actuators A: Physical 200 (2013) 2-10. DOI:10.1016/j.sna.2012.12.013.

[7] L. E. Scriven "Physics and applications of dip coating and spin coating" Symposium H – Better Ceramics Through Chemistry III 121 (1988) 717-729. DOI: 10.155/PROC-121-717.

[8] M.N. Rahaman, "Ceramic progressing" Boca Raton: CRC Press (2007) 242-244. ISBN: 00-8493-7285-2.

[9] D. Quéré, "Fluid coating on a fiber" Annual review of fluid mechanics 31 (1999) 1, 347-384. DOI: 10.1156/annurev.fluid.31.1.347.

[10] H. Xu and J.B. Schlenoff, "Kinetics, isotherms, and competition in polymer adsorption using the quartz crystal microbalance" Langmuir 10 (1994) 1, 241-245. DOI: 10.1021/la00013a035.

[11] S.J. Xia, G. Liu and V.I. Birss, "Properties of thin flim polystyrene films prepared on gold electrodes by the dip coating method" Langmuir 16 (2000) 3, 1379-1387. DOI: 10.1021/la9907735.

[12] L. Ruiz-Rubio, I. Azpitarte, N. García-Huete, J.M. Laza, J.L. Vilas and L.M. León, "Solvent and relative humidity effect on highly ordered polystyrene honeycomb patterns analysed by Voronoi tessellation", Journal of Applied Polymer Science 133 (2016) 39, 4404 (9 p.).DOI: 10.1002/APP.4404.

[13] P.G. Stoyanov and C.A. Grimes, "A remote query magnetostrictive viscosity sensor", Sensors and Actuators A; Physical 80 (2000) 1, 8-14. DOI: 10.1016/S0924-4247(99)00288-5.

4. Magnetoelastic resonant platforms for biological detection

This fourth chapter introduces the magnetoelastic resonant platforms to develop biological sensors. It will be focused on the study of several methods to functionalize the magnetoelastic strip surfaces with zinc oxide (ZnO) to make it sensitive to the final target analyte. In this entire chapter, the magnetoelastic material is a commercial Metglas 2826MB3. After comparing the different functionalization methods, the best one will be used to deposit a zinc oxide thin film and by performing magnetoelastic resonance measurements we will determine the elastic modulus of that deposited layer. Finally, bio-detection experiments will be carried out by immobilising hemoglobin onto the zinc oxide film with the aim of being able to detect the presence of H_2O_2. Thus and, after construction of a small sensing device, the oxidation of the hemoglobin by H_2O_2 will be monitored simultaneously by two different techniques, magnetoelastic resonance method and cyclic voltammetry measurements.

4.1. Introduction

Zinc oxide is an inorganic compound with formula ZnO. It is a rather common material used for a quite large variety of different applications, such as an additive in numerous daily life materials and products, including rubbers, plastics, ceramics, glass, adhesives, pigments, foods, batteries and so on[1]. Although it occurs naturally as the mineral zincite, most zinc oxide is synthetically produced.

ZnO occupies a special place among wide bandgap semiconductors of the II-VI group, as it possesses several favourable properties such as, good transparency, high electron mobility, high radiation, high room-temperature luminescence and chemical and thermal resistance[2]. Those properties have made zinc oxide valuable in some emerging applications such as, transparent electrodes, energy-saving or heat-protecting windows, thin film transistors or light emitting diodes[3].

Most of the group II-VI binary compound semiconductors crystallise in either cubic zinc blende or hexagonal wurtzite structure, where each anion is surrounded by four cations at the corners of a tetrahedron, and vice versa. This tetrahedral coordination is typical of sp^3 covalent bonding nature, but these materials also have a substantial ionic character that tends to increase the bandgap beyond the one expected from the covalent bonding. ZnO is an II-VI compound semiconductor whose ionicity resides at the borderline between covalent and ionic semiconductors. The crystal structures shared by ZnO are hexagonal wurtzite, cubic zinc blende and cubic Rochelle salt. Under ambient conditions, the thermodynamically stable phase is that of wurtzite symmetry. On the other hand, the zinc blende structure can be stabilised only by growth on cubic substrates and the Rochelle salt metastable structure may be obtained at relatively high pressures. Figure 4.1 shows a representation of the ZnO crystal structures.

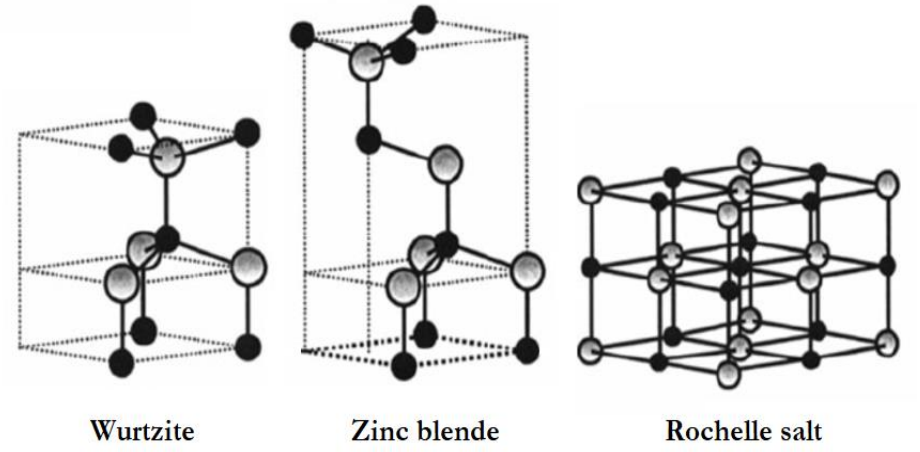

Figure 4.1. Representation of the ZnO crystal structures (hexagonal wurtzite, cubic zinc blende and cubic Rochelle salt). Grey spheres denote Zn atoms, and black spheres denote oxygen atoms.

The wurtzite structure has an ABAB hexagonal close packing (HCP) structure, belonging to the space group $P6_3mc$, and it is characterized by two interconnecting sublattices of Zn^{2+} and O^{2-}, such that each Zn ion is surrounded by a tetrahedral of O ions, and vice versa. The Zn^{2+} and O^{2-} ions create a normal dipole moment and an instant polarization, which results in a diversification of surface energy. Therefore, the tetrahedral coordination in ZnO results in a noncentral symmetric structure giving rise to polar symmetry along the hexagonal axis. This polarity is responsible for a number of properties of the ZnO, including its piezoelectricity, pyroelectricity and spontaneous polarization, and it is also a key factor in crystal growth, etching and defect generation[4].

At the nanoscale, ZnO presents diverse range of possible structures and morphologies such as nanospheres, nanoflowers, nanowires[5,6], nanorods, nanobelts[7], nanobridges[8], nanonails[8], nanohelices[9], tetrapods[10] and comb-like nanostructures[11]. The structure and morphology of the obtained nanoparticles depends on the synthesis method, which can take place through various routes including sol-gel processes, chemical coprecipitation, chemical vapour deposition, metal-catalysing growth, thermal evaporation, hydrothermal synthesis, solid-state reactions, among others[12].

Wurtzite ZnO is one of the key wide-band-gap (3.437 eV) semiconductors and has a relative large excitation binding energy

(60mV). Owing to these unique properties, ZnO is attracting much attention for a variety of electronic and optoelectronic applications. Some advantages associated with that large bandgap include high-temperature and high-power operation, low noise generation, high breakdown voltages and ability to sustain large electric fields. Besides, the lack of a centre of symmetry in wurtzite, combined with the large electromechanical coupling, results in strong piezoelectric and pyroelectric properties and the consequent use of ZnO in mechanical actuators and piezoelectric sensors. In fact, it is already widely utilised not only in piezoelectric transducers[13] or sensors[14] (including chemical sensors), but also in varistors, phosphors[15], solar cells[16], luminescence devices and transparent conducting films. This particular semiconductor has attracted also such interest due to its excellent chemical and thermal stabilities.

ZnO with a wurtzite structure naturally becomes an n-type semiconductor due to the presence of intrinsic and extrinsic defects, which are generally attributed to native defects, such as the Zn-on-O antisites, the Zn interstitial and the O vacancies. Various forms of ZnO exhibit two luminescence bands, a short wavelength band, which is located near the absorption edge of the crystal, and a broad long wavelength band, the maximum of which usually, is in the green spectral range. As far as the green luminescence is concerned, despite a huge number of investigations, its nature is yet to be understood. However, several structural defects, such as: zinc vacancies[17,18], oxygen vacancies[19,20], interstitial zinc ions[21] or oxygen antisites[22], among others have been considered responsible for the green luminescence by different authors[23]. Nevertheless, successful p-type doped ZnO structures have also been reported. P-type and n-type nanowires, for example, can serve as p-n junction diodes and LEDs, and fields effect transistors (FETs) can be fabricated from then to make complementary logic circuits.

But not only in electronic applications, as it was previously mentioned ZnO has a wide range of applications in very different fields. ZnO is used in rubber manufacturing for activating the vulcanisation process, being also a very important additive in car tyres as it improves the thermal conductivity, which helps the tyres to dissipate heat quickly. Fine particles of ZnO have antimicrobial and deodorising qualities and

hence they are used for packaging purposes. These properties along with its ability of neutralising acids makes it ideal for being used in antiseptic creams, healing creams or as component of toothpastes and dental prosthetics. Furthermore and due to its ability to absorb ultraviolet light, ZnO is also used in sunscreens and sunblocks to prevent sunburns. Besides, ZnO is usually added to food products as a source of zinc, which is considered to be a necessary nutrient as it helps in the performance of various physiological activities. Finally, and since as zinc oxide is an excellent inhibitor of fungi, mildew and mould, is extensively used as additive for anti corrosive coatings, for example in paints.

The experimental part of this chapter has been developed at the Department of Material Science in the University of Patras (Greece), the Foundation for Research and Technology (FORTH) and the Institute of Chemical Engineering Science in Patras (Greece) under the supervision of Dr. Nikolaos Bouropoulos, Dr. Dimitris Kouzoudis and Dr. Emmanuel Topoglidis and with the help of Apostolos Panagiotopoulos.

4.2. Detection by ZnO functionalized magnetoelastic resonant platforms

The study of zinc oxide material and its employment in micro-scale and nano-scale devices has grown tremendously during last decade. As it waspreviously mentioned, zinc oxide is a very versatile material that can be used in many microsystems. The combination of its wide band gap, piezoelectric, electrical and optical properties makes ZnO unique and crucial for a wide range of device applications. Due to its high electromechanical coupling coefficient, ZnO is one of the leading candidates for efficient signal transduction between electrical and mechanical domains in both sensors and actuators. Furthermore, ZnO also stands out from other materials because of its ability to operate in extreme conditions such as nuclear reactors and space, due to its better radiation hardness if compared to other materials used for such purposes.

In particular, the piezoelectric characteristics of ZnO make it an outstanding transducer material for making microelectromechanical systems (MEMS), resonators and mechanical switches. These small resonators are useful in wireless communication systems where small size, low power consumption and the ability for on-chip integration with microelectronics are greatly appreciated. Piezoelectrically-actuated resonators in bulk acoustic wave (BAW) mode have been widely used in wireless communicators providing piezoelectric MEMS resonators to succeed in wireless world.

Another application of ZnO piezoelectric effect is employed in mass-sensitive sensors, which are based on the acoustic wave phenomena. These transducers can be used for chemical and biological monitoring devices where the resonant frequency strongly depends on the amount of external mass attached to the resonator. ZnO is also a biocompatible material, and therefore it can be used for many biomedical applications such as biomedical implants and coatings.

In this chapter, the functionalization of commercial ferromagnetic magnetoelastic strips with zinc oxide will be presented. Different deposition methods will be studied to achieve the most homogenous deposited layer of ZnO. From the sample with the best deposited and formed active layer, studies to determine the Young Modulus of the deposited ZnO film will be carried out. Finally, these samples will be tested for biodetection purposes. Hemoglobin will be attached onto the zinc oxide layer in order to make the system sensitive to the reactions with hydrogen peroxide. This detection process will be performed simultaneously by two different methods, cyclic voltammetry curves and magnetoelastic resonance measurements.

4.2.1. ZnO deposition process study onto MRPs

In which concerns the following experimental work, the magnetoelastic material used as base layer for the ZnO deposition processes is a commercial long ribbon of Metglas 2826MB3 ($Fe_{40}Ni_{38}Mo_4B_{18}$) purchased from Hitachi Metals Europe GmbH

(Dusseldorf, Germany). This has $6\,mm$ width and $29\,\mu m$ thickness. The ribbon was cut in pieces (strips) of $2\,cm$ length, cleaned with analytical grade acetone purchased from Sigma-Aldrich under sonication for 15 minutes to remove any dirt from the fabrication or manipulation processes and finally dried at room temperature. These strips with the ZnO already deposited on them, will be used afterwards as resonant platforms for sensing purposes.

Once the samples were cut and cleaned, the subsequent functionalization of the resonant platforms was carried out by three different techniques:

- Direct precipitation from a mixture of solutions
- Seeding procedure and later precipitation process
- Casting technique by evaporation of the solvent

The main objective is to compare them by studying the formed structures and compositions, morphology and homogeneity of the deposited layers. To do this, the obtained deposited layers will be characterized using different techniques as X-Ray Diffraction (XRD), Scanning Electron Microscopy (SEM or Photoluminescence Emission (PL).

As it was previously mentioned, the magnetoelastic material for these tests will be the commercial Metglas 2826MB3. The ribbons were cut in pieces of 2 cm length, cleaned with analytical grade acetone under sonication for 15 minutes and finally dried at room temperature.

Once the strips were cut and cleaned, they were weighted and the resonant frequency measured (112 kHz). The subsequent functionalization of the Metglas 2826MB3 resonant platforms with a ZnO layer was carried out by three different techniques. The methodologies employed and studies performed to characterize the fabricated ZnO layers were:

- Direct precipitation from a mixture of solutions
    - Time dependence
    - Zn concentration dependence

- Seeding procedure and later precipitation process
    - Zinc acetate particles
    - Zinc oxide particles
- Casting technique by evaporation of the solvent
    - Zinc oxide particles

With the best obtained Metglas 2826MB3 + ZnO layer sample other studies will be subsequently performed as the determination of the Young modulus measurement of the deposited zinc oxide layer and a biodetection experiment to show a final possible application of the developed system.

All the precipitation reactions, both for the direct precipitation procedures and for the precipitations after the seeding procedures, were performed by mixing a sodium hydroxide $0.1\,M$ solution ($NaOH\ 0.1M$) with zinc nitrate $0.2\,M$ solution ($Zn(NO_3)_2\ 0.2M$) under different conditions to study the factors that may have influence on the formation of the precipitate. Both reactants were purchased from Sigma. Those conditions will be detailed in each procedure in a table to ease the understanding of each process.

- Direct precipitation process: Time dependence

Different samples were prepared by mixing the same amount of reactants at the same temperature conditions but varying the reaction times. In Table 4.1, the sample preparation conditions are shown. The Metglas 2826MB3 strips were put in a glass vial with the rough side up and fixed to the bottom of the vial with an external magnet in order to add the solutions and avoid the sample movement. Both solutions were then added to the glass vial with micropipettes. When adding the $Zn(NO_3)_2$ solution some turbidity appeared, due to the quickly formation of the precipitate of zinc hydroxide, so the final mixture was manually shaken until the turbidity disappeared so it has been well homogenised. After this, the external magnet was removed and the glass vial was closed and let into the oven at 65 ℃ for different precipitation times. Several

depositions were made following this procedure. At each precipitation process, the samples were cleaned by rinsing them with ethanol and dried at 65 ℃, weighted and subsequently measured the corresponding resonance frequency, to follow the evolution of the loaded mass with the resonant frequency change. Some white precipitates were observed onto the deposited surface.

Table 4.1. Sample preparation conditions for the time dependence study by direct precipitation process.

Sample	***Reactants***	***Temperature*** (℃)	***Time*** (***min***)
***M*1_18**	$10\ ml\ NaOH\ 0.1\ M$ + $0.2\ ml\ Zn(NO_3)_2\ 0.2\ M$	65	**90**
***M*2_18**			**60**
***M*3_19**			**30**

In Figure 4.2 XRD patterns of the prepared samples and some useful materials as references, as pure zinc oxide (wurtzite structure) and zinc hydroxide patterns, are shown. As it can be observed, for the shorter precipitation time, sample M3_19, 30 minutes, there is a mixture in the deposited layer formed by zinc hydroxide and zinc oxide with a clear predominance of the hydroxide structure (the peaks related with the hydroxide structure are more intense that the ones that correspond to the zinc oxide structure). On the other hand, when the reaction time is longer, of 60 or 90 minutes, the obtained patterns reveal only the presence of ZnO in the structure of the deposited material, with no other peaks appearing.

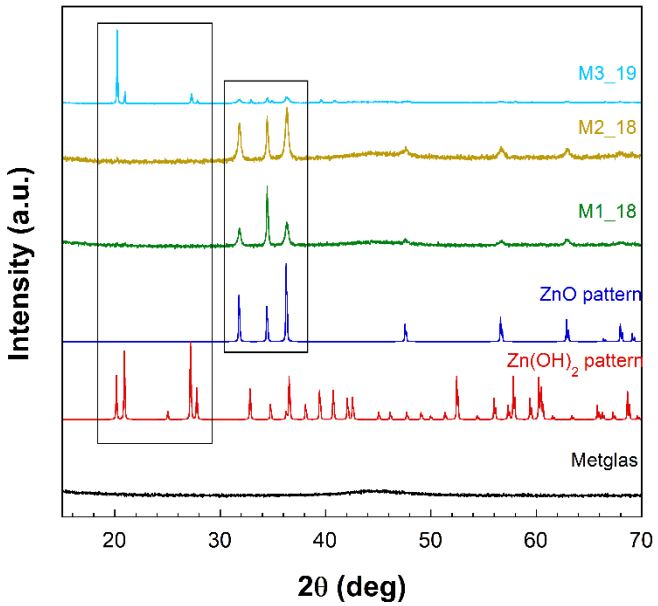

Figure 4.2. X-ray spectra for the samples of the deposited layers by direct precipitation at different times and ZnO and $Zn(OH)_2$ patterns to compare the obtained precipitates.

The obtained XRD results are in good agreement with the SEM analysis, as it is shown in Figure 4.3. In the case of the samples with longer reaction times, where all the formed precipitate is ZnO, a flower-like morphology can be observed on the fabricated layer. However, for the shorter reaction time sample, two different structures were observed due to the mixture of ZnO and $Zn(OH)_2$. Not only flower-like grains corresponding to the ZnO were observed, but also other hexagonal structures which are related to the $Zn(OH)_2$ (wulfingite) structures. In Table 4.2, the conclusions obtained from each conditions are summarised.

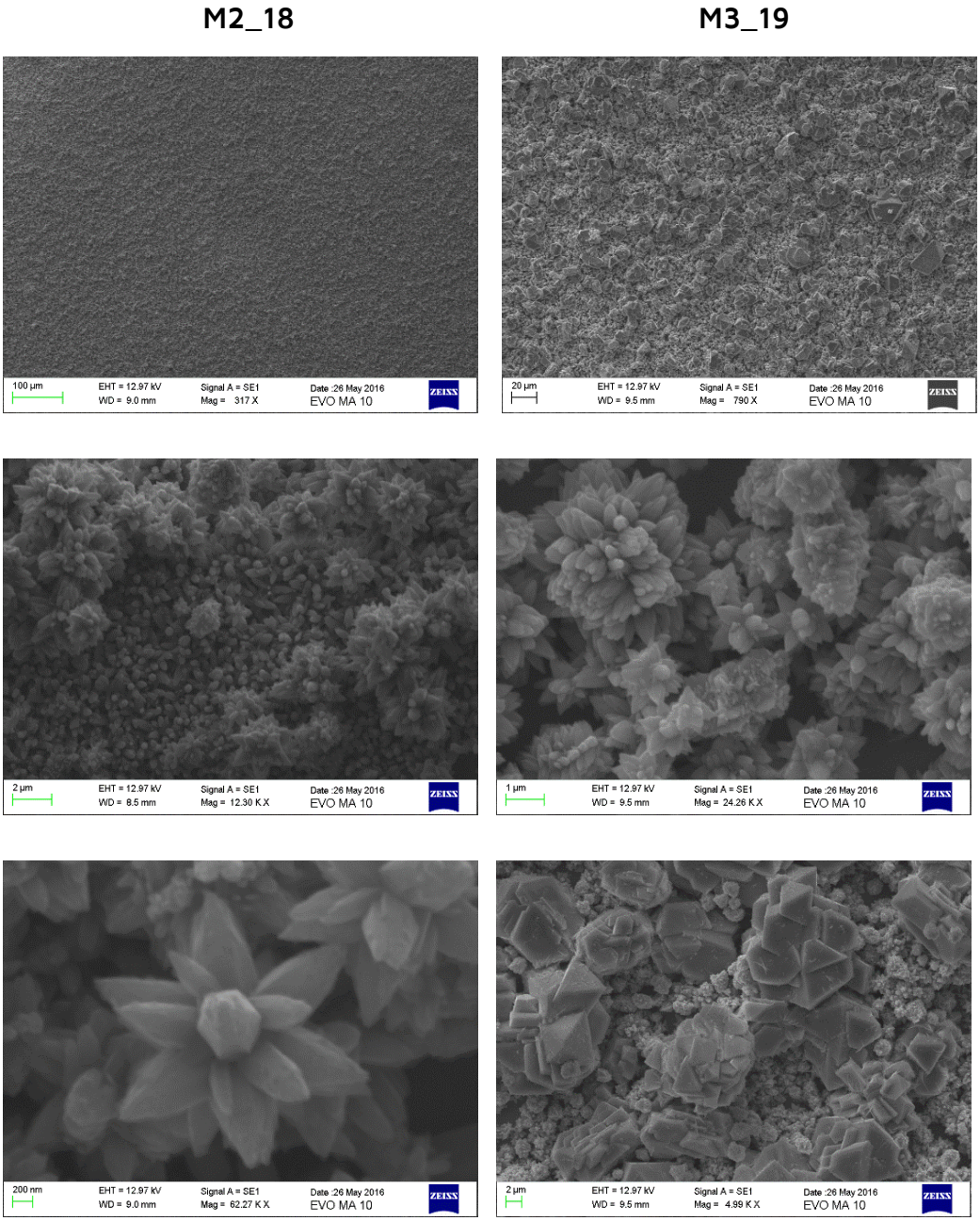

Figure 4.3. SEM images of two different time precipitation samples. M2_18 (60min), flower structure of ZnO layer. M3_19 (30min), flower structure of ZnO and hexagonal structures of $Zn(OH)_2$.

Table 4.2. XRD and SEM characterization results (final product and morphology) for the precipitation layers formed at different precipitation times.

$\boldsymbol{Sample}$	$\boldsymbol{Time\ (min)}$	$\boldsymbol{XRD}$	$\boldsymbol{SEM}$
$\boldsymbol{M1\_18}$	90	ZnO	$Flowers$
$\boldsymbol{M2\_18}$	60	ZnO	$Flowers$
$\boldsymbol{M3\_19}$	30	$ZnO\ +\ Zn(OH)_2$	$Flowers\ +\ Hexagons$

It can be concluded that, through direct precipitation, it is possible to obtain a zinc oxide layer deposited onto the Metglas ribbon. For this purpose, the precipitation reaction must be performed allowing the detailed reaction to take place at 65 ℃ for precipitation times of at least of 60 minutes. If the reaction time is not enough a mixture of zinc oxide and zinc hydroxide will be obtained. The formed ZnO precipitate layer has a flower like structure, which is directly related with the conditions of the reaction. In the case of a mixed composition, hexagonal structures were observed due to the presence of wulfingite.

- Direct precipitation process: Zn concentration dependence

In order to study the influence of the zinc concentration on the formed precipitate structure, different samples were prepared by changing the initial quantity of zinc nitrate at the same temperature and time conditions. Table 4.3a and Table 4.3b show the different sample preparation conditions.

In Figures 4.4a and 4.4b, XRD patterns of the prepared samples are shown. As it can be observed, for the lower zinc concentration samples ($0.25\,ml$ or less) there is a mixture on the deposited layer of zinc oxide and zinc hydroxide. Besides, the deposited layer was not homogenous probably because there was not enough amount of reactants to form a homogenous and well distributed precipitate layer to cover the whole ribbon surface. For samples with higher concentrations of zinc nitrate, only zinc oxide formation has been observed.

Table 4.3a. Sample preparation conditions for zinc concentration dependence by direct precipitation.

	Reactants		
Samples	$V\ NaOH$ $0.1M\ (ml)$	$V\ Zn(NO_3)_2$ $0.2M\ (ml)$	***Conditions***
$M1\_20$	10	0.15	1 *day at room temperature* + 2 *days at* 65 ℃
$M2\_20$		0.20	
$M3\_20$		0.25	
$M4\_20$		0.30	
$M5\_20$		0.35	

Table 4.3b. Sample preparation conditions for zinc concentration dependence by direct precipitation.

	Reactants		
Samples	$V\ NaOH$ $0.1M\ (ml)$	$V\ Zn(NO_3)_2$ $0.2M\ (ml)$	***Conditions***
$M1\_31$	10	0.30	1 *day at room temperature* + 2 *days at* 65 ℃
$M2\_31$		0.35	
$M3\_31$		0.40	
$M4\_31$		0.45	
$M5\_31$		0.50	
$M6\_31$		0.55	
$M7\_31$		0.60	
$M8\_31$		0.65	

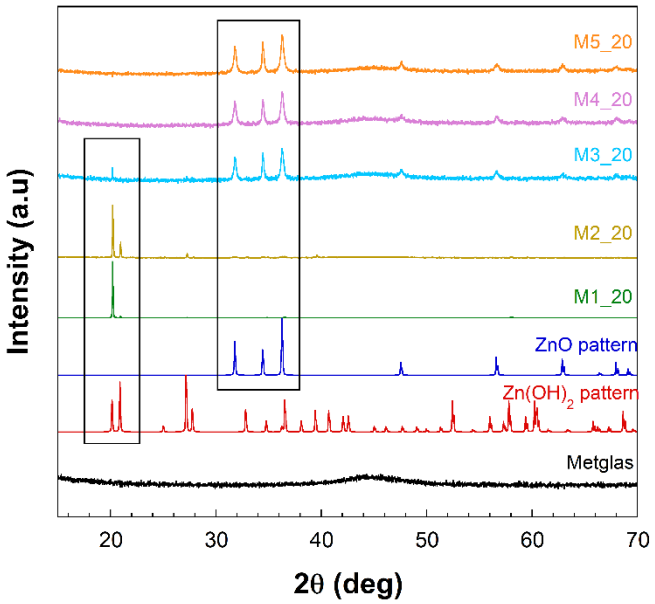

Figure 4.4a. X-ray spectra for the samples of the deposited layers by direct precipitation with different zinc nitrate initial concentrations.

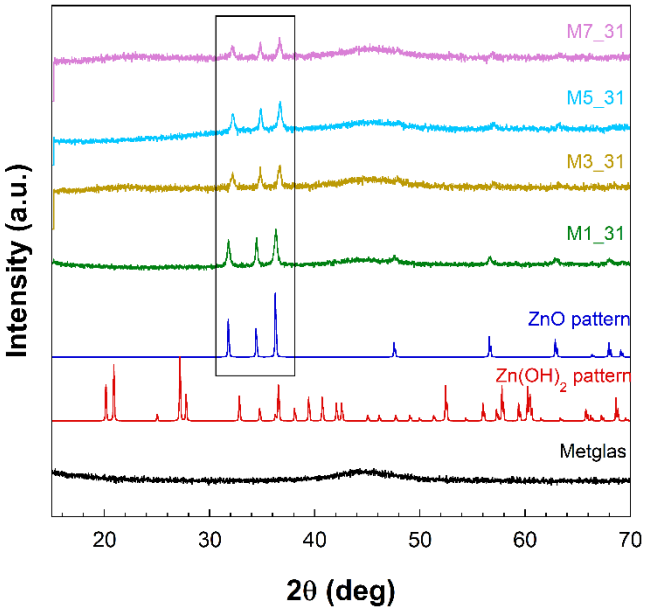

Figure 4.4b. X-ray spectra for the samples of the deposited layers by direct precipitation with different zinc nitrate initial concentrations.

The obtained SEM images, presented in Figure 4.5 show a completely different morphology compared with the previous ones, due to the synthesis conditions used that have been clearly different if compared to the time dependence study. Instead of ZnO particles in 'flower' type shape in this case 'sponge' like structures were obtained. In Table 4.4 the results obtained from XRD and SEM are summarised.

M3_31

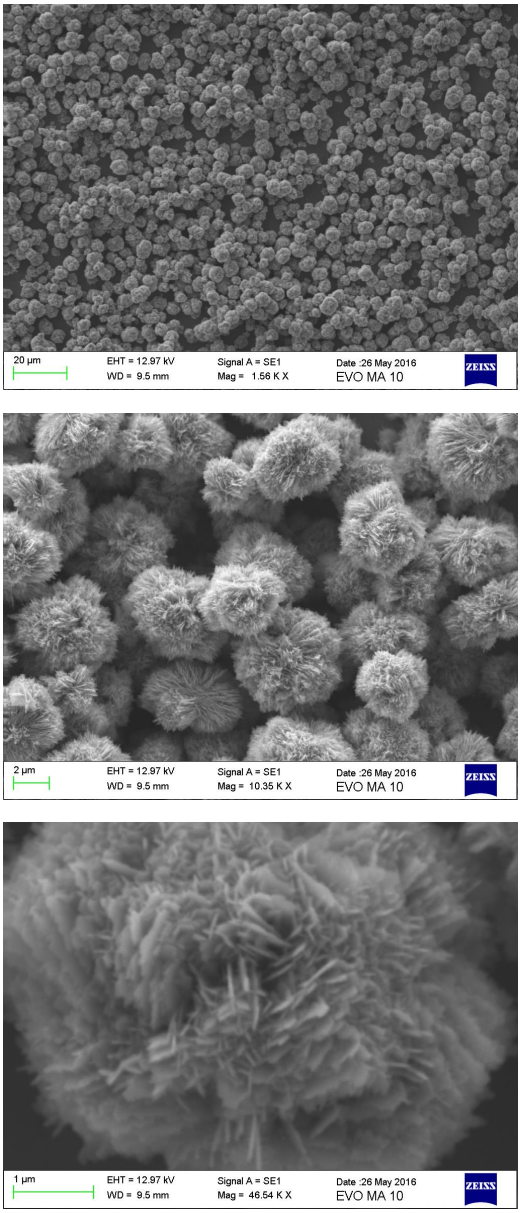

Figure 4.5. SEM images of M3_31 where ZnO precipitate has sponge like structure.

Table 4.4. XRD and SEM characterization results (final product and morphology) for the precipitation layers formed at different zinc nitrate initial concentrations.

Samples	$\boldsymbol{V\ Zn(NO_3)_2\ 0.2\ M\ (ml)}$	***XRD***	***SEM***
M1_20	0.15	$Zn(OH)_2 + ZnO$	–
M2_20	0.20	$Zn(OH)_2 + ZnO$	–
M3_20	0.25	$Zn(OH)_2 + ZnO$	–
M4_20	0.30	ZnO	*Sponges*
M5_20	0.35	ZnO	*Sponges*
M1_31	0.30	ZnO	–
M2_31	0.35	ZnO	–
M3_31	0.40	ZnO	*Sponges*
M4_31	0.45	ZnO	–
M5_31	0.50	ZnO	–
M6_31	0.55	ZnO	*Sponges*
M7_31	0.60	ZnO	–
M8_31	0.65	ZnO	*Sponges*

As a further characterization and proof of the quality of the formed precipitate and deposited ZnO layers, photoluminescence measurements were also carried out at room temperature.

Zinc oxide is a semiconductor which presents a wide and direct bandgap in the near UV spectral region (3.4 eV) and large exciton binding energy (~60 meV at room temperature). ZnO often exhibits a broad and weak green luminescence, centred between 2.2 and 2.4 eV. This green luminescence has been observed in samples prepared with a variety of techniques, and it is important to point out that there may not be a single source for this luminescence.

For instance, the presence of certain impurities has been suggested as a potential cause; nevertheless, samples without any impurities have shown also the green luminescence. Due to this fact, a native defect have also been suggested as a potential cause. Moreover, this is going to

be our hypothesis. As Reynolds and Kohan have suggested, that zinc vacancy can give rise to green luminescence. Indeed, the calculated transition level between the -1 and -2 charge states occurs at 0.9 eV above the valence band maximum and hence the transition between the conduction band and the acceptor level would give rise to luminescence around 2.5 eV, in good agreement with the observed transition energy. Besides, zinc vacancy is favoured under O-rich condition synthesis, as it will happen in the followed ZnO synthesis processes. As PL spectra are going to be present as function of the wavelength, in Figure 4.6 conversion between eV and nm can be observed.

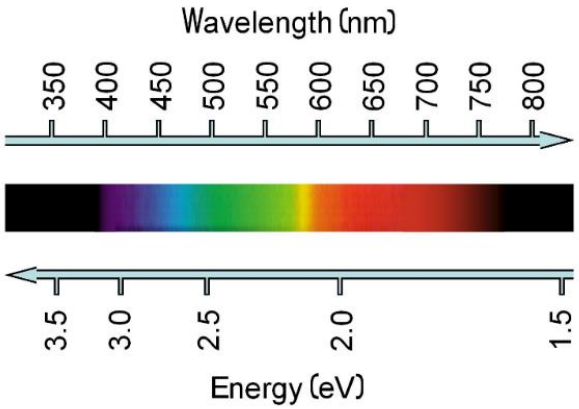

Figure 4.6. Spectrum of the visible light over the wavelength in nanometres and the photon energy in eV.

As afore explained, there is not a clear agreement for the explanation of the green luminescence emission of the ZnO. In our case, the origin of such green broadband that can be observed in Figure 4.7 can be attributed to zinc vacancies. Firstly, as our synthesis procedure has been performed in air, that band cannot be caused by oxygen vacancies. Besides, two samples of different concentrations appear in this study, M3_31 and M7_31, and as it can be observed the one with the higher concentration of zinc nitrate, M7_31, is the one that has formed the higher amount of zinc oxide and the one presenting a more intense band, as it could be expected.

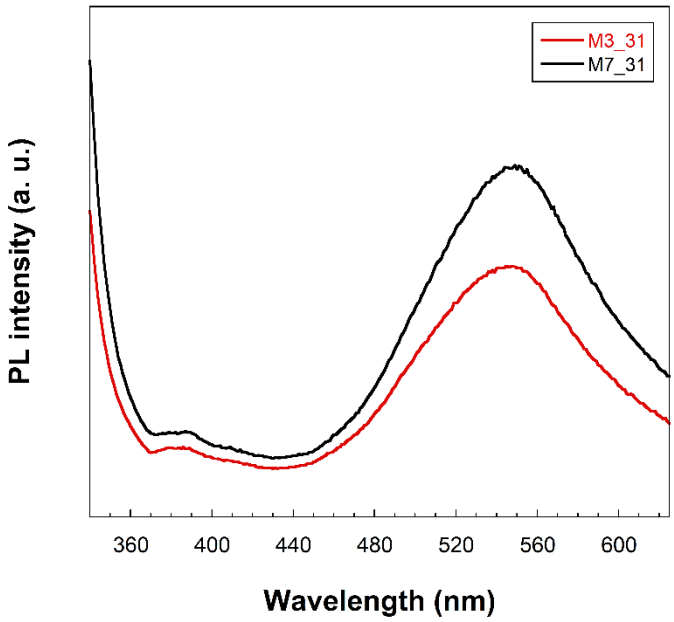

Figure 4.7. Photoluminescence spectra of two samples with different initial concentration of zinc nitrate.

Extensive research has been carried out to study the luminescence mechanism in ZnO nanostructures. The PL spectra observed in Figure 4.7 shows a clear broadband usually related with the defect emission due to trap states in ZnO. The origin of this defect related emission in the visible region is still a controversial question. In our case, the band is centred at 550 nm corresponding to the green region of the spectra and matched with an energy of 2.25 eV.

From this study of the dependence with the zinc concentration when using the direct precipitation synthesis method, it can be concluded that it is possible to achieve the coating with ZnO of the magnetoelastic strips when the amount of zinc nitrate 0.2 M is higher than 0.30 ml and mixed with 10 ml NaOH 0.1 M. If there is less amount of nitrate, a mixture of zinc hydroxide and zinc oxide will be obtained, while if that amount is higher the precipitate will only be zinc oxide. In this case, the morphology of the deposited particles is close to a sponge mainly due to the conditions of the reaction.

- Seeding procedure with zinc acetate particles

In this series of experiments, the cleaned Metglas 2826MB3 ribbon was directly seeded with a 0.1 M zinc acetate dihydrate solution in ethanol. For the seeding procedure, metglas strips were placed in a petri dish with the rough side up, and 2 ml of $(C_2H_3O_2)_2Zn \cdot 2H_2O$ were added. This was kept overnight at 80 ℃ to evaporate the solvent and to let the zinc acetate particles get attached to the surface of the metglas to act as nucleation points for the later precipitation reaction. After this, the samples, as in the previous experiments, were placed in a glass vial with the rough side up, held with an external magnet to add the precipitation solutions and manually shaken until total homogenisation. The added amounts of zinc nitrate were the same as for the previous experiment where only zinc oxide was obtained, and the precipitation conditions similar to the ones of the time dependence studies, being these synthesis conditions summarised in Table 4.5.

Table 4.5. ZnO preparation conditions for the samples seeded with zinc acetate after the precipitation step.

Samples	***Seeding conditions***	***Reactants***		***Precipitation conditions***
		V NaOH 0.1 M (ml)	***V $Zn(NO_3)_2$ 0.2 M (ml)***	
M1_58	*2ml of ethanoic zinc acetate solution + 1 day at 80 ℃*	10	0.30	*1 day at 65 ℃*
M2_58			0.35	
M3_58			0.40	
M4_58			0.45	
M5_58			0.50	
M6_58			0.55	

As it can be observed in Figure 4.8 XRD patterns showed that, in all the samples there is presence in the final product of acetate traces. It was expected that during the reaction time and due to the precipitation process, all the initially seeded zinc acetate would evolve to zinc oxide just before acting as nucleation points for the subsequent deposition

procedure. However, this has not been a successful procedure. Therefore, these samples are not useful for further experimental characterization.

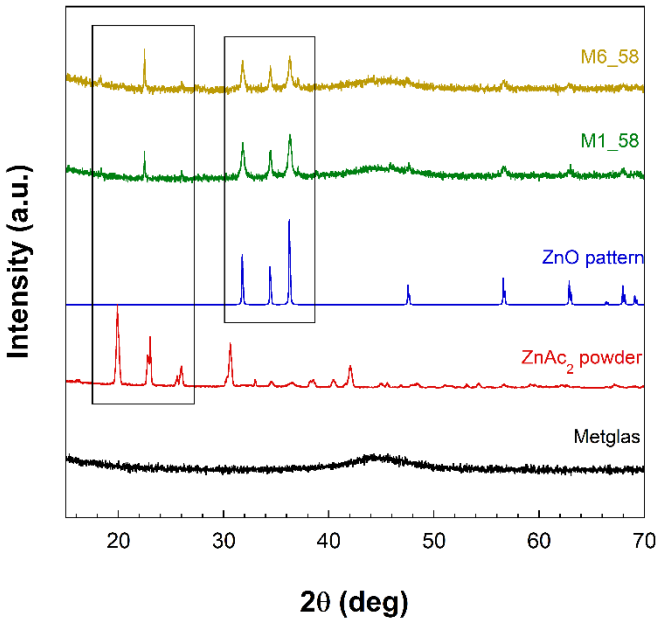

Figure 4.8. X-ray spectra of the samples prepared by seeding procedure with zinc acetate solution and later precipitation process.

- Seeding procedure with zinc oxide homemade nanoparticles

As in the previously described synthesis procedure, the samples will be seeded before the precipitation reaction with different zinc nitrate concentrations. However, as in the last experiments the zinc acetate of the seeding procedure did not evolve to zinc oxide during the precipitation, in the present case the seeding solution will be prepared directly with zinc oxide homemade nanoparticles.

The synthesis of ZnO nanoparticles was carried out by following a hydrothermal procedure: 0.4 g of lithium hydroxide monohydrate, $Li(OH)\cdot H_2O$ were suspended in 100 ml absolute ethanol under magnetic stirring. The suspension was added into 50 ml ethanoic 0.1 M solution of zinc acetate dihydrate, $Zn(CH_3COO)_2\cdot H_2O$ under constant stirring. The obtained solution was then sealed in an autoclave reactor and maintained at 100 ℃ for 3 h, followed by natural cooling down to room temperature.

The obtained particles were centrifuged at 4000 rpm for 10 minutes, washed after resuspension in water and centrifugation for three times and finally dried at 80 ℃. The XRD characterization of these homemade nanoparticles is shown in Figure 4.9. The measured diffraction pattern is compared to the standard JCPDS card for ZnO which corresponds to the wurtzite crystal No 36-1451 structure of ZnO. The observed experimental peaks fit well to the standard card values corresponding to ZnO reflections arising from (100), (002), (101), (102), (110) and (103) planes.

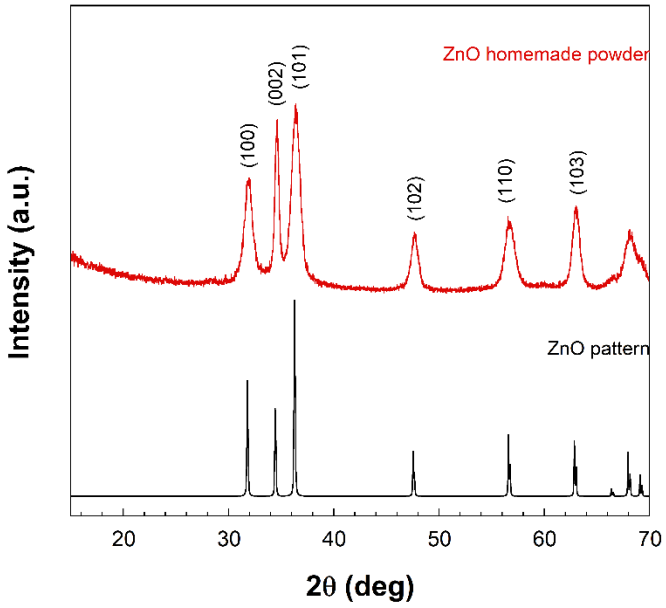

Figure 4.9. X-ray spectra of the homemade zinc oxide nanoparticles and the zinc oxide standard card.

For the deposition procedures, the metglas strips were put in a petri dish with the rough side up, and 2 ml of the seeding solution, ethanoic zinc oxide nanoparticle solution, were added. This solution was prepared by dispersing 100 mg of ZnO homemade nanoparticles in 50 ml ethanol under magnetic stirring and sonication. For the solvent evaporation process, those seeded strips were left in an oven at 80 ℃ overnight.

Following, the seeded strips were placed in a glass vial again with the rough side up, held with an external magnet to add the precipitation solutions and manually shaken until total homogenisation of the initially

formed turbidity when both solutions were added. The added amounts of zinc nitrate covered in this particular case the whole range previously studied in the zinc nitrate concentration dependence to observe if in this new procedure there is formation of zinc hydroxide after the seeding with zinc oxide. In fact, two different series of samples were prepared to cover the previously studied zinc nitrate quantities. After the solutions homogenisation, the vials were left for the precipitation process to take place into an oven for 1 day at 65 ℃. This precipitation time was chosen to ensure the total evolution of the formed precipitate to zinc oxide, avoiding as much as possible the zinc hydroxide formation. In Table 4.6 sample preparation conditions are summarised.

Table 4.6. Sample preparation conditions for the samples seeded with zinc oxide solution after precipitation step.

Samples	***Seeding conditions***	***Reactants***		***Precipitation conditions***
		$V\ NaOH$ $0.1\ M\ (ml)$	$V\ Zn(NO_3)_2$ $0.2\ M\ (ml)$	
$M1\_60$	$2ml\ of\ ethanoic\ zinc\ oxide\ solution + 1\ day\ at\ 80\ ℃$	10	0.30	$1\ day\ to\ evaporate\ seeding\ solution\ solvent + 1\ day\ at\ 65\ ℃$
$M2\_60$			0.35	
$M3\_60$			0.40	
$M4\_60$			0.45	
$M5\_60$			0.50	
$M6\_60$			0.55	
$M1\_63$			0.05	
$M2\_63$			0.10	
$M3\_63$			0.15	
$M4\_63$			0.20	
$M5\_63$			0.25	
$M6\_63$			0.30	

In Figure 4.10, a picture of the vials, M1_63 to M6_63, after the precipitation process is shown. As previously mentioned, a white precipitation powder deposits all over the bottom of the vial covering the

magnetoelastic ribbon. Due to the increasing concentration, in the first vial the precipitate is barely visible, while from 4 to 6 the metglas strip is totally covered with the synthesized zinc oxide particles.

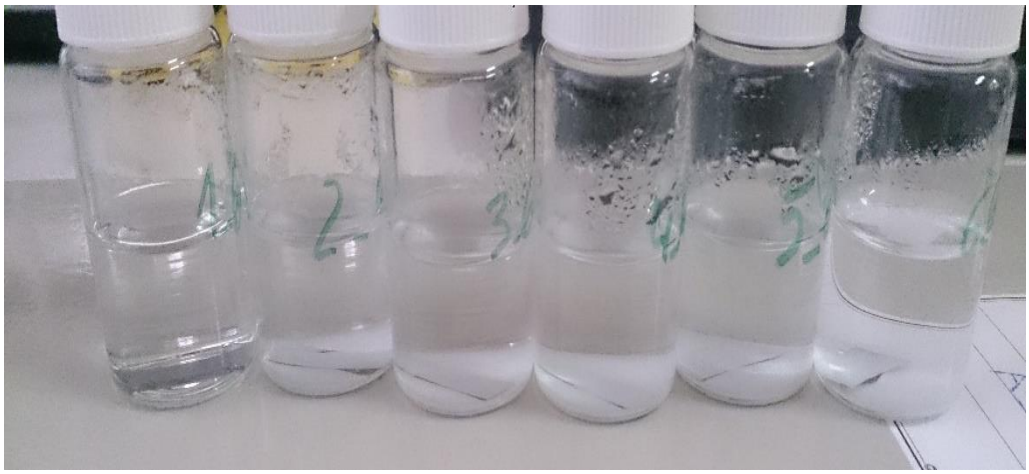

Figure 4.10. Precipitate formation and deposition that takes place after de reaction process for increasing concentration of zinc reactant in samples 1_63 to 6_63.

In Figure 4.11 XRD patterns of the prepared samples are shown. As it can be observed, in all the samples the deposited layer is formed by zinc oxide without any presence of other compounds as zinc hydroxide. This means that the precipitation process has had enough time to completely evolve to zinc oxide. The morphology of this deposited precipitate onto the metglas ribbon was studied by SEM. The obtained SEM pictures can be seen in Figure 4.12. showing the same flower structure as when the time dependence experiments were performed. The structure of the formed precipitate depends on the reaction conditions (temperature and time). During these last synthesis experiments, the samples were directly put into the oven to allow the precipitation take place, as it was made for the experiments about the time dependence. In Table 4.7 the results obtained from XRD and SEM are summarised.

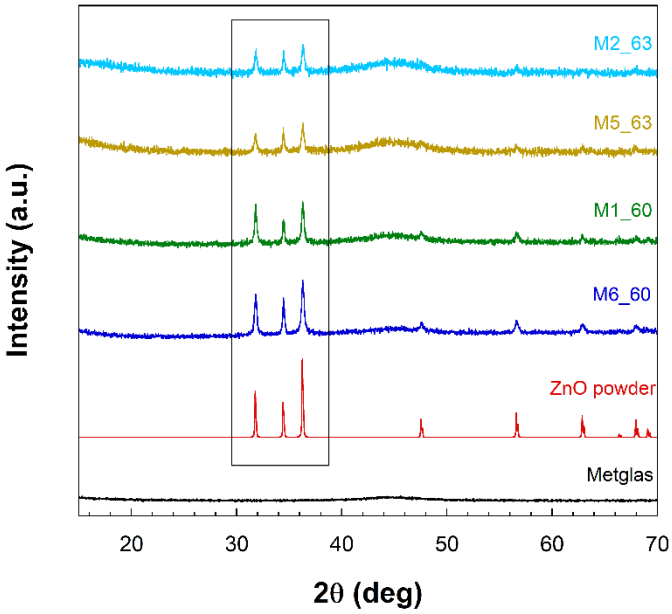

Figure 4.11. X-ray spectra of the samples prepared by seeding procedure with zinc oxide solution and later precipitation process.

M2_63

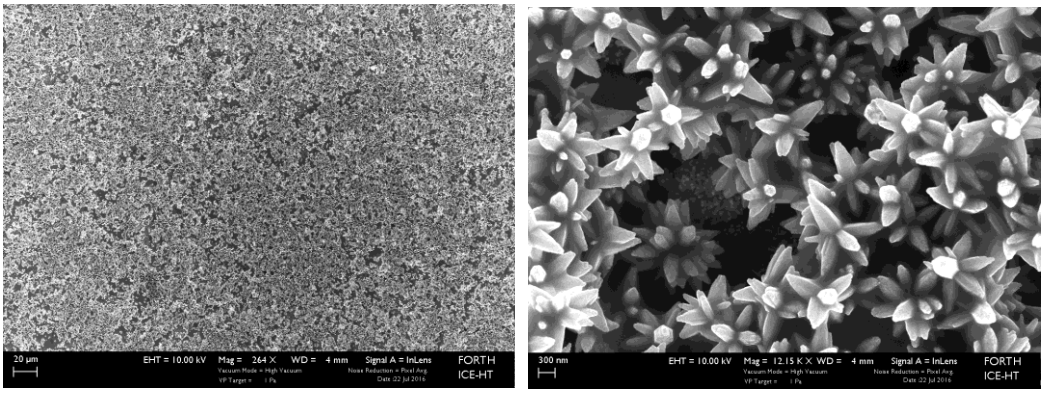

Figure 4.12. SEM images of M2_63 sample. ZnO deposited layer with flower structure.

Table 4.7. XRD and SEM characterization results (final product and morphology) for the precipitation layers formed at different zinc concentrations.

Samples	$V\ Zn(NO_3)_2$ $0.2\ M\ (ml)$	*XRD*	*SEM*
M1_60	0.30	*ZnO*	–
M2_60	0.35	–	*Flower*
M3_60	0.40	–	–
M4_60	0.45	*ZnO*	–
M5_60	0.50	–	*Flower*
M6_60	0.55	*ZnO*	–
M1_63	0.05	–	–
M2_63	0.10	*ZnO*	*Flower*
M3_63	0.15	–	–
M4_63	0.20	–	*Flower*
M5_63	0.25	*ZnO*	–
M6_63	0.30	–	–

As a part of the characterization of the formed precipitate and deposited layers, photoluminescence measurements were also carried out. The green luminescence broadband with a maximum at 545 nm can be observed in Figure 4.13. As in the previous PL spectra (see Figure 4.6), the intensity of the band is related with the quantity of ZnO formed onto the surface of the metglas strip. As it can be clearly observed, as the concentration increases the intensity follows the same tendency. For the samples with a low amount of deposited ZnO, M1_63 and M2_63 only a weak band can be observed. On the contrary, for higher ZnO containing samples, M3_63 and M4_63 this band becomes broader, as it could be expected.

As it was previously shown in Figure 4.7, the PL spectra shown in Figure 4.13 shows a clear broadband in the visible region. The band is centred at 545 nm corresponding to the green region of the spectra and matching with an energy of 2.27 eV.

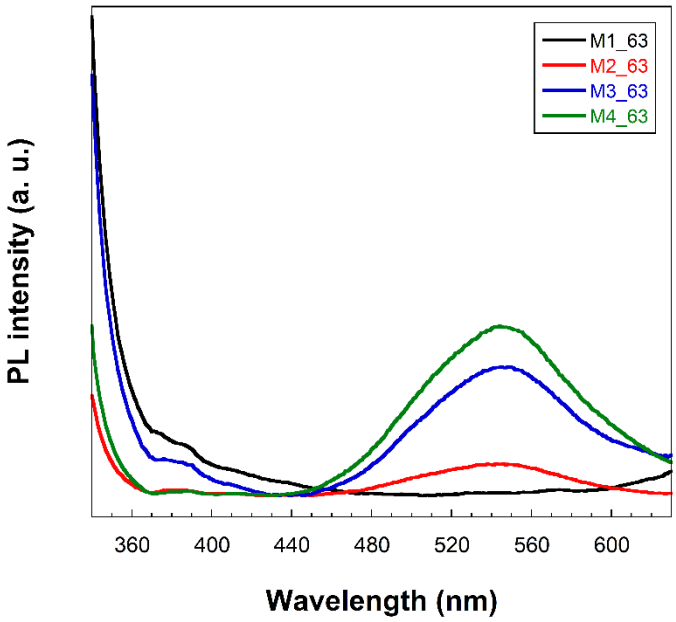

Figure 4.13. Photoluminescence spectra samples with different initial concentration of zinc nitrate for the precipitation process after the seeding.

As conclusions of these seeding and further precipitation experiments, it can be concluded that in order to ensure the deposition and formation of a ZnO layer onto the magnetoelastic material the seeding procedure must be performed with ZnO particles and not with other kind of precursor as zinc acetate is. It has to be concluded that those $ZnAc_2$ particles do not evolve to zinc oxide during the reaction processes and induce impurities in the deposited layer. For the optimal deposition of ZnO layer following this type of procedure, ZnO particles must be used as seeds. Nevertheless, although the Metglas 2826MB3 strip surface was covered with the ZnO fabricated and deposited layer, this was not homogeneously distributed along the whole surface of the strip.

- Casting procedure with zinc oxide nanoparticle solution

To follow this method, the metglas samples were covered directly with the homemade zinc oxide nanoparticles. The cleaned strips were placed in a petri dish with the rough side up and 2 ml of a zinc oxide nanoparticle solution were added. This solution was prepared by

dispersing 100 mg of ZnO homemade nanoparticles in 50 ml ethanol under magnetic stirring and sonication. After the addition of the solution, the samples were left into an oven at 85 ℃ until all the solvent has completely evaporated.

By using the synthesis procedure, all the obtained and deposited final product was zinc oxide, as it can be observed in the difractograms presented in Figure 4.14. As the deposited amount of ZnO is low, the formed layer is too thin. This can be observed in the signal obtained in XRD difractograms where there is a prevalence of the metglas signal. The amplitude of the broad band coming from the amorphous metglas makes the whole difractogram to be noisy. Nevertheless, the most intense peaks from the ZnO nanoparticles can be observed for the deposited samples M1_67 and M4_67.

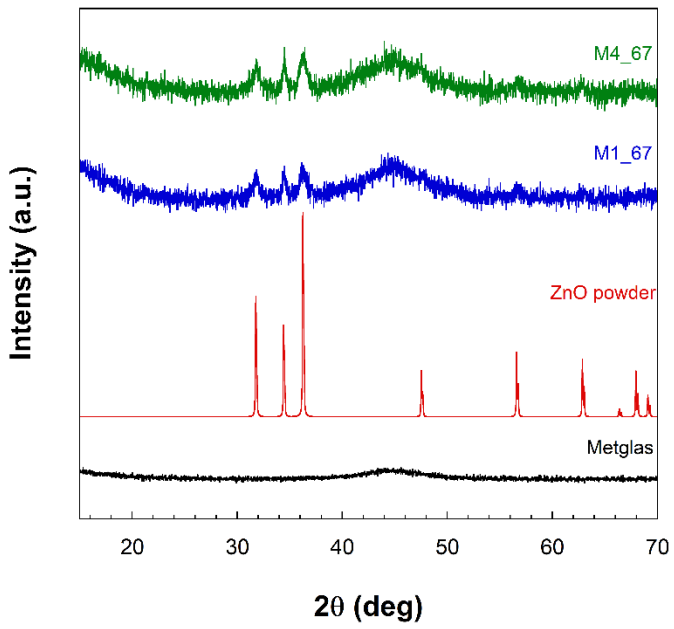

Figure 4.14. X-ray spectra of the samples prepared by seeding procedure with zinc oxide solution and later precipitation process.

SEM micrographs shown in Figure 4.15 show that the ZnO particles were found as aggregated composed of individual nanoparticles of spherical shape. The size of the nanoparticles was measured using the ImageJ software (National Institutes of Health, Bethesda, USA). The size

ranged from 11 to 32 nm with a mean value of 18.3 ± 4.0 nm. On the other hand, the deposited ZnO layer covered entirely the surface of the metallic ribbon as can be also observed in Figure 4.15.

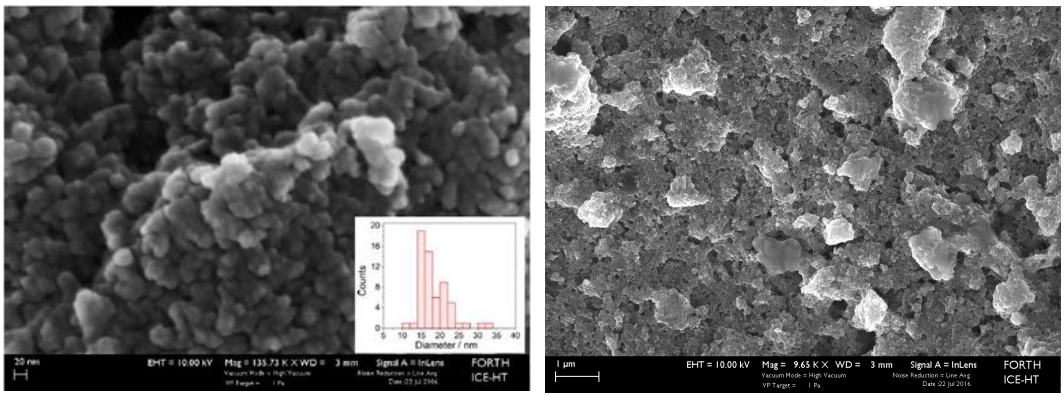

Figure 4.15. SEM images of the formed layer after 6 deposition processes.

From these previous measurements, it can be inferred that the deposited layers were homogenous and only of ZnO, and also very thin. In order to get new information about the thickness of the obtained ZnO layer onto the Metglas 2826MB strip, the magnetoelastic resonance of the whole system will be used. Several subsequent deposition processes will be made and after each of them, the samples (ZnO layer + Metglas 2826MB) will be weighted and hereafter their magnetoelastic resonance frequency will measured. By following the evolution of the change in the resonant frequency against the loading mass amount of ZnO, not only an estimation of the deposited layer thickness per deposition process, but also a close measurement of the deposited ZnO layer Young's modulus can be done, as it will be better explained in a next section.

Figure 4.16 shows photoluminescence spectra of the ZnO layer. A small peak appear at 380 nm, which can be attributed to the near band edge emission, arising from the recombination of free excitons. However the spectrum is dominated by a broad band with a maximum around λmax = 545 nm (2.27 eV) which is known as green emission and has a full width at half maximum of $\Delta E1/2$ = 330 meV.

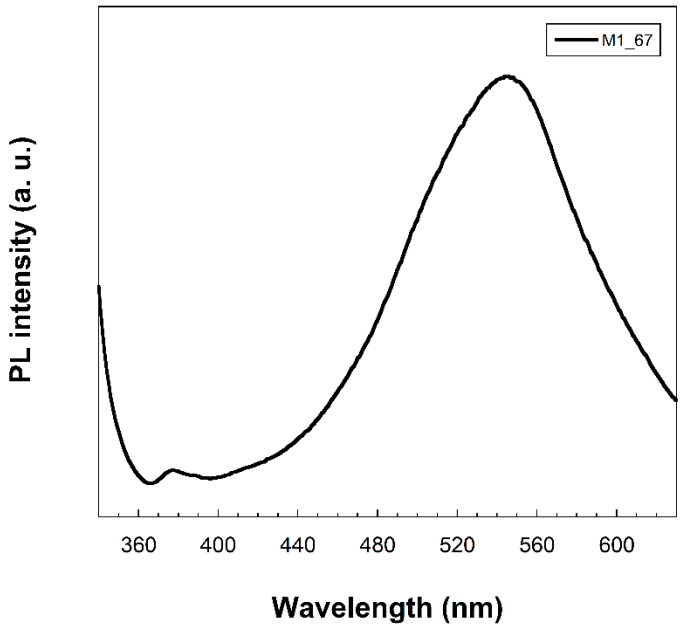

Figure 4.16. Photoluminescence spectra of one of the prepared samples by casting a zinc oxide nanoparticle solution.

From all the previous considerations it is clear that at this point it can be concluded that the best synthesis procedure to obtain a pure ZnO final product and also a good and homogenous film is the casting procedure by directly depositing a solution formed with synthesised ZnO nanoparticles onto a Metglas 2826MB3 strip.

Therefore, for the next experimental characterization (determination of the elastic modulus of the deposited ZnO thin film) and sensing tests as biosensing platforms (study of the oxidation of the hemoglobin in presence of hydrogen peroxide), only the samples fabricated by using this last method are going to be used.

4.2.2. Determination of the elastic modulus of the deposited ZnO thin films

The knowledge of the elastic parameters of a thin film turns to be of great importance in the design and fabrication of sensing devices. While the usual technique to measure the Young modulus of a bulk materials is uniaxial tensile testing, this turns out to be impossible to apply when dealing at the nanoscale, where the manipulation of the material and application of the force and accurate measurement of displacement is extremely difficult. Thus, the possibility to perform in situ experiments at the nanoscale becomes a necessary tool in order to obtain not only quantitative but also qualitative information about nanosized materials[24].

Therefore, the detection of the magnetoelastic resonance frequency of our fabricated devices becomes a precise tool to determine not only the Young's modulus value of the deposited ZnO film, but also to give information about the Young's modulus of the bare magnetoelastic strip and discuss the goodness of the deposition process of the ZnO film onto it.

Once the magnetoelastic ribbons were cleaned and dried, they were weighted and the resonant frequency was measured with a homemade coil system that can be seen in Figure 4.17. For those magnetoelastic resonance measurements, a magnetoelastic sensor "reader box" made by driving a homemade coil (N = 24 turns, R = 0.6 W, L = 6.9 μH), wrapped around a cylindrical glass vial of 4.6 cm height and 2.3 cm diameter.

The magnetoelastic resonance method employed to make all these measurements is different than the one previously explained for the polymer deposition experiments. As the system to perform the magnetoelastic resonance measurements is also different, in this case there is only one coil, which is the responsible for driving all the processes.

In this particular case, in order to take the measurements, the experimental set-up at the Department of Material Science in the University of Patras was used. A picture of the magnetoelastic sensor

"reader box" and the homemade coil used are shown in Figure 4.17[25, 26]. An extensive explanation has already been given in section *2.1.2.3. Magnetoelastic resonance and ΔE effect*.

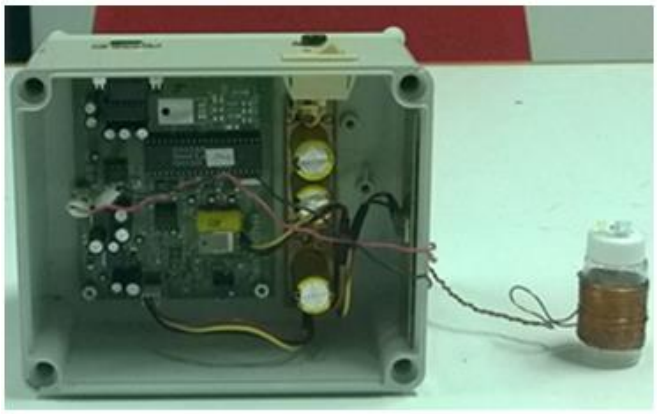

Figure 4.17. Homemade coil and magnetoelastic resonance measurement box.

The fundamental resonance frequency of a single flat layer, stress free ribbon of length L, density ρ, and elastic Young modulus E is given by the well-known relationship[27,28]:

$$f_r = \frac{1}{2L}\sqrt{\frac{E}{\rho}} \qquad [4.2]$$

but when, as it is our case, we have more than one layer at resonance, that formula has to be modified to:

$$f_r'' = \frac{1}{2L}\sqrt{\frac{E''}{\rho''}} = \frac{1}{2L}\sqrt{\frac{E+E'\frac{h'}{h}}{\rho+\rho'\frac{h'}{h}}} \qquad [4.3]$$

where $E'' = E + E'\left(\frac{h'}{h}\right)$ and $\rho'' = \rho + \rho'(h'/h)$, are referred to the whole sensing element which is the ZnO coated metglas strip. The unprimed parameters refer to the metglas 2826MB strip alone and the primed parameters refer to the ZnO layer.

Figure 4.18. Schematic representation of the Metglas 2826MB3 and ZnO layers layout in our resonant devices.

According to the method, if a series of similar films with different thicknesses h' can be synthesised, then a plot of the E'' parameter of the bilayer system (extracted numerically from the resonance frequency) versus h' will be a straight line with a slope equal to the value of the Young's modulus E' of the film. Additionally, the Young's modulus E of the substrate layer can be extracted from the y-intercept. In our case, a thickness of $h \approx 30\,\mu m$ was measured for the metglas 2826MB3 layer ($\rho = 7900\,kg/m^3$), while the thickness h' of the ZnO layer was estimated assuming a uniform film, given its mass, dimensions and the (bulk) density value of ZnO $\rho' = 5606\,kg/m^3$. As I have previously explained, bearing the purpose of the determination of the Young modulus in mind, six different and successive depositions of the ZnO solution were performed onto the metglas strips, with the final one resulting to the thickest ZnO solid film of about 1 μm thickness.

Figure 4.19 shows the obtained results and the corresponding linear fit for one of our resonant platforms. The good linearity reveals the validity of the aforementioned method. From the y-intercept, a Young's modulus of 160 GPa is estimated for the bare Metglas strip, in good agreement with previous results[29]. From the slope, a Young's modulus value of 60 GPa is calculated for the ZnO film.

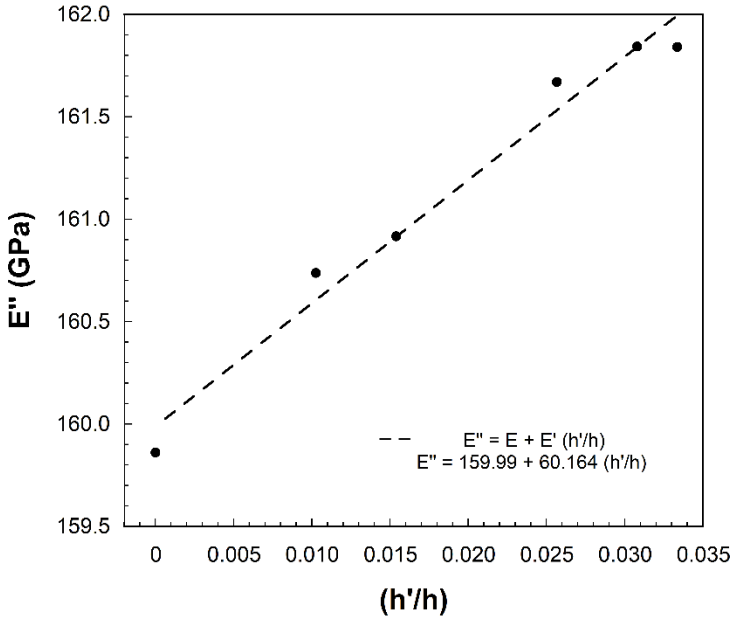

Figure 4.19. Total Young's modulus (E'') measured as a function of the ratio h'/h (width of the deposited ZnO layer / width of Metglas 2826MB strip).

The Young's modulus of bulk ZnO is $\approx 140\,GPa$, a value that is generally accepted and was calculated by Kobiakov[30] starting from elastic constants for ZnO crystal. The range of experimental values measured when dealing with ZnO at the nanoscale, is quite diverse depending not only on the geometry of the material but also on the experimental process used for its measurement Thus, for ZnO nanowires Song et al.[31] gave a value of $29\,GPa$ determined by AFM bending measurements and Desai et al.[32] obtained a value of $21\,GPa$ measured by using a MEMS test-bed to perform uniaxial tensile experiments. On the other hand, Ji et al.[33] have reported values of Young's modulus as high as $117\,GPa$ and $232\,GPa$ for ZnO nanowires with diameters of 100 nm and 30 nm respectively, by studying the buckling of the nanowires with nano-indentation. For ZnO nanobelts, Bai et al.[34] gave a Young's modulus value of $50\,GPa$, and Wang obtained a value of $52\,GPa$[35], in both cases by measuring the dynamic response of the specimen in an alternating electrostatic field inside a TEM. Considering all the previously reported values, our observations mostly agree with those obtained for nanobelt shaped samples, and we can infer that our $\sim 1\,\mu m$ thickness ZnO film on the Metglas 2826MB3 strip, behaves like a wide nanobelt with Young's modulus of about $60\,GPa$.

4.2.3. Hydrogen peroxide detection

Over the last 30 years there has been a great effort to develop new hydrogen peroxide, electrochemical biosensors in order to understand the redox processes of enzymes and proteins and if these are maintained after their immobilization on electrodes surface. Hydrogen peroxide is a chemical compound with the formula H_2O_2, that has found a wide range of applications. It is employed in the industry for pulp and paper bleaching and for certain waste-water treatments; it is also used in medicine as disinfectant, with cosmetically purposes as human hair bleaching or to treat acne, chemically used as an oxidizer or to fabricate some explosives among others. Hydrogen peroxide is also found in biological systems including the human body and plays a role in the immune system. H_2O_2 presents cytotoxic effects and associated tissue injury, and even more it plays a role in physiological and biomedical studies as well as when monitoring biological processes. H_2O_2 is also a side product of many oxidative biological reactions catalysed by enzymes such as glucose oxidase (GOx), lactate oxidase (LOx), cholesterol oxidase (ChoOx) and many others. The protein structure and redox transformation of protein molecules are actually a preferential task devoted to give a deep insight into physiological electron transfer processes. Therefore, it is of high importance to be able to achieve sensitive determination of H_2O_2 presence in many biological processes and related applications. Additionally, it is also well known that due to its intrinsic peroxidase activity, hemoglobin is an excellent protein to fabricate H_2O_2 electrochemical biosensors[36,37].

Hemoglobin (Hb) is the iron-containing oxygen transport metalloprotein present in the red blood cells. This physiologically oxygen transfer protein with formula $C_{2952}H_{4664}O_{832}N_{812}S_8Fe_4$, has a well known and documented structure, and properties as low cost, relatively higher stability and intrinsic peroxidase activity[38]. Hb has a quaternary structure made up of four protein molecules (globulin chains) that are connected together. Those polypeptide chains have one electroactive iron heme group[39] each, as it can be seen in Figure 4.20. A heme group consists of an iron ion held in a heterocyclic ring that consists of four pyrrole

molecules cyclically linked together with the iron ion bound in the centre. The structure of a heme group can be observed in Figure 4.21.

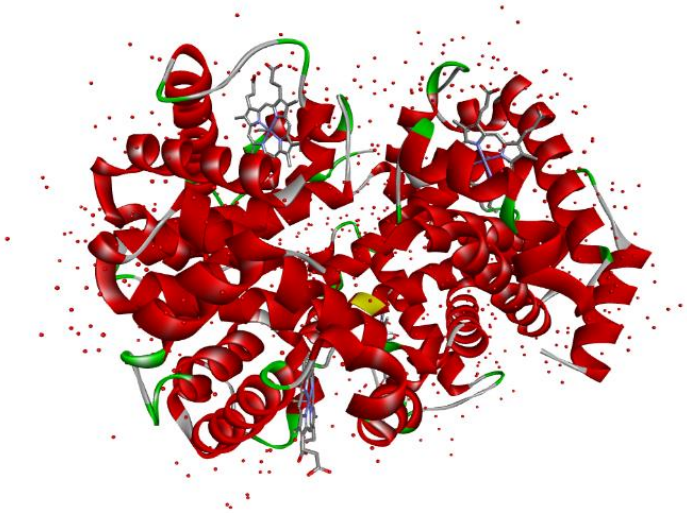

Figure 4.20. Ribbon diagram of hemoglobin showing the position of the four hemes (blue) taken from the RCSB Protein Data Bank and plotted on BIOvia Discovery Studio Visualizer.

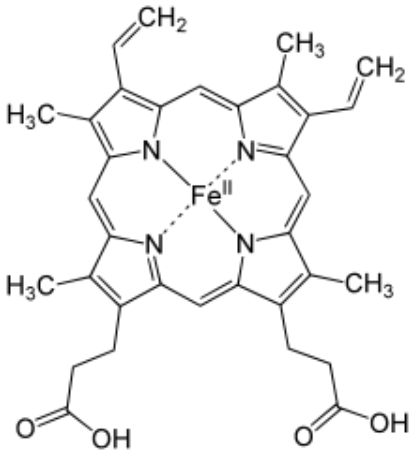

Figure 4.21. Chemical structure of a heme group with the iron ion in the centre surrounded by a four pyrrole linked structure.

Hemoglobine is a prototype molecule for studying biological electron transfer processes and therefore it has been extensively used as an ideal model enzyme to study biological electron transfer reactions, to evaluate materials for their choice to be used as substrates for the immobilisation of biomolecules in an active configuration. It has already

been used in the past for the fabrication of electrochemical biosensors and bioreactors[40, 41].

Nevertheless, many of the fabricated sensors exhibit slow electron exchange due to the unfavourable orientation of hemoglobine molecules onto electrode surfaces, and so, efforts point towards the development of new immobilisation methods and supporting materials to promote the direct electron transfer of Hb while maintaining its enzymatic activity. Among other possibilities, ZnO nanoparticles are good candidates for such purposes[42].

Hemoglobin is an auto-oxidating protein where heme iron atoms easily oxidise from ferrous Fe (II) to ferric Fe (III) and reduce from Fe (III) to Fe (II). The reaction scheme for the electrochemical reduction and oxidation of Hb can be written as follows:

$$HbFe\ (III) + H^+ + e^- \leftrightarrows HbHFe\ (II)$$

An excellent and complete graphical representation of all involved reactions in this reduction and oxidation of Hb process can be found in literature[38]. It is well known that the Hb molecule can catalyse the reduction of H_2O_2[43,44,45] and accordingly Hb has been extensively used to construct H_2O_2 biosensors[46]. As shown in Figure 4.22, the enzymatic reaction mechanism can be described as follows[47,48]:

$$2\ HbHFe\ (II) + H_2O_2 + 2H^+ \rightarrow 2\ HbFe\ (III) + 2H_2O$$

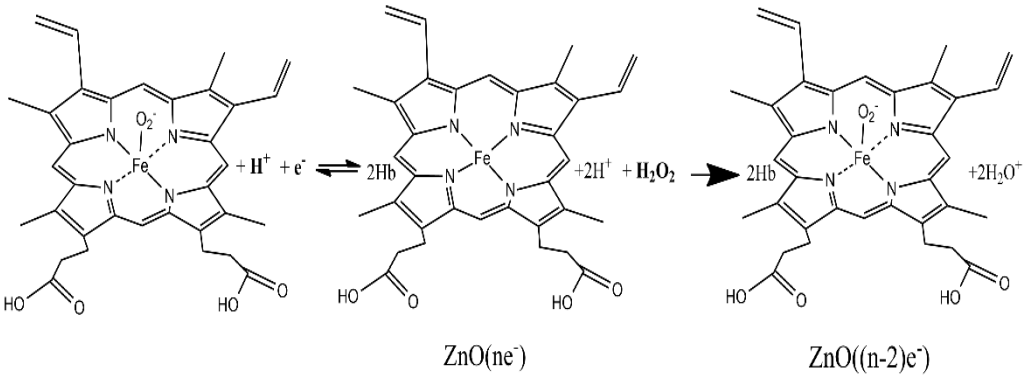

Figure 4.22. Reaction scheme for the direct reduction and oxidation of the immobilised hemes of Hb and the electrocatalytic reduction of H_2O_2 on the sensor (created on Chemdraw).

With this purpose in mind, we have fabricated a biosensor to detect the oxidation of hemoglobine by H_2O_2. The biosensor is composed of a thin-film of nanostructured ZnO deposited onto a magnetoelastic strip of commercial magnetoelastic material Metglas 2826MB. The ZnO nanoparticles for the ZnO layer were prepared using the hydrothermal method and a layer of Hb was successfully immobilised on the ZnO layer. The resultant three-layer sensor was used in two simultaneous detection techniques, as a working electrode (Metglas/ZnO/Hb) in cyclic voltammetry (CV) and as the resonant platform in magnetoelastic resonance measurements (MR). A detailed scheme of the detection home made system is shown in Figure 4.23.

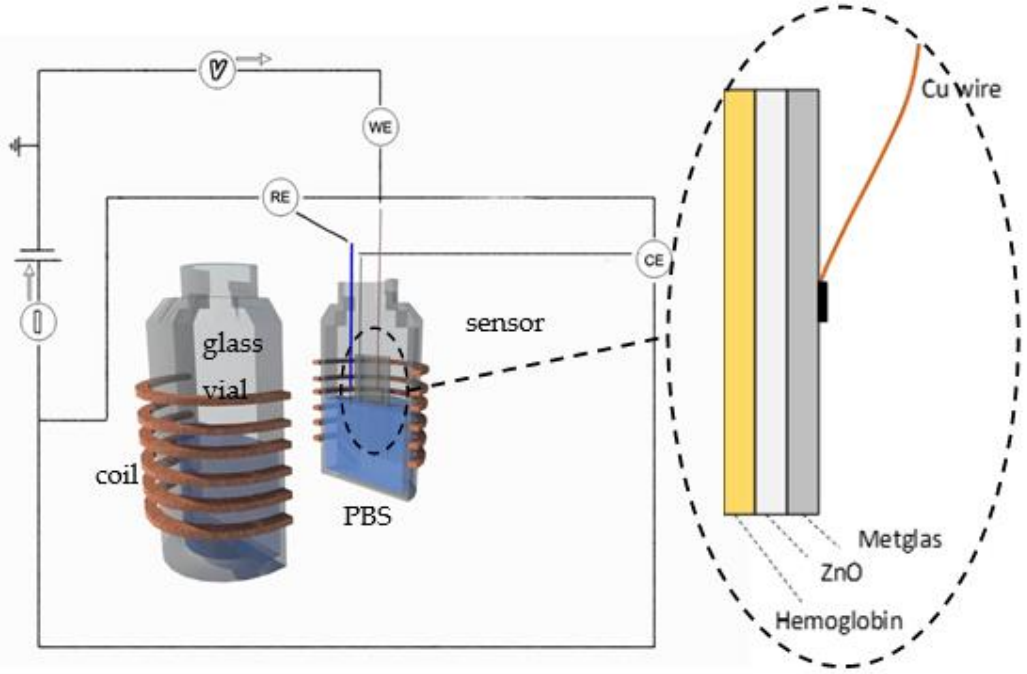

Figure 4.23. The experimental set-up consisted of three electrodes immersed in a PBS buffer solution inside a glass vial on which a coil was wrapped externally.

On one hand, the experimental cyclic voltammetry (CV) technique was used to monitor the electrochemical behaviour of the modified electrodes. The detection experiment consisted of a standard electrochemical cell composed of three electrodes, the sensor as the working electrode (WE), the platinum counter electrode (CE) and the Ag/AgCl reference electrode (RE). The system was immersed in a PBS

buffer solution at room temperature where drops of H_2O_2 were added. The measurement technique applied a voltage V between the reference and working electrodes during the CV scans and the resulting current (I) between the working and the counter electrodes was recorded. On the other hand, magnetoelastic materials working in resonant conditions are known to be extremely sensitive to external parameters, such as mass load[49]. An external coil was wrapped around the glass vial, which contained the electrolyte solution and the cell. The MR system is the same described above. The appearance of any mass load onto a magnetoelastic ribbon will immediately cause a decrease in its resonant frequency and this decrease can be used to determine the loaded mass value by comparing to calibration curves of known mass loads.

The electrochemical measurements were performed on an Autolab PGStat 101 Potentiostat with a conventional three-electrode system; the Metglas/ZnO/Hb acted as working electrode, a platinum wire as counter electrode, and Ag/AgCl microelectrode as reference electrode. Simultaneously, magnetoelastic resonance detection was performed by using a magnetoelastic resonator made by Sentec and our homemade coil described above.

4.2.3.1. Fabrication of the electrode

The Metglas/ZnO/Hb electrode was fabricated following the procedure described above for the Metglas/ZnO film, plus the immobilisation of Hb on its surface. Hemoglobin (MW 65,000), from Bovine blood was purchased from Sigma and was used without further purification. For the Hb immobilization, a 20 μM Hb solution was prepared using 0.01 M Phosphate Buffer Solution (PBS), pH 7 and stored at 4 ℃. Hb was deposited on the surface of the Metglas/ZnO by dropping 5 μl of Hb solution on the surface material and allowing it to dry at 30 ℃ for 30 minutes. This procedure was repeated twice to ensure the immobilization of the hemoglobin and a homogenous distribution of the deposited amount. Sodium dihydrogen orthophosphate (0.01M) from Sigma was used to prepare the supporting electrolyte solution, and its pH

was adjusted to 7 using NaOH and was thoroughly deaerated by bubbling with argon prior to the experiments. All solutions were prepared with deionized water. Prior to all electrochemical measurements, the Metglas/ZnO/Hb electrode was rinsed with PBS to remove any non-immobilised Hb from its surface.

For the sensing experiments H_2O_2 (30% w/v solution) purchased from Lach-Ner was used. Successive additions of aliquots of 5 μL of H_2O_2 30 μM were made in order to increase the H_2O_2 concentration by 25 μM at each step. Each amount was added at time intervals of 15 minutes and CV scans and MR were obtained right afterwards (30 seconds) and shortly before the end of the interval (5 minutes).

A real picture of the whole vial cap, with the three electrodes in it can be observed in Figure 4.24. Holes were made in the cap to ensure a good fixing of the electrodes and which is even more important to avoid any contact among them. The connexions with the sensor material, which is the working electrode, were made by attaching a cooper wire with carbon tape to the middle of the ribbon. In that way it can be ensured that there are no contributions of the wire to the vibration of the sample, as the middle part of the sample is a 'vibration free point'. A picture of the back part of the ribbon where the connection was made, can be observed also in Figure 4.24.

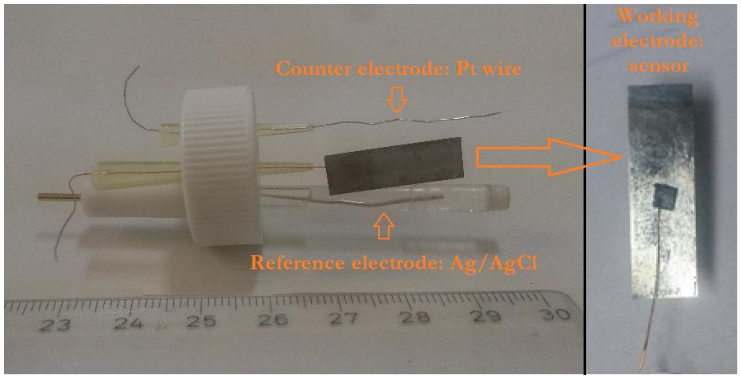

Figure 4.24. The experimental set-up consisted of three electrodes immersed in a PBS buffer solution inside a glass vial on which a coil was wrapped externally.

The final measure system with all the connections for the electrodes to make the voltammetry curves and inside the vial with the coil wrapped

on it for the magnetoelastic measurements is shown in Figure 4.25. This is the real system shown schematically in Figure 4.23, which has been developed specially for making these essays. It is a totally homemade system that uses a glass vial as a cell, making holes on the cap to properly fix the different electrodes.

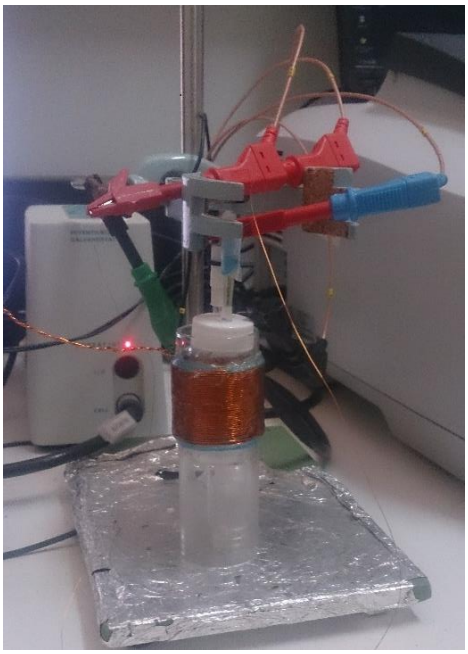

Figure 4.25. Final measurement set-up with the electrode connexions for the CV measurements and the external coil for the MR measurements.

4.2.3.2. Electrochemical behaviour of the electrode

When using CV, the potential between the reference and working electrodes was scanned from a certain initial voltage to a certain final potential to charge the capacitor and again scanned back in the reverse direction in order to discharge it. This allows the tracking of the electrochemical properties of the modified electrodes. The resulting current between the working and counter electrodes was plotted against the applied potential with respect to the reference electrode. The CV curve of an electric double layer capacitor (such as Metglas/ZnO) would be of a rectangular shape, in absence of a faradic reaction. In the presence of faradic redox reactions, the CV curve should exhibit peak

currents, which are due to the effect of pseudo-capacitance exhibited by the electrode material.

All voltammetry experiments showed in this part were carried out in a hemoglobin-free, 10 mM aqueous PBS electrolyte solution of pH 7 at room temperature. Figure 4.26 shows the CV curves of Metglas 2826MB (black), Metglas/ZnO (red) and Metglas/ZnO/Hb (blue) electrodes at a scan rate of 0.1 V/s.

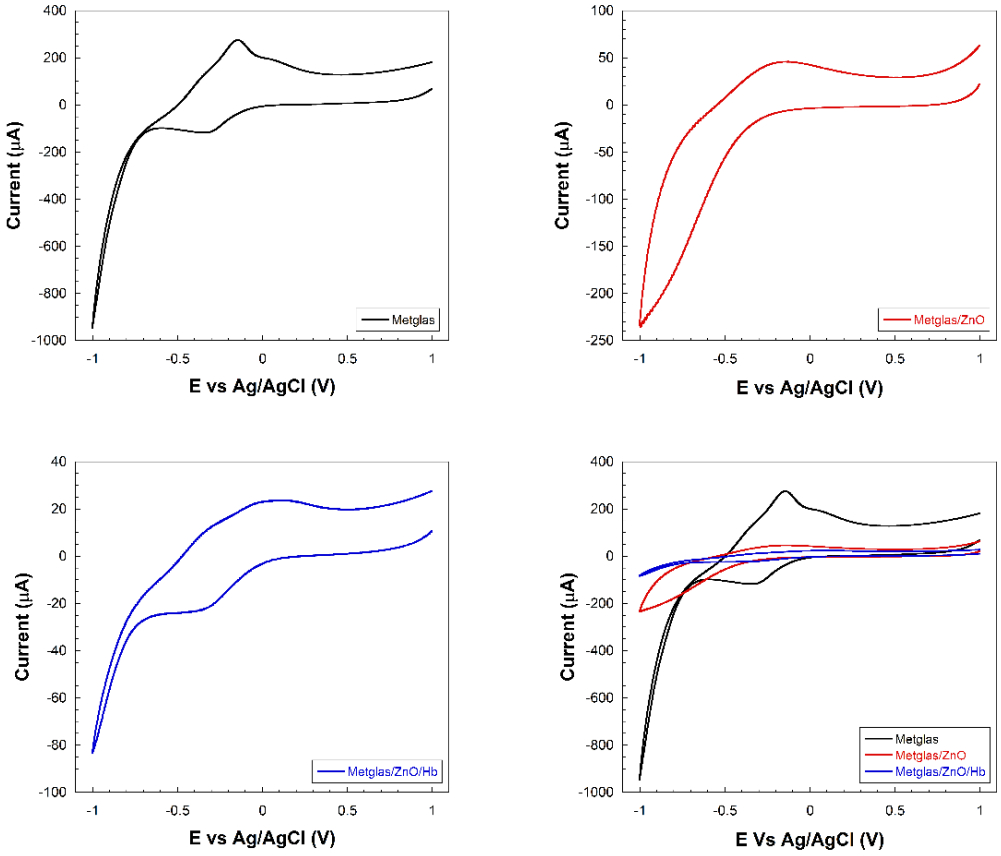

Figure 4.26. Cyclic voltammetry curve of Metglas 2826MB (black), Metglas/ZnO (red), Metglas/ZnO/Hb (blue) electrodes at a scan rate of 0.1 V/s, and as comparison the three in the same graph.

The metglas monolayer is exhibiting high peak redox currents, which are shown in the CV (Figure 4.26a). This metglas is exhibiting a very interesting electrochemical behaviour, and it seems likely to be a diffusion-controlled system with charge transfer phenomena in play. The metglas ribbon shows a characteristic reduction peak at -0.35 V and a (re)oxidation peak at -0.15 V in aqueous electrolyte solution. The voltage range is taken from -1 V to +1 V because in this range the metglas electrode is effectively working without any breakdown. These peaks that correspond to a reversible process could be possibly due to the high content of iron in metglas. As metglas is an amorphous iron rich metallic alloy, the iron atoms can occur in both oxidizing states Fe(II) and Fe(III), depending on their local neighbourhood in the amorphous atomic framework. Thus, depending on the applied potential, iron can be oxidized and reduced easily. These peaks could be a sum of contribution of various oxidation processes of iron to form divalent or trivalent species[50]. In addition, the metallic metglas gives back a greater and broader current when compared to the semiconducting Metglas/ZnO, due to its conducting nature.

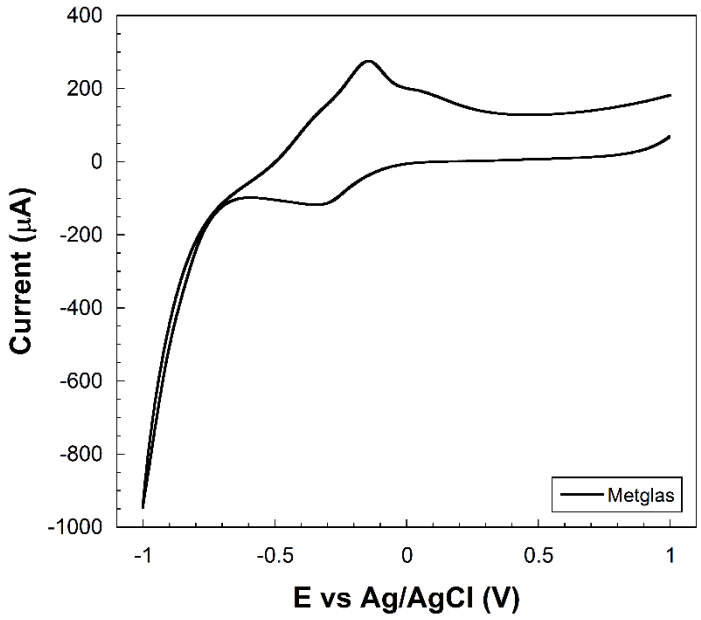

Figure 4.26a. Cyclic voltammetry curve of Metglas 2826MB electrode at a scan rate of 0.1 V/s.

The Metglas/ZnO system, where a zinc oxide layer has been deposited onto the metglas, (Figure 4.26b) shows the characteristic charging/discharging currents assigned to electron injection into sub-band gap/conduction band states of the ZnO film. The charging of the ZnO film as seen in Figure 4.26b starts at -0.16 V, which is around the same value reported at previous studies in literature[51]. Over the potential range examined, for potentials more positive to -0.16 V, the ZnO is insulating and serves only as a support for the immobilization of biomolecules.

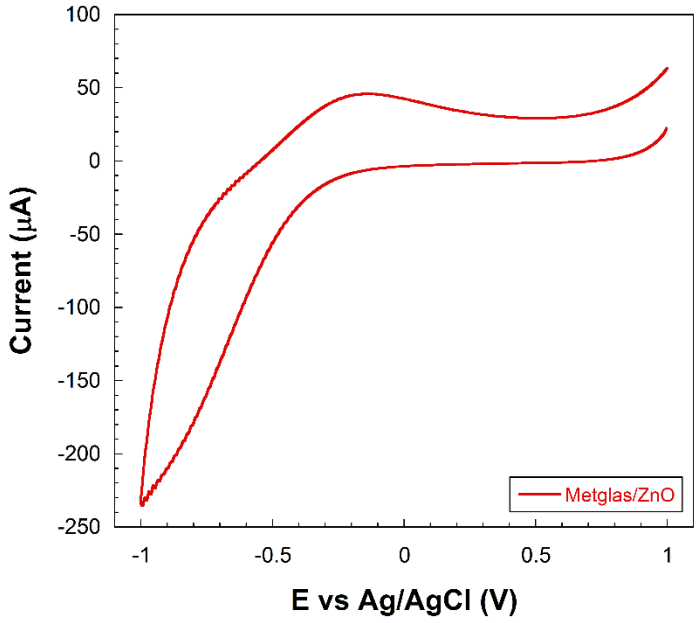

Figure 4.26b. Cyclic voltammetry curve of Metglas/ZnO electrode at a scan rate of 0.1 V/s.

The voltammetry curve of the Metglas/ZnO/Hb electrode in PBS solution is shown in Figure 4.26c. It was used to estimate the midpoint redox potential of the immobilised hemoglobin. As the applied potential was ramped from 1.0 V to -1.0 V and reversed vs Ag/AgCl, the Metglas/ZnO/Hb electrode exhibits in addition to the film charging currents, nearly reversible, but not equivalent well-defined reduction (-0.35 V) and oxidation(+0.15 V) peaks. These peaks are assigned to Hb reduction Fe (II) and re-oxidation Fe (III). The Fe (III)/Fe (II) redox chemistry of heme is termed quasi-reversible as the peak-to-peak separation was > 60 mV and the peak oxidation current was typically

much less than the reduction peak current[48]. These peaks are clearly absent from the CVs of the same electrode before the immobilisation of Hb. It clearly demonstrates that the immobilized protein is electroactive and that it could be used for the sensing of H_2O_2.

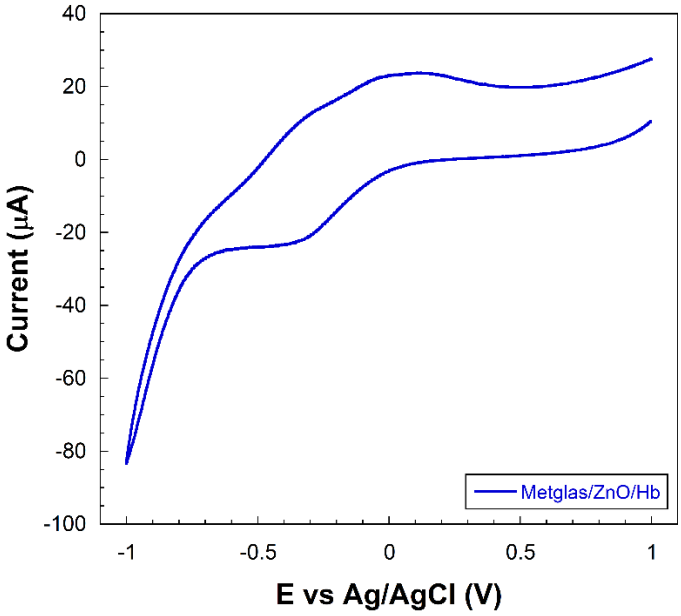

Figure 4.26c. Cyclic voltammetry curve of Metglas/ZnO/Hb electrode at a scan rate of 0.1 V/s.

Finally, Figure 4.26d shows all the above mentioned different curves of the three electrodes, plotted together for direct comparison. It is evident in the plot that the metallic metglas gives back a greater and broader current with respect to the other two electrodes, which is due to its conductive nature.

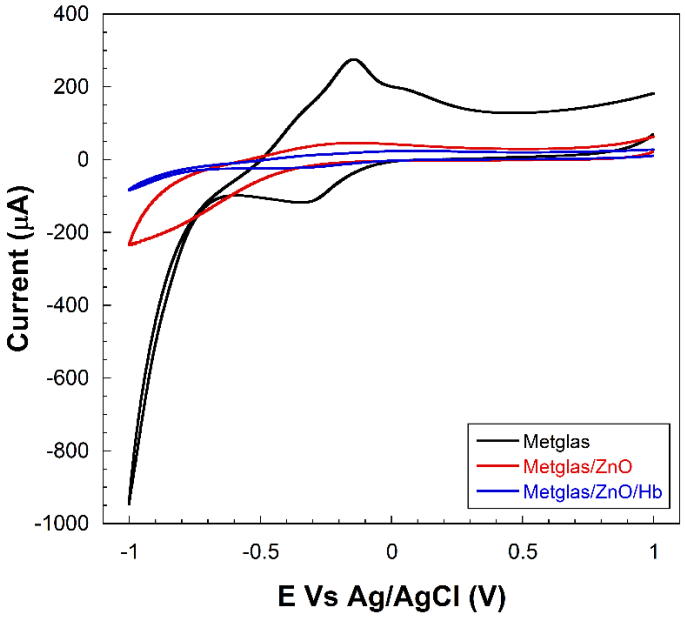

Figure 4.26d. Cyclic voltammetry curves of the electrode at different stages at a scan rate of 0.1 V/s, Metglas 2826MB (black), Metglas/ZnO (red) and Metglas/ZnO/Hb (blue) for comparison purposes.

4.2.3.3. Simultaneous detection experiments

- ***Control curves***

In order to ensure that the signal being detected in the measurements was due to the oxidation of the immobilised Hb by H_2O_2, we performed control experiments without any presence of H_2O_2, which means that those measurements were made in plain PBS solution. In Figure 4.27 are shown the CV scans taken every 5 minutes in a total time period of 50 minutes. It is evident that there is no much activity during these 50 minutes as it was expected.

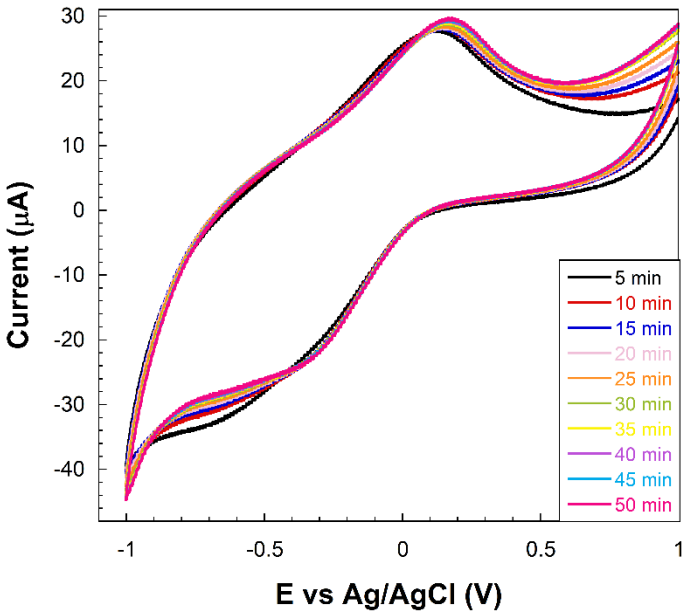

Figure 4.27. CVs of a Metglas/ZnO/Hb electrode at a scan rate of 0.1 V/s at specific time intervals (5 - 50 min) in PBS solution, without H_2O_2 presence.

In Figure 4.28 are shown the magnetoelastic resonance measurements at the same conditions, in absence of H_2O_2. It can be seen a typical resonance signal which is received when the Metglas/ZnO/Hb electrode is immersed in the PBS solution, where the continuous red line is a Gaussian fit to the data. From those curves the resonance frequency is extracted by the x-value at the peak, and the evolution of those resonance frequencies for different times can also be observed in Figure 4.28. It is clear that the curve is quite flat with an error of about 0.02 kHz.

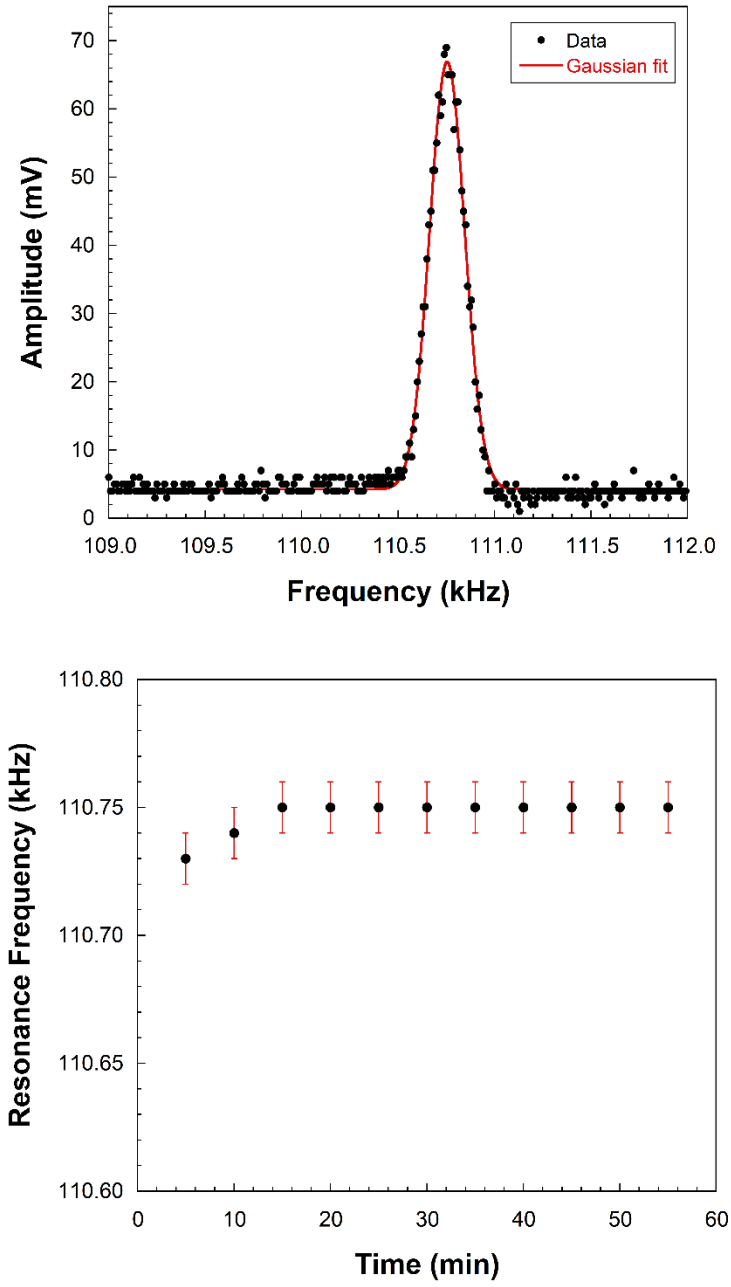

Figure 4.28. Magnetoelastic resonance measurement and resonance frequency evolution versus time when the electrode is immersed in PBS solution.

- ***H_2O_2 detection curves***

To test the electrochemical reaction between Hb and H_2O_2, 5 µL aliquots of 30 µM H_2O_2 solution were added each time successively in the cell where the Metglas/ZnO/Hb electrode was immersed in PBS buffer, in order to increase the H_2O_2 concentration by 25 µM at each step. Each amount was added at time intervals of 5 minutes and CV scans were obtained right afterwards (30 seconds) and shortly before the end of the interval (<5 minutes). CV obtained scans at 50 µM step additions of H_2O_2 are shown in Figure 4.29. This plot reveals an intense electrochemical activity (electrocatalytic responses), as expected, since it is well known that Hb can catalyse the reduction of H_2O_2.

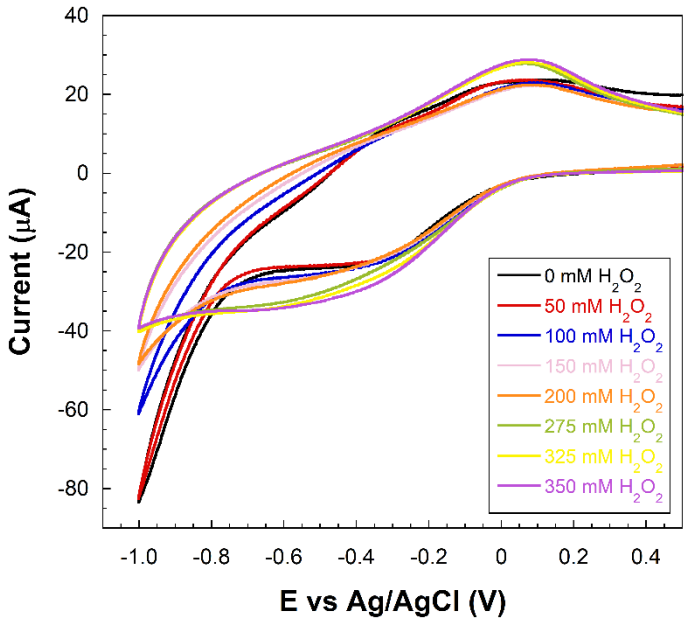

Figure 4.29. CVs obtained for a Metglas/ZnO/Hb electrode in PBS buffer before and after the addition of increasing amounts (50-350 µM) of H_2O_2 at a scan rate of 0.1 V/s (sensing signals measured 30 seconds after each addition of H_2O_2)

Hb was immobilised in the mesopores of the ZnO film in a stable and functional way and it was able to interact with the semi-conducing substrate as well as the aqueous electrolyte solution. When the H_2O_2 molecules were added to the electrolyte solution in the cell, they could easily enter the mesopores of the ZnO film, interacting there with the immobilized molecules of Hb, which were reduced by the four bound iron atoms on each of the heme molecules of Hb. In Figure 4.29 these interactions between the immobilised Hb and the added H_2O_2 are displayed by the gradual increase of the current peaks and their gradual shift to the right (to less negative biases). Figure 4.30 shows the peak current versus the H_2O_2 concentration with a good linear correlation (R = 0.99). This plot proves that the CV method is not only sensitive enough to detect the electrochemical changes that take place between Hb and H_2O_2 but also that the corresponding signals produce a linear calibration plot that could be used as a H_2O_2 biosensor.

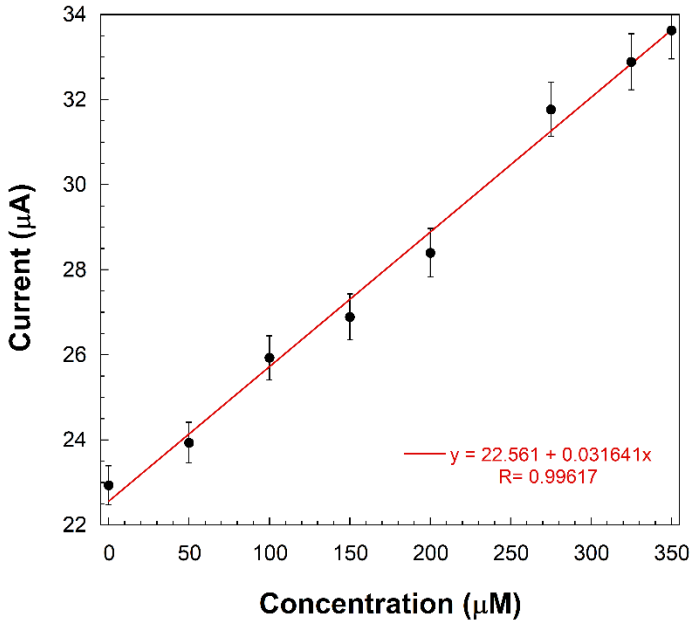

Figure 4.30. Evolution of the peak current values vs H_2O_2 concentration.

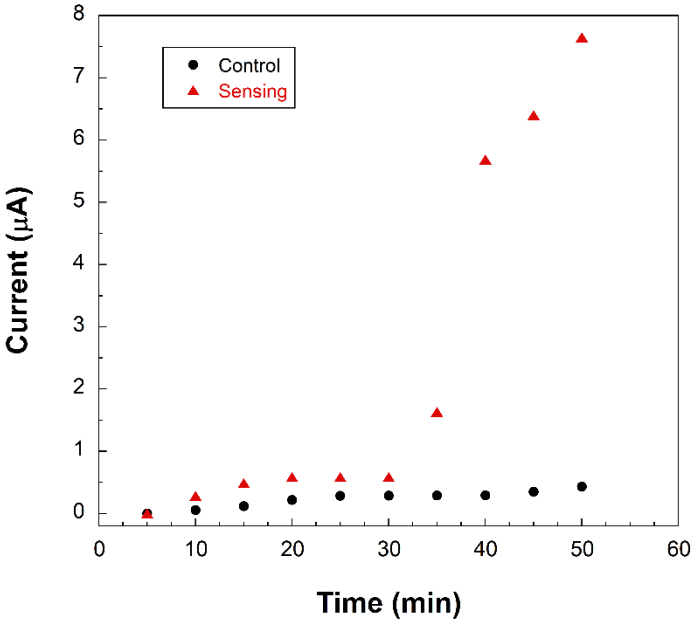

Figure 4.31. Comparison of the control peak current (circles) obtained from the CVs of a Metglas/ZnO/Hb electrode in PBS solution and the corresponding sensing current (triangles) when H_2O_2 is added in the solution.

For comparison, the peak current of CV curves, is plotted in Figure 4.31 as solid circles for the control experiments together with the corresponding signal (solid triangles) which is received when H_2O_2 is added in the solution. The control experiment produces a flat response with a small error of about 0.5 μA and it is obvious that the changes brought up by the electrochemical reaction of H_2O_2 with the Hb, produce a big enough sensing signal of about 8 μA in variation, much larger than the above error. Thus, CV method is a sensitive enough method to detect the electrochemical reactions caused by the addition of H_2O_2.

Figure 4.32 depicts the magnetoelastic data, which show that the resonance frequency of the sensor has a linear drop versus time as the H_2O_2 concentration increases. Additionally, the total change of 0.075 kHz is larger than the error of 0.02 kHz observed at the control experiment and thus the change should be related to the H_2O_2 concentration. As it was mentioned in the introduction, the magnetoelastic sensors are used as microbalances since the resonance frequency depends on the mass load. For the particular metglas ribbon used, calibration with known small

mass loads gives a calibration factor of -1.4 kHz/mg. From this factor and the maximum H_2O_2 concentration of 350 µM, it can be concluded that there was a corresponding mass increase on the sensor of 152 ng/µM, which is most probably due to the H_2O_2 adsorption in the mesopores of the ZnO film during the electrochemical reaction.

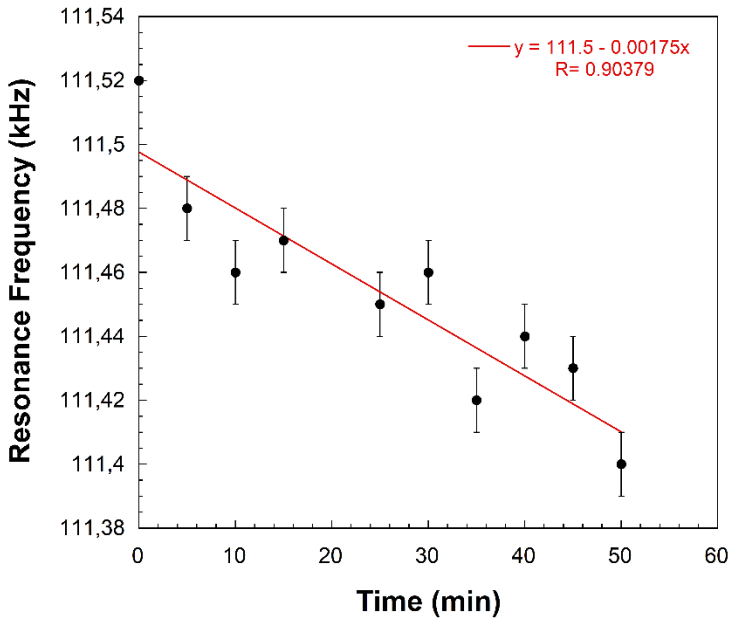

Figure 4.32. Magnetoelastic resonance data of a Metglas/ZnO/Hb electrode measured 5 mins after the addition of increasing aliquots of H_2O_2.

The influence in the sensing experiments of the time interval between the addition of H_2O_2 aliquots and the electrochemical detection was also tested. For that purpose, three different cases were analysed (3 different concentrations of H_2O_2 and two different time intervals: 30 s and 5 min after each addition of H_2O_2). The results are shown in Figure 4.33. Comparing the obtained CV scans at each time interval, it can be clearly seen that the detection happens instantly, so it can be affirmed that there is no time dependence in the electrochemical detection process.

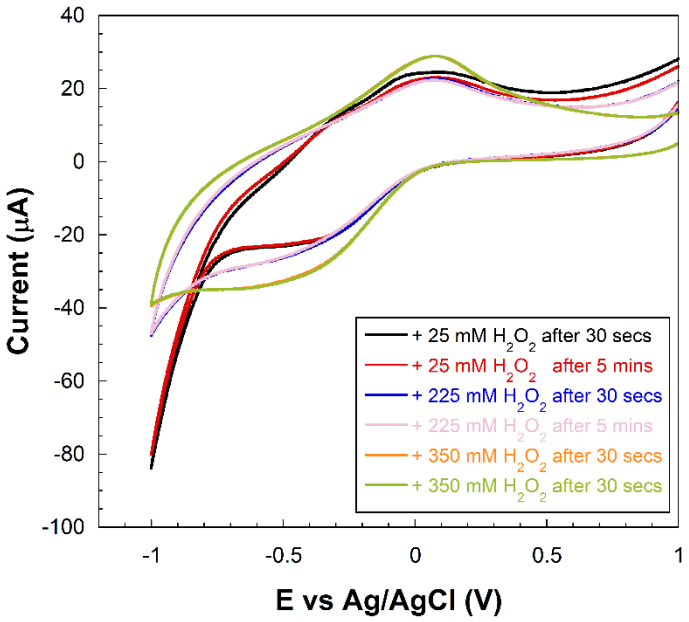

Figure 4.33. CVs of a Metglas/ZnO/Hb electrode at a scan rate of 0.1 V/s after the addition of 3 different concentrations of H_2O_2 measured after 30 s and 5 min after each addition.

4.3. Summary and conclusions

In this chapter it has been demonstrated that it is possible to directly coat a magnetoelastic amorphous material in the form of ribbon with a zinc oxide active layer. Parameters as the temperature or time of the synthesis conditions are a key factor to ensure that the deposited layer is only composed by zinc oxide, and not only affect the composition of the formed layer but also the morphology of the final precipitate. The ZnO layers deposited by three different methods were fully characterized by XRD, SEM and PL. From the obtained results, it has to be concluded that among the different methods used and analysed to cover the surface of the ribbon, the best way to deposit a homogenous layer of ZnO is by making a direct casting with the previously synthetized ZnO nanoparticles. Other deposition procedures do not ensure that the formed layer is only constituted by ZnO without other impurities which can be obtained due to the fabrication or deposition processes. Also, in most of

the cases the formed film did not homogeneously cover the surface of the ribbon, which is another important factor for our purposes, that is to use them later as biosensors.

Even more, once the best procedure to make the ZnO films onto the magnetoelastic material has been determined, it has also been possible to determine the Young modulus of the deposited ZnO film by making several successive depositions and by measuring the change at each step in the magnetoelastic resonant frequency as the mass increment of the future sensor platform will happen. According to the employed method, a straight line is obtained when plotting the Young modulus of the whole composite material (resonant platform) versus the thickness relation of each layer (Metglas 2826MB3 + ZnO layer), and from that evolution Young's modulus of the Metglas 2826MB3 and what is more important of the deposited ZnO film can be obtained from the slope of the obtained linear dependence. Thus, after 6 depositions of the ZnO material, a good layer of about 1 μm thickness and Young's modulus of about 60 GPa, has been obtained. This value is in good agreement with other values reported for other morphologies of ZnO nanostructures synthesised.

Finally, the fabrication of a biosensor to monitor the oxidation of the hemoglobin protein (Hb) has been presented. The sensor was fabricated to simultaneously detect the oxidation of the Hb due to its reaction with H_2O_2 by two different methods, by cyclic voltammetry and magnetoelastic resonance. For that purpose, hemoglobin has been immobilised onto the surface of the previously prepared Metglas/ZnO bilayer, thus constructing both a sensitive modified voltammetry electrode and a magnetoelastic biosensor. In this way it has been possible to monitor the reaction of the immobilized protein with specific aliquots of H_2O_2 by using simultaneously cyclic voltammetry and magnetoelastic detection procedures. The voltammetry measurements reveal direct electrochemical behaviour of Hb and display good electrocatalytical response to the reduction of H_2O_2. The measured catalysis currents increase linearly with the H_2O_2 concentration in a wide range of 25-350 μM with a correlation coefficient 0.99. The detection limit is 25-50 μM. Moreover, the Metglas/ZnO/Hb electrode displays a rapid response (30 s) to H_2O_2, and exhibits good stability and reproducibility of the

measurements. On the other hand, the simultaneously performed magnetoelastic measurements show a small linear mass increase versus the H_2O_2 concentration with a slope of 152 ng/μM, a mass change that is most probably due to the H_2O_2 adsorption in ZnO during the electrochemical reaction. No such effects were detected during the control experiment when only the PBS solution was present for a long time, a fact that strongly support the previous conclusion.

References

[1] C.F. Klingshirn, B.K. Meyerm A. Waag, A. Hoffmann and J. Geurts, "Zinc oxide, from fundamental properties towards novel applications [Chapter 13: Past, present and future applications]", Springer (2010). ISBN 10: 978-3-642-10576-0.

[2] Kasap Capper Editors, "Handbook of Electronic and Photonic Materials [Part B: Growth and Characterization, Chapter 16. Wide-Bandgap II-VI Semiconductors: growth and properties]", (M. Isshiki and J. Wang) Springer (2017). ISBN: 978-3-319-48931-5. DOI: 10.1007/978-3-319-48933-9.

[3] A. Janotti and C.G. Van de Walle, "Fundamentals of zinc oxide as a semiconductor", Reports in Progress in Physics 72 (2009) (12) 1-29. DOI: 10.1088/0034-4885/72/12/126501.

[4] C. Jagadish and S.J. Pearson, "Zinc oxide bulk, thin films and nanostructures: Properties and applications [Chapter 1: Basic properties and applications of ZnO]" (V.A. Coleman and C. Jagadish), Elsevier (2011). ISBN 10: 0-08-044722-8.

[5] A.V. Desai and M.A. Haque, "Mechanical properties of ZnO nanowires", Sensors and Actuators A: Physical 134 (2007) 169-176. DOI: 10.1016/j.sna.2006.04.046.

[6] S. Wei, S. Wang, Y. Zhang and M. Zhou, "Different morphologies of ZnO and their ethanol sensing property", Sensors and Actuators B: Chemical 192 (2014) 480-487. DOI: 10.1016/j.snb.2013.11.034.

[7] X.D. Bai, P.X. Gao, Z.L. Wang and E.G. Wang, "Dual-mode mechanical resonance of individual ZnO nanobelts", Applied Physics Letters 82 (2003) (26) 4806-4808. DOI: 10.1063/1.1587878.

[8] J.Y. Lao, J.Y. Huang, D.Z. Wang and Z.F. Ren, "ZnO nanobridges and nanonails" Nano Letters 3 (2003) (2) 235-238. DOI: 10.1021/nl025884u.

[9] P.X. Gao, W. Mai and Z.L. Wang, "Superelecticity and nanofracture mechanics of ZnO nanohelices" Nano Letter 6 (2006) (11) 2536-2543. DOI: 10.1021/nl061943i.

[10] S. Rackauskas, O. Klimova, H. Jiang, A. Nikitenko, K.A. Chernenko, S.D. Shandakov, E.I. Kauppinen, O.V. Tolochko and A.G. Nasibulin, "A novel method for continuous synthesis of ZnO tetrapods" Journal of Physical Chemistry C 119 (2015) (28)16366-16373. DOI: 10.1021/acs.jpcc.5b03702.

[11] Y. Huang, Y. Zhang, J. He, Y. Dai, Y. Gu, Z. Ji and Z. Zhou, " Fabrication and characterization of ZnO comb-like nanostructures" Ceramics International 32 (2006) (5) 561-566. DOI: 10.1016/j.ceramint.2005.04.011.

[12] Z.L. Wang, "Zinc oxide nanostructures: growth, properties and applications", Journal of Physics: Condensed Matter 16 (2004) R829-R858. DOI: 10.1088/0953-8984/16/25/R01.

[13] J.P. Parekh, S. Shen and G. Thomas, "Magnetoelastic Rayleigh wave delay line and convolver utilizing ZnO transducer" IEEE 1975 Ultrasonic Symposium. DOI: 10.1109/ULTSYM.1975.196499.

[14] A. Wei, L. Pan and W. Huang, "Recent progress in the ZnO nanostructure-based sensors" Materials Science and Engineering B 176 (2011) 1409-1421. DOI: 10.1016/j.mseb.2011.09.005.

[15] C.H. Lin, B.S. Chiou, C.H. Chang and J.D. Lin, "Preparation and cathodoluminescence of ZnO phosphor" Materials Chemistry and Physics 77 (2003) (3) 647-654. DOI: 10.1016/S0254-0584(02)00120-7.

[16] R. Pietruszka, B.S. Witkowski, S. Gieraltowska, P. Caban, L. Wachnicki, E. Zielony, K. Gwozdz, P. Bieganski, E. Pleaczek-Popko and M. Godlewski, "New efficient solar cell structures based on zinc oxide nanorods" Solar Energy Materials and Solar Cells 143 (2015) 99-104. DOI: 10.1016/j.solmat.2015.06.042.

[17] A.F. Kohan, G. Ceder, D. Morgan and C.G. Van de Walle, "First-principles study of native point defects in ZnO" Physical Review B 61 (2000) 15019. DOI: 10.1103/PhysRevB.61.15019.

[18] B. Guo, Z.R. Qiu and K.S. Wong, "Intensity dependence and transient dynamics of donor-acceptor pair recombination in ZnO thin

films grown on (001) silicon" Applied Physics Letters 82 (2003) 2290. DOI: 10.1063/1.1566482.

[19] F.K. Shan, G.X. Liu, W.J. Lee, G.H. Lee, I.S. Kim and B.C. Shin, "Aging effect and origin of deep-level emission in ZnO thin film deposited by pulsed laser deposition", Applied Physics Letters 86 (2005) 221910. DOI: 10.1063/1.1939078.

[20] F.H. Leiter, H.R. Alves, A. Hofstaetter, D.M. Hofmann and B.K. Meyer, "The oxygen vacancy as the origin of a green emission in undoped ZnO" Physica Status Solidi B 226 (2001) (1) R4. DOI: 10.1002/1521-3951(2000107)226.

[21] M. Liu, A.H. Kitai and P. Mascher, "Point defects and luminescence centres in zinc oxide and zinc oxide doped with manganese", Journal of Luminescence 54 (1992) (1) 35-42. DOI: 10.1016/0022-2313(92)90047-D.

[22] D.C. Reynolds, D.C. Look, B. Jogai, J.E. Hoelscher, J.E. Hoelscher, R.E. Sherriff, M.T. Harris and M. J. Callahan, "Time-resolved photoluminescence lifetime measurements of the Γ_5 and Γ_6 free excitons in ZnO" Journal of Applied Physics 88 (2000) (4) 2152-2153. DOI: 10.1063/1.1305546.

[23] A. Chrissanthopoulos, S. Baskoutas, N. Bouropoulos, V. Dracopoulos, P. Poilopoilos and S.N. Yannopoulos, "Synthesis and characterization of ZnO/NiO p-n heterojunctions: ZnO nanorods grown on NiO thin film by thermal evaporation", Photonics and Nanostructures – Fundamentals and Applications 9 (2011) (2) 132-139. DOI: 10.1016/j.photonics.2010.11.002.

[24] M.P. Manoharan, A.V. Desai, G. Neely, and M.A. Haque. "Synthesis and elastic characterization of zinc oxide nanowires", Journal of Nanomaterials (2008) vol. 2008, Article ID 849745, 7 pages. DOI: 10.1155/2008/849745.

[25] X. Gao, R. Zhen, Y. Zhang and C.A. Grimes, "Detecting penicillin in mil with a wireless magnetoelastic biosensor", Sensor Letters 7 (2009) 6-10. DOI: 10.1166/sl.2009.1002.

[26] N. Bouropoulos, D. Kouzoudis, C.A. Grimes, "The real-time, in situ monitoring of calcium oxalate and brushite precipitation using

magnetoelastic sensors", Sensors and Actuators B: Chemical 1096 (2005) 227–232. DOI: 10.1016/j.snb.2004.12.054.

[27] L.D. Landau and E.M. Lifshitz. "Theory of Elasticity" Second edition, Vol. 7 of "A Course of Theoretical Physics", Pergamon Press (1970).

[28] J. D. Livingston, "Magnetomechanical properties of amorphous metals", Physica Status Solidi A 70 (1982) 591-596. DOI: 10.1002/pssa.2210700228.

[29] T. Baimpos, I. G. Giannakopoulos, V. Nikolakis and D. Kouzoudis, "Effect of gas adsorption on the elastic properties of faujasite films measured using magnetoelastic sensors", Chemistry of Materials 20 (2008) (4) 1470-1475. DOI: 10.1021/cm7026509.

[30] I.B. Kobiakov. "Elastic, piezoelectric and dielectric properties of ZnO and CdS single crystals in a wide range of temperatures", Solid State Communications 35 (1980) (3) 305–310. DOI: 10.1016/0038-1098(80)90502-5.

[31] J. Song, X. Wang, E. Riedo, and Z. L. Wang, "Elastic property of vertically aligned nanowires", Nano Letters 5 (2005) (10) 1954–1958. DOI: 10.1021/nl051334v.

[32] A.V. Desai and M.A. Haque, "Mechanical properties of ZnO nanowires", Sensors and Actuators A: Physical 134 (2007) 169–176. DOI: 10.1016/j.sna.2006.04.046.

[33] L.W. Ji, S.J. Young, T.H. Fang, and C.H. Liu, "Buckling characterization of vertical ZnO nanowires using nanoindentation", Applied Physics Letters 90 (2007) (3) Article ID 033109, 3 pages. DOI: 10.1063/1.2431785.

[34] X.D. Bai, P.X. Gao, Z.L. Wang, and E. G.Wang, "Dual-mode mechanical resonance of individual ZnO nanobelts", Applied Physics Letters 82 (2003) (26) 4806–4808. DOI: 10.1063/1.1587878.

[35] Z.L. Wang, "Zinc oxide nanostructures: growth, properties and applications", Journal of Physics: Condensed Matter 16 (2004) (25) R829–R858. DOI: 10.1088/0953-8984/16/2R01.

[36] W. Chen, S. Cai, Q.Q. Ren, W. Wen and Y.D. Zhao, "Recent advances in electrochemical sensing for hydrogen peroxide: a review", Analyst 137 (2012) (1) 49–58. DOI: 10.1039/c1an15738h.

[37] M. Shamsipur, A. Pashabadi and F. Molaabasi, "A novel electrochemical hydrogen peroxide biosensor based on hemoglobin capped gold nanoclusters-chitosan composite", RSC Advances 5 (2015) 61725-61734. DOI: 10.1039/C5RA09216G.

[38] Y. Xu, C. Hu and S. Hu, "A hydrogen peroxide biosensor based on direct electrochemistry of hemoglobin in Hb-Ag sol films", Sensors and Actuators B: Chemical 130 (2008) (2) 816-822. DOI: 10.1016/j.snb.2007.10.048.

[39] M. Weissbluth, "Molecular biology" Biochemistry and Biophysics vol. 15 (1974) p. 68, Springer, New York.

[40] C.L. Zhang, M.C. Liu, P. Li, Y.Z. Xian, Y.X. Chang, F.F. Zhang, X.L. Wang and L.T. Jin, "Fabrication of ZnO nanorods modified electrode and its application to the direct electrochemical determination of hemoglobin and cytochrome c", Chinese Journal of Chemistry 23 (2005) (2) 144-148. DOI: 10.1002/cjoc.200590144.

[41] G. Duan, Y. Li, Y. Wen, X. Ma, Y. Wang, J. Ji, P. Wu, Z. Zhang and H. Yang, "Direct electrochemistry and electrocatalysis of Hemoglobin/ZnO-Chitosan/nano-Au modified glassy carbon electrode", Electroanalysis 20 (2008) n.22, 2454–2459. DOI: 10.1002/elan.200804337.

[42] J. Rifkind, E. Nagababu, S. Ramasamy and L. B. Ravi, "Hemoglobin redox reactions and oxidative stress", Redox Report 8 (2003) No. 5. DOI 10.1179/135100003225002817.

[43] X. Fang, Y. Bando, M. Liao, U.K. Gautam, C. Zhi, B. Dierre, B. Liu, T. Zhai, T. Sekiguchi, Y. Koide and D. Golberg, "Single-crystalline ZnS nanobelts as ultraviolet-light sensors", Advanced Materials 21 (2009) 2034-2039. DOI: 10.1002/adma.200802441.

[44] A. Wei, C.X. Xu, X.W. Sun, W. Huang and G.Q. Lo, "Field emission from hydrothermally grown ZnO nanoinjectors", Journal of Display Technology 4 (2008) (1) 9-12. DOI: 10.1109/JDT.2007.901569.

[45] Z.L. Wang, "Towards self-powered nanosystems: from nanogenerators to nanopiezotronics", Advanced Functional Materials 18 (2008) 3553-3567. DOI: 10.1002/adfm.200800541.

[46] T.L. Mollan and A.I. Alayash, "Redox reactions of Hemoglobin: mechanism of toxicity and control", Antioxidants & Redox Signaling 18 (2013) (17) 2251-2253. DOI: 10.1089/ars.2013.5195.

[47] C. Gonga, Y. Shena, J. Chena, Y. Songa, S. Chena, Y. Songa and L. Wanga, "Microperoxidase-11@PCN-333 (Al)/three-dimensional microporous carbon electrode for sensing hydrogen peroxide" 0925-4005/ 2016 Elsevier B.V.

[48] E. Topoglidis, A.E.G. Cass, B. O'Regan and J. R. Durrant, "Immobilization and bioelectrochemistry of proteins on nanoporous TiO2 and ZnO films", Journal of Electroanalytical Chemistry 517 (2001) 20-27. DOI: 10.1016/S0022-0728(01)00673-8.

[49] P.G. Stoyanov and C.A. Grimes, "A remote query magnetostrictive viscosity sensor", Sensors and Actuators A: Physical 80 (2000) 8-14. DOI: 10.1016/S0924-4247(99)00288-5.

[50] A. Altube and A.R. Pierna, "Thermal and electrochemical properties of cobalt containing Finemet type alloys", Electrochemica Acta 49 (2004) 303-311. DOI: 10.1016/j.electacta.2003.08.012.

[51] A.J. Bard and L.R. Faulkner, "Electrochemical Methods Fundamentals and Applications", Second edition, John Wiley & Sons, New York, (2001). ISBN: 978-0-471-04372-0.

5. Magnetoelastic resonant platforms for gas detection

This chapter is devoted to the practical use of magnetoelastic resonant platforms for gas detection. Zeolites will act as active layer in this functionalized resonant strips. Three different zeolites, LTA, MFI and FAU will be directly synthesized by hydrothermal methods onto the surface of the resonant platforms and will be used to trap the target analyte, ortho-xylene. O-xylene is a volatile organic compound that is very hazardous in case of skin or eye contact and slightly hazardous in case of ingestion or inhalation. As in the previous chapter, the aim is to enable the fabrication from the very first state the whole sensor material, starting from homemade magnetoelastic ribbons and ending with the zeolite sensitive membrane.

5.1. Introduction

In previous chapters, the use of magnetoelastic materials with several purposes has been described. Magnetoelastic materials have been use to determine the Young modulus of a ZnO deposited layer or as biosensors to determine the oxidation of hemoglobin due to the reaction with H_2O_2. As it has been previously explained, magnetoelastic ribbons coated with an active layer can be used for applications as chemical or biological sensors.

Magnetoelastic materials can be also used for gas sensing applications, if the active layer, the coating of the magnetoelastic material, is sensitive to a target gas molecule. Depending on the nature of this active layer, sensors for different gases can be created[1]. For such detection, the active layer can be a metal oxide film, a polymer, a metal, an inorganic material or an organic membrane.

Concerning the metal oxides, TiO_2 has been used for different purposes. For example, if the material that coats the magnetoelastic ribbon responds to humidity by absorbing ambient moisture, then the resonant frequency would be expected to decrease when the humidity increases, due to the mass absorbed by the sensor. With this purpose, magnetoelastic materials in combination with a moisture-absorbing layer such as TiO_2 or Al_2O_3, have been used as humidity sensors[2]. Other authors have reported the use of magnetoelastic sensors coated with Pt-TiO_2 for the detection of ethylene, an organic gas compound that works as a plant hormone in the regulation of metabolic processes which is crucial for both fruit ripening and plant respiration. For this particular case, a 155 nm coated sensor showed a shift of 65 Hz in the resonant frequency in response to 50 ppm ethylene[3].

Polymers, as polystyrene sulfonic acid (PPSA), have been also used to detect humidity[4]. Other polymers as acrylamide or isooctylacrylate have been used as active layers to detect carbon dioxide concentrations[5]. Similarly, ammonia sensors have been fabricated by coating magnetoelastic materials with a layer of poly (acrylic acid-co-

isooctylacrylate)[6]. In addition, a commercial polymer, bayhydrol-110, has been used as an active layer for volatile organic compound detection[7].

Selective absorption is also possible by using other kind of materials as sensitive layers: for example, mercury vapour was achieved by coating a magnetoelastic sensor with gold[8], while carbon nanotubes were used to sense CO_2[4].

The experiments described in this chapter have been carried out at the Foundation for Research and Technology (FORTH) and the Institute of Chemical Engineering Science in Patras (Greece), under the supervision of Doctor Dimitris Kouzoudis and with the help of Vasiliki Tsoukala.

5.2. VOC detection by functionalization of MRPs with zeolites

As it has been explained in this work magnetoelastic resonant platforms covered with an active material are able to detect a wide range of environmental, physical, chemical or even biological parameter. One of those active layer materials can be zeolites, which have been used to trap and detect several gases as carbon dioxide[9], light hydrocarbons[10] or volatile organic compounds (VOC)[11].

5.2.1. Introduction to zeolites

Zeolites are porous crystalline aluminosilicate materials that can have natural or synthetic origin. Although all the aluminosilicates share the same basic chemical composition, the different atom and molecular arrangements lead to structures with different properties. Zeolites are constructed from linked TO_4 tetrahedra (where T = Al^{3+} or Si^{4+}) joined through shared oxygen atoms, and forming three-dimensional framework that defines a regular system of voids and channels of molecular

dimensions. The first zeolite was identified in 1756 by the Swedish mineralogist Friedrich Axel Cronstedt, who observed that on heating the stones he had gathered in a blow-pipe flame, they dance about in a froth of hot liquid and steam, appearing as if the stones themselves were boiling. He thus coined the name 'zeolite' which from Greek derivation (*zein*, 'to boil'; *lithos*, 'a stone') means 'stones that boil'[12].

Nowadays, the International Zeolite Association (IZA)[13] database contains crystallographic data and information on the structure of over 232 different types of zeolites. IZA has set up a database and has established an international code of designations using three letters for the different structures of both natural and synthetic zeolites. Each code also corresponds to a different grid topology and its name usually is derived from the first three letters of the zeolite name or from researchers phrases. For example, FAU comes from Faujasite mineral, LTA comes from Linde Type A and MFI corresponds to Mobil Five (number)[14]. Those codified names are extremely useful in cases where there are many names for the same topology. In addition to the type of a mesh of zeolites, its chemical composition is also important in determining its properties. The general formula describing the chemical composition of zeolites is $M_{y/m}^{m+}\left[(SiO_2)_x(AlO_2^-)_y\right]\cdot nH_2O$, where M denotes a cation with charge m+, n corresponds to the number of water molecules and the sum of (x+ y) is the total number of Si and Al tetrahedrons present in the unit cell[15].

Different zeolite structures are formed by different arrangements and coordination structures of the TO_4 tetrahedra. The grid of pure silicate (SiO_2) does not have an electric charge since silicon has valence +4. Conversely, the existence of trivalent aluminium requires the existence of cations for balancing the electric charge. That should be equalized by M cations electrostatically bonded to the grid to ensure the electrical neutrality in the crystal. Nevertheless, AlO_4 compounds have not been observed on zeolites. As Loewenstein[17] first explained two tetrahedrons AlO_4 cannot occur in adjacent positions within the zeolite lattice, the repulsive electrostatic forces between the similarly charged aluminium squares make that compound extremely unstable. Due to this Loewenstein claimed that the Si/Al ratio should be between one and

infinite; 1 < (Si/Al) < ∞. Typical cations in natural zeolites are metals such as Na^+, K^+ or alkaline earths. In synthetic zeolites, the cation may be either inorganic or organic. The ion exchange of the cationic zeolites necessary for the electrical neutrality can change their important properties such as the pore size, conductivity or rheological and catalytic capabilities. Figure 5.1 shows the structures of four selected zeolites.

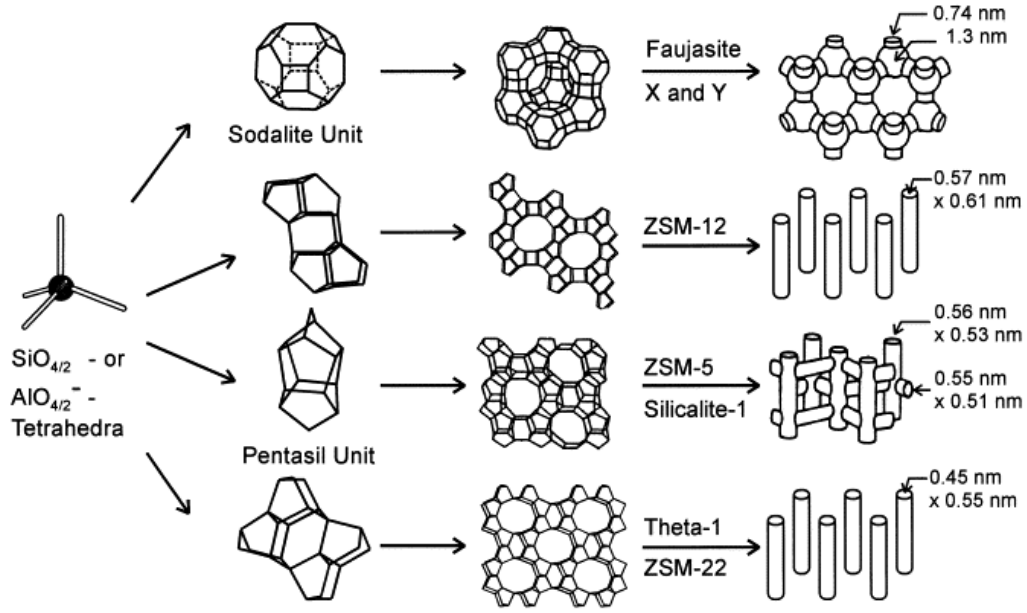

Figure 5.1. Structures or different zeolites and their micropore systems and dimensions[16].

As previously mentioned, the ratio of the silicon to aluminium atoms is an important and characteristic number that can be adjusted affecting so the properties of the zeolite. For example, by increasing the percentage of aluminium the number of interchangeable cations will increase, while the zeolite is characterized as hydrophilic. Such a zeolite can be used, for example as a drying agent in a moisture-rich steam stream. In contrast, hydrophobic high Si/Al zeolites are used to adsorb organic molecules from high humidity or water streams.

In zeolites, the union of the TO_4 tetrahedra is also called primary building block and leads to the formation of secondary building units (SBUs) that consist of single, double and branched rings that can contain from four to sixteen tetrahedrons. Those secondary building block, in

turn, can be properly joined together to form cells and chains. Due to this, the final form of the zeolite structure contains uniform openings being characterized by the presence of pores and cavities of molecular dimensions. The diameter of the pores or channels of zeolites range between 3 and 15 Å.

Zeolites are thermally and chemically stable material, and thus they can be used in a variety of thermochemical environments. Based on its chemical properties the most well known application for zeolites is as catalyst.

Nevertheless, due to their high porosity, zeolites have been used for a wide range of other applications. They have demonstrated to be useful for their ability to eliminate and absorb water by about 30% of their weight[18]. They have been also used as ion exchange membranes as they can exchange cations without any significant alteration of their structure[19]. For this reasons the thermodynamics and chemistry of zeolite diffusion, sorption and ion exchange capacity have been extensively studied. In fact, zeolites are thermally and chemically stable materials. Among the applications, the binding of hazardous heavy metals from industrial waste waters through ion exchange, their use as additives in building materials (cement for example) and applications in energy or medicine fields can be remarked[20,21].

Zeolites are often called molecular sieves due to their ability to distinguish different molecules by size, shape or polarity. Besides, due to their unique physicochemical properties described above, they have found many applications as catalysts[22,23], sorbents[24,25], water softeners[26,27], selective membranes[28,29], optoelectronic devices[30,31], sensors[32,33].

The main objective of this section is to develop a new fully homemade magnetoelastic/zeolite sensor which should be able to detect and quantify small amounts of o-xylene. Xylene, in liquid form at room temperature, is a volatile aromatic hydrocarbon produced through petrochemistry, which is used as a solvent in the printing, rubber, paint and leather industries. Exposure to this organic compound can occur via inhalation, ingestion, and eye or skin contact. Xylene causes health effect from both small and also large exposures. The type and severity of health

effects depends on several factors, including the amount of chemical exposed to and the length of time exposed for. The main effect of inhaling xylene vapor is depression of the central nervous system, with symptoms such as headache, dizziness, nausea and vomiting. The effects listed below can occur with exposures to air levels as low as 1000 ppm[34]. Although the hazards of xylene are well documented, most of the less expensive alternatives do not have the same properties, particularly the ability to be miscible with alcohols but not with water. But not only xylene, many of the VOC, are quite hazardous and cause long-term health and environmental problems, even at very low concentrations, being their detection absolutely necessary[35].

Bearing this purpose in mind, the adsorption ability of o-xylene of three different zeolites: LTA, FAU and MFI, deposited onto our homemade magnetoelastic ribbons is going to be compared, together with previous reported results for the same kind of zeolite membranes grown onto a commercial resonant platforms[10,11]. A scheme of the main characteristics and structure of these zeolites can be seen in Figure 5.2 and Table 5.1.

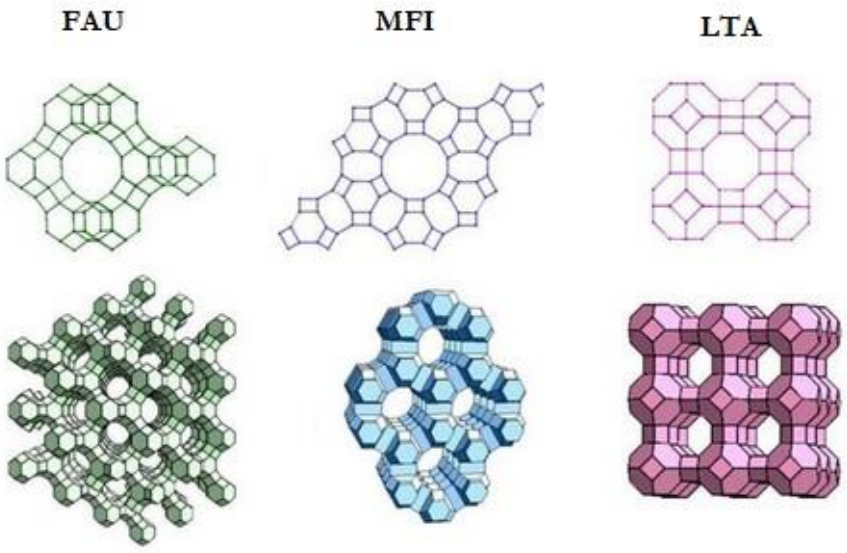

Figure 5.2. FAU, MFI and LTA zeolite structures[36].

✓ Faujasite (FAU)

FAU is a large pore (about 7.3 Å) zeolite , with cubic symmetry which can be synthesized in a variety of compositions that differ in the silicon to aluminium ratio. In FAU structure, each corner of the microstructure represents a Si or Al atom and each line an oxygen bridging atom.

✓ Movil Five (MFI)

MFI can possess different crystal symmetries depending on the temperature, the Si/Al ratio, the nature and the amount of absorbed guest molecules. In this work Al-free state of MFI, also call Silicalite-1, is going to be synthesized. Silicalite-1 has types of channels interconnecting each other. This type of zeolite has an intermediate pore size of 5 Å, between FAU and LTA types.

✓ Linde Type A (LTA)

LTA is a zeolite with silicon to aluminium ratio usually equal to 1. It has a cubic symmetry with eight sodalite cages connected with four-member oxygen bridges. It has pore opening slightly smaller than 4.2 Å, and it is utilized as adsorbent for the separation of n-alkanes from their branched isomers.

Table 5.1. FAU, MFI and LTA zeolites main properties[13].

	FAU	*MFI*	*LTA*
Cell structure	Cubic (Fd3m)	Orthorhombic (Pnma)	Cubic (Pm3m)
Pore size	7.3 Å	5 Å	4.2 Å
Accessible volume	27.4%	9.8%	21.4%

5.2.2. Functionalization of MRPs with zeolites

To develop the sensor elements in this particular case, a homemade magnetoelastic alloy of composition $Fe_{64}Co_{21}B_{15}$ was selected. It was also fabricated by the melt spinning technique previously described and the obtained strip had a width of 2.6 mm and a thickness of approximately 13 μm. The magnetic characterization gave a saturation magnetization value of 1 T and a saturation magnetostriction of 20 ppm. The obtained curves for the hysteresis loop and the measured magnetostriction can be observed in Figure 5.3.

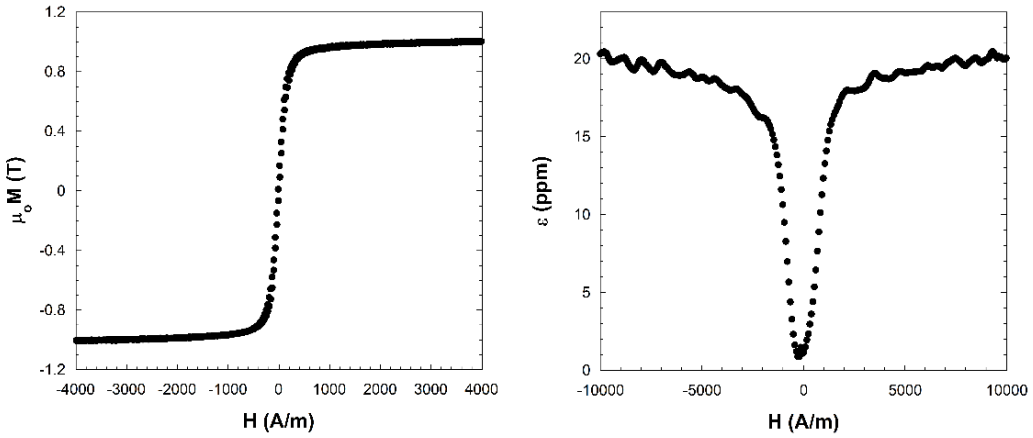

Figure 5.3. Magnetic and magnetostrictive characterization of $Fe_{64}Co_{21}B_{15}$.

The fabrication of the sensor took place in different stages. It starts with the preparation of the sample (cleaning + metallization) and the functionalization of the magnetoelastic resonant platforms with the zeolite. This first stage included the cleaning process made to the magnetoelastic strips, the seeding procedure with the zeolite nanoparticles, (including the seed synthesis in the case it had been made) and the hydrothermal synthesis of the zeolites. In some cases and after the hydrothermal synthesis, an annealing procedure was needed to eliminate the employed organic template. Finally, sensing experiments were made in order to detect the o-xylene gas by using those prepared resonant platforms. In Figure 5.4 a brief scheme of the fabrication processes followed for the three zeolites can be observed.

Sample preparation *cut and clean*			
Magnetoelastic resonant platform protection *metallic coating*			
Functionalization *seeding procedure, hydrothermal synthesis and annealing*			
	FAU	MFI	LTA
Seed synthesis	Commercial NaY	Yes	Yes
Hydrothermal synthesis	7 days 85 °C	5 hours 185 °C	5 hours 100 °C
Organic template removing	3 days 280 °C	5 days 85 °C	No
Sensing experiments			

Figure 5.4. Scheme of the followed procedure for the fabrication of the o-xylene sensors.

❖ *Sample preparation*

The magnetoelastic ribbons were cut in 2 cm long pieces and ultrasonically cleaned, alternatively they were cleaned with methanol and trichloroethylene for 10 minutes. This cleaning procedure was repeated three times in order to remove any dirt from the fabrication or manipulation process. Afterwards, these samples were dried using a heating plate.

When this work was carried out, corrosion resistant samples were not been fabricated yet, so such problems arised when trying to cover the samples with the zeolite membranes. In the first attempts, zeolites synthesis processes were performed simultaneously both in a commercial Metglas 2826MB3 sample and in the $Fe_{64}Co_{21}B_{15}$ homemade alloy. The main idea was to study how the hydrothermal synthesis should be carried out, with a substrate that was already used in the past (having so the guarantee that the synthesis process works on it) and compare with the homemade magnetoelastic resonant platforms case. As it can be

observed in Figure 5.5, a zeolite membrane was formed onto both substrates, showing that hydrothermal synthesis was successfully carried out. Nevertheless, two problems were detected: on the one hand, the formed membrane was not homogeneous in the case of LTA, due to problems that occurred during the synthesis process. On the other hand, corrosion appeared on the homemade $Fe_{64}Co_{21}B_{15}$ samples after the zeolite synthesis, affecting the magnetoelastic material properties. That behaviour was not observed in the commercial Metglas 2826MB3 strips, so it could be inferred that a protective layer was needed in order to avoid corrosion appearance during the sensor development.

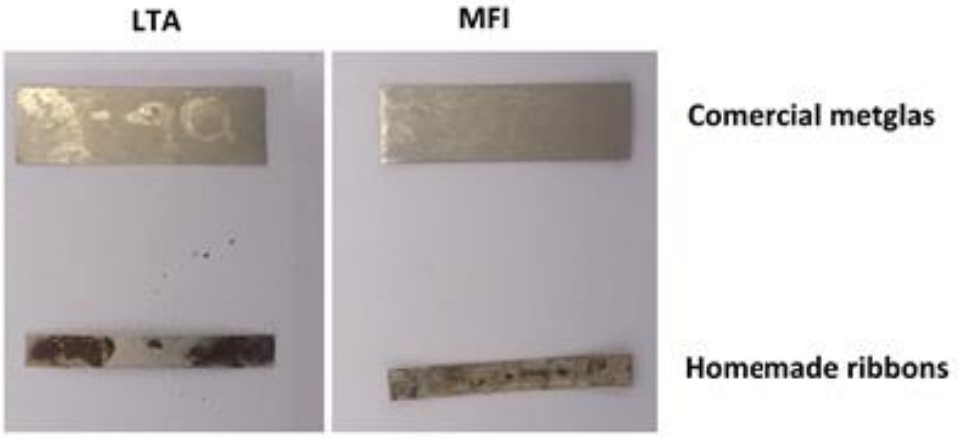

Figure 5.5. First attempt synthesizing LTA and MFI onto commercial metglas (up) and the homemade magnetoelastic ribbon (down). Oxidation can be observed in homemade ribbons but not in commercial ones.

This observation was another strong reason that made us fabricate new corrosion resistant magnetoelastic materials in the form of ribbons, as previously discussed.

❖ *Metallic coating of the MRPs*

Following our observations, once the samples were cleaned, they had to be protected to avoid the corrosion of the surface, and this was achieved by covering the strips with an adequate metallic coating.

Several metal coatings were tested in order to avoid the corrosion damage. All of the tested metals were sputtered onto the surface of our homemade alloys, in order to make a thin protective film. This film must cover the whole surface of the ribbon to ensure the good protection of the sample in aqueous solutions, as the hydrothermal synthesis of zeolites would take place in basic aqueous media.

The first protective coating used was gold (Au). Gold sputtering was performed in the laboratory upon the surface of our magnetoelastic ribbons giving rise to a film of approximately 40 nm thickness. A picture of the employed equipment can be observed in Figure 5.6. To test the gold layer attachment state to the surface of the strip and to ensure that it would protect the ribbon against corrosion, it was directly immersed in water. After a few minutes, a quick detachment of the gold film from the surface of the ribbon was observed. Due to this problem, gold was discarded as a good alternative to protect the samples from corrosion before developing the active zeolite membrane layer.

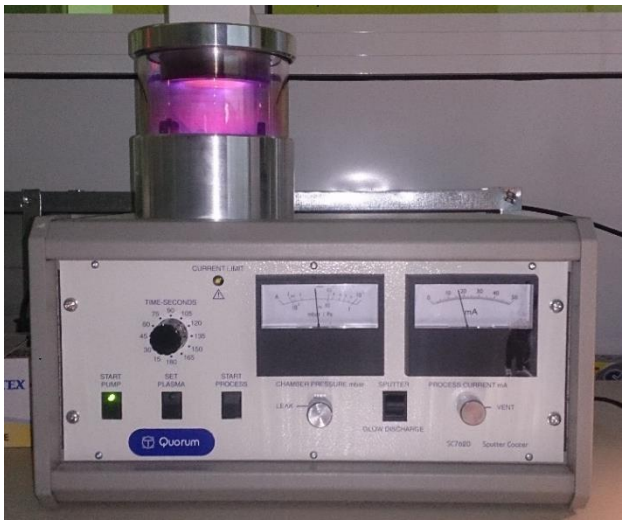

Figure 5.6. Gold sputtering process going on.

As an alternative to gold protective layer, other two metals were tested, chromium (Cr) and titanium (Ti). The sputtering process for those metals was carried out only in one side of the samples. To do this, two different samples were selected to be simultaneously covered with those previously mentioned metals. Both Cr and Ti are supposed to favour

corrosion resistant behaviour (in fact, chromium was chosen in a previous chapter as additive element to develop corrosion resistant metallic alloys). Once the two samples were sputtered with the metals, they were immersed in water for 1 day, to test the adhesion of the deposited layers and the corrosion resistance. In both cases, they seemed to be perfectly deposited and attached onto the surface of the resonant platforms and as expected, the metal-covered side did not present any sign of corrosion, as it happened with the non-covered side.

The next step was to test the zeolite membrane formation. In the first experiment and after the seeding procedure, LTA type membrane was grown onto two samples, one covered with Ti and another one with Cr to compare the results of the formed zeolite membrane and the gas sensing capability. In both cases the zeolite membrane seemed to be successfully formed, as a white film covering the whole surface was observed. Nevertheless, when the first sensing experiments were made, chromium deposited samples did not show any sensing response. A possible explanation can be that the expected zeolite membrane was not properly formed onto the chromium deposited layer. Probably some LTA zeolite structures had been grown around nucleation points created during the seeding procedure giving rise to a non porous membrane. Such good porosity is absolutely required for the good developments of the subsequent sensing experiments.

On the contrary, titanium deposited sample showed o-xylene detection ability on those preliminary experiments. So, titanium was chosen as the best available material to protect the surface of the amorphous alloys from corrosion, allowing also the formation of the zeolite membrane, and without affection to the sensing capability of the whole device (magnetoelastic platform + Ti coating + LTA zeolite membrane).

In what follows, all presented samples and results were performed with the magnetoelastic strips covered onto both sides with a protective titanium layer prior to zeolite synthesis. Figure 5.7 shows the surface of one of the formed LTA membranes. As it can be observed zeolite covered the whole surface of the ribbon creating a quite homogeneous film,

which was after all used for gas sensing experiments, in particular in o-xylene containing atmospheres.

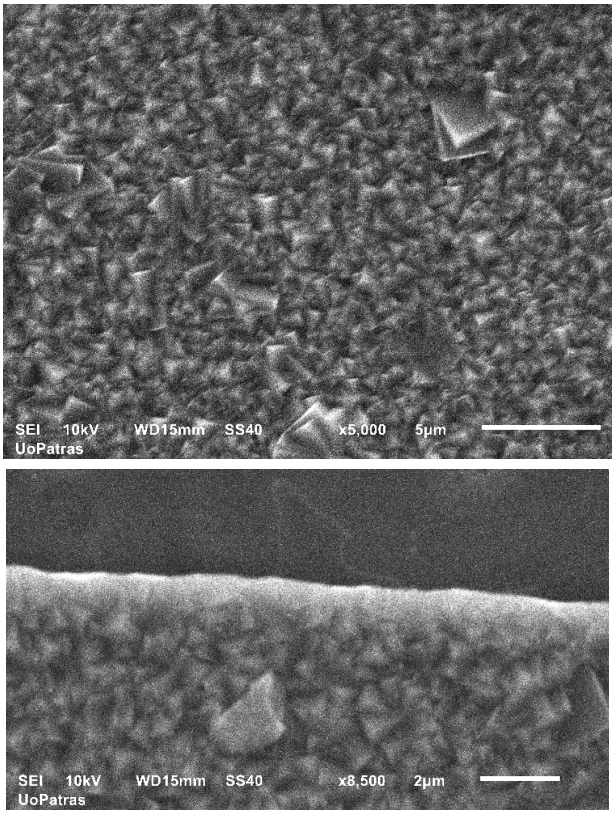

Figure 5.7. LTA zeolite membrane formed onto the surface of a titanium coated magnetoelastic resonant platform.

❖ *Zeolite seed synthesis and seeding procedure*

For the optimal formation of the zeolite membranes onto the metallic substrate, a first seeding step is needed. The deposited seeds would act as nucleation points for the later formation of the zeolite membrane. It would ensure a better homogeneity of the formed membrane that would start growing from the nucleation points until it totally covers the surface of the magnetoelastic alloy. Afterwards, the cleaned-metal-covered magnetoelastic strips were weighted to later be able to ensure that the subsequent processes as the seeding or the zeolite membrane formation succeeded.

Depending on the zeolite type, different kind of seeds will be used. The seeding procedure consisted on dipping the magnetoelastic ribbons onto the seeding solution for a few seconds following a dip-coating procedure, and allowing it to dry. In all the cases, the concentration of the seeding solution was of 1 g of seeds in 100 ml of water. After that, the samples were left at room temperature until the total evaporation of water. This seeding procedure was repeated several times (5-6) to ensure that seeds of the zeolite have been sprayed all over the surface of the resonant platforms. This was done, to assure a more homogenous formation of the zeolite membrane.

- ✓ **FAU** seeding solution was prepared from a commercially available NaY solution of Sigma-Aldrich.

- ✓ **MFI** seeding solution was prepared with previously synthesized MFI seeds.

MFI seed synthesis: all the reactants 19.25 g H_2O, 18.36 g TpAOH (tetrapropylammonium hydroxide), 10.7 g TEOS (tetraethoxysilane) and 0.0158 g NaOH (sodium hydroxide) were stirred together until the hydrolysis of the TEOS took place. The samples were left at room temperature under stirring for a minimum of 24 hours for hydrolysis to take place. When TEOS was hydrolysed, the odour of the solution changed and it became more transparent. The solution was introduced in a polypropylene bottle into the oven at 100 ℃ for 1 day to leave the synthesis to form the seeds. Afterwards, the solution was centrifuged at 9000 rpm for 20 minutes. To clean the obtained particles, water was added under sonication and centrifuged again until the particles were totally cleaned. Finally, the obtained seeds were dried at 100 ℃.

- ✓ **LTA** seeding solution was prepared with previously synthesized LTA nanoseeds[37].

LTA nanoseed synthesis: a first solution 'A' containing 0.19 g NaOH, 14.885 g H_2O, 53.01 g TmAOH (tetramethylammonium hydroxide) was prepared and left stirring for 30 minutes until total homogenization. This first solution 'A' was divided in two; 'A1' where 4.21 g of aluminium isopropioxide and 'A2' where 12 g of the silica source LUDOX 30 were added and both were left under stirring at room temperature for 2 hours. Once the two solutions were well homogenised they were mixed together and poured in a polypropylene bottle at room temperature under magnetic stirring for 4 days. After that, the mixture was placed into the oven at 80 ℃ for 24 hours. To recover the formed particles, the solution was stirred at 7500 rpm for 15 minutes. The supernatant was removed and the particles were cleaned with water under sonication and centrifuged again. This cleaning procedure was repeated until reaching pH 8. Finally, the sample was dried in a porcelain plate at 100 ℃.

- ❖ ***MRP functionalization: zeolite membrane formation by hydrothermal synthesis***

Once the samples were seeded and dried, they were weighted to ensure that seeding procedure had succeeded. The next step of the procedure was to grow the zeolite membrane onto the surface of the magnetoelastic resonant platforms. For this purpose, the seeded magnetoelastic ribbons were placed in polypropylene bottles for the cases of FAU and LTA hydrothermal synthesis and in an autoclave for MFI synthesis, since higher temperatures were needed. Samples were placed vertically with the help of a little teflon cylinder inside the reactors. That cylinder maintains the samples vertical to facilitate the formation of the zeolite membrane all over the surface of the ribbon. As in the previous section, the synthesis of the different zeolite membrane is going to be described separately.

✓ **FAU** membrane hydrothermal synthesis:

FAU membrane synthesis required two initial solutions. On the one hand, solution 'A' where 15.81 g H_2O, 0.716 g NaOH and 0.25 g Al foil were mixed and left under magnetic stirring at room temperature until all the aluminium was dissolved. It took 2-3 hours time, depending on how small the pieces of the aluminium foil were cut. On the other hand, solution 'B' where 22.59 g H_2O, 0.83 g NaOH, 1.84 g TEOS and 7.05 g TEA (triethanolamine) were mixed and maintained under magnetic stirring until TEOS hydrolysis happened, at least 12 hours at room temperature.

When both solutions were homogeneous, 'A' solution was filtered (Whatman No. 2) and slowly added to solution 'B' while being stirred, resulting in a final synthesis gel. This gel was then added to the polypropylene bottle where the magnetoelastic ribbon was vertically maintained and the hydrothermal synthesis took place into the furnace for 7 days at 85 ℃. Finally, the sample was taken out from the solution, cleaned with distilled water to eliminate the non-attached zeolite particles, dried and weighted.

To perform this synthesis an 'organic template' (TEOS) was used to ensure the correct formation of the zeolite membrane. This organic template was filling the pores of the zeolite structure, so the elimination of this reactant is mandatory to be able to use the channels and pores of the zeolite for sensing purposes. In order to get the zeolite structure empty of the organic template, the sample was annealed at 280 ℃ for 3 days. After this final treatment the samples was weighted again. The obtained film was characterized by XRD to ensure that the zeolite formed was the desired one. As can be observed in Figure 5.8, the measured diffraction pattern matches with the standard card of the FAU type zeolite.

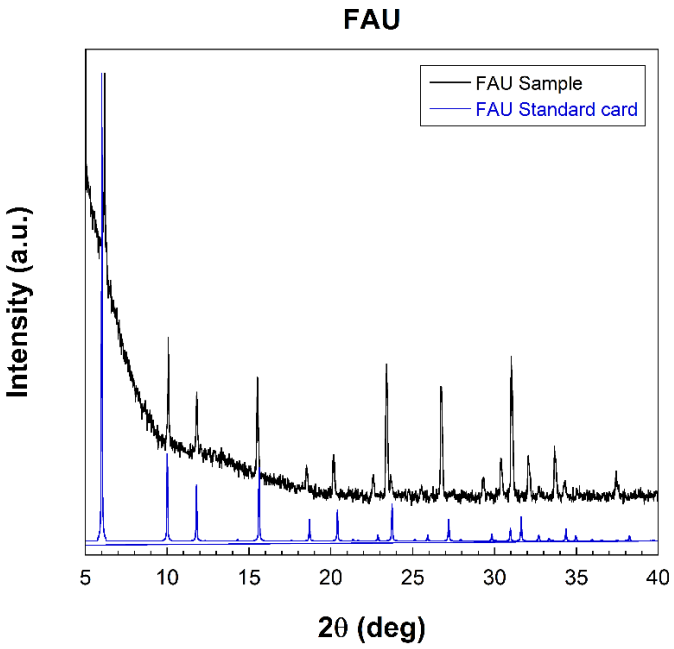

Figure 5.8. X-ray difractogram of the synthesized FAU membrane and a standard FAU card to probe the structure of the obtained membrane.

✓ MFI membrane hydrothermal synthesis:

In this case, a unique solution was prepared by mixing 30 ml H_2O, 5.65 ml TpAOH and 10.2 ml TEOS. The solution was maintained under stirring until TEOS hydrolysis took place, at least 12 hours at room temperature. As in the seed synthesis, the odour of the solution changed when TEOS was hydrolysed.

Once the synthesis solution was made, it was added carefully to the autoclave where the metallic ribbon was placed. It was closed and introduced into the furnace at 185 ℃ for 5 hours. After this, the autoclave was quickly cooled down with water to be able to take the sample out. Finally, the sample was cleaned with distilled water to eliminate the non-attached zeolite particles. It was dried and weighted.

As with the FAU zeolite case, TEOS 'organic template' was used to ensure the correct formation of the zeolite membrane. To eliminate it the sample was annealed at 280 ℃ for 5 days. After this final treatment the samples was weighted again. The obtained membrane was

characterized by XRD to ensure that the zeolite formed was the desired one. As can be observed in Figure 5.9, the obtained diffraction pattern matches with the standard card of the MFI type zeolite.

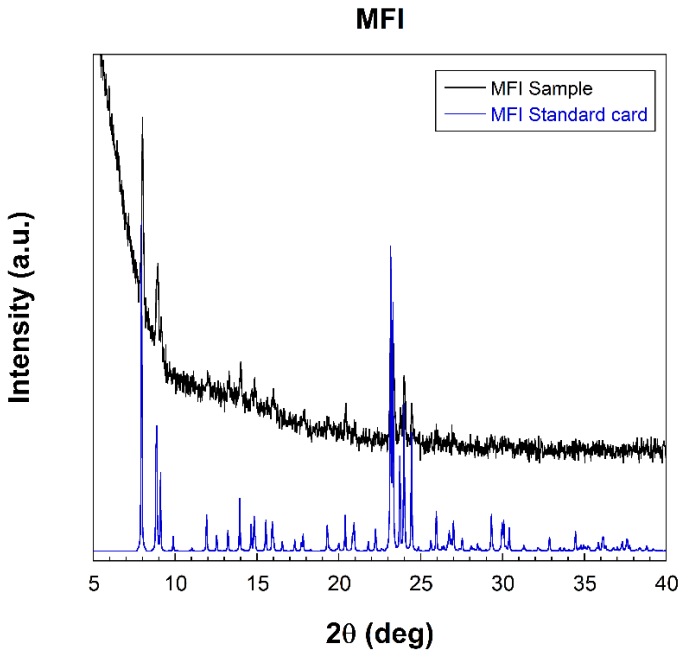

Figure 5.9. X-ray difractogram of the synthesized MFI membrane and a standard MFI card to probe the structure of the obtained membrane.

✓ **LTA** membrane hydrothermal synthesis:

An initial solution containing 30 ml H_2O and 2.96 g $NaAlO_2$ was prepared at 50 ℃ stirring for 15-20 minutes, until the sodium aluminate was totally dissolved. This solution was then filtered (Whatman No. 2) and slowly added to 7.24 g $NaSiO_3$ (liquid). A gel was formed blocking the magnetic stirrer and manual stirring with a spatula was needed to homogenise well the synthesized gel.

This gel was added to the polypropylene bottle where the seeded sensing platforms were. The polypropylene bottle was put into the oven at 100 ℃ for 5 hours in order the hydrothermal synthesis to take. After this, the samples were taken out from the bottle and cleaned with distilled water to eliminate the non-attached zeolite particles. Finally,

they were dried, weighted and characterized by XRD to ensure that the zeolite structure matches with the standard LTA card. The obtained diffraction pattern can be observed in Figure 5.10.

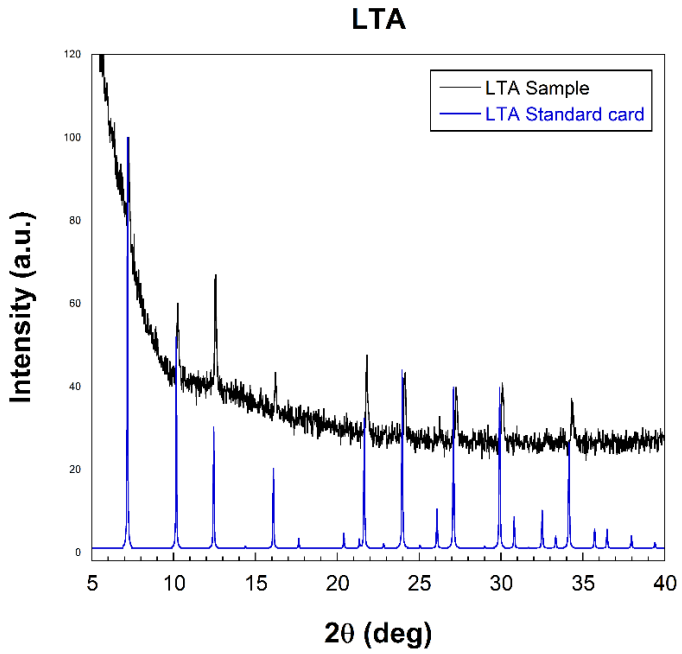

Figure 5.10. X-ray difractogram of the synthesized LTA membrane and a standard LTA card to probe the structure of the obtained membrane.

5.2.3. Detection process and results for o-xylene

The zeolite hydrothermal synthesis as well as the gas sensing experiments were carried out in the Laboratory of Composition and Applications of Microporous Materials, at FORTH Institute (Patras, Greece). A general view of the lab space where the sensing experiments were performed is presented in Figure 5.11.

Figure 5.11. Photograph of the laboratory space where the sensing experiments were performed.

Ortho-xylene is an aromatic hydrocarbon with formula $C_6H_4(CH_3)_2$, with two methyl substituents bonded to adjacent carbon atoms of a benzene ring and a kinetic diameter of 6.8 Å[38]. It is a colourless, flammable liquid usually produced in petrochemical industries by the methylation of toluene and benzene. It is considered a harmful substance, labelled with different R and S phrases, as R11 (highly flammable), R20 ((harmful by inhalation), R21 (harmful in contact with skin), R38 (irritating to skin) or S2 (keep out of the reach of children) and S25 (avoid contact with eyes). As it is a hazardous substance that may cause nervous system depression as well as liver, kidney and lung damage, the detection of o-xylene concentrations in the atmosphere has proved to be of great importance to avoid health damage.

The experimental set-up shown in Figure 5.11 for the sensing experiments is schematically presented in Figure 5.12 with some extra pictures showing in detail the different parts of the real system.

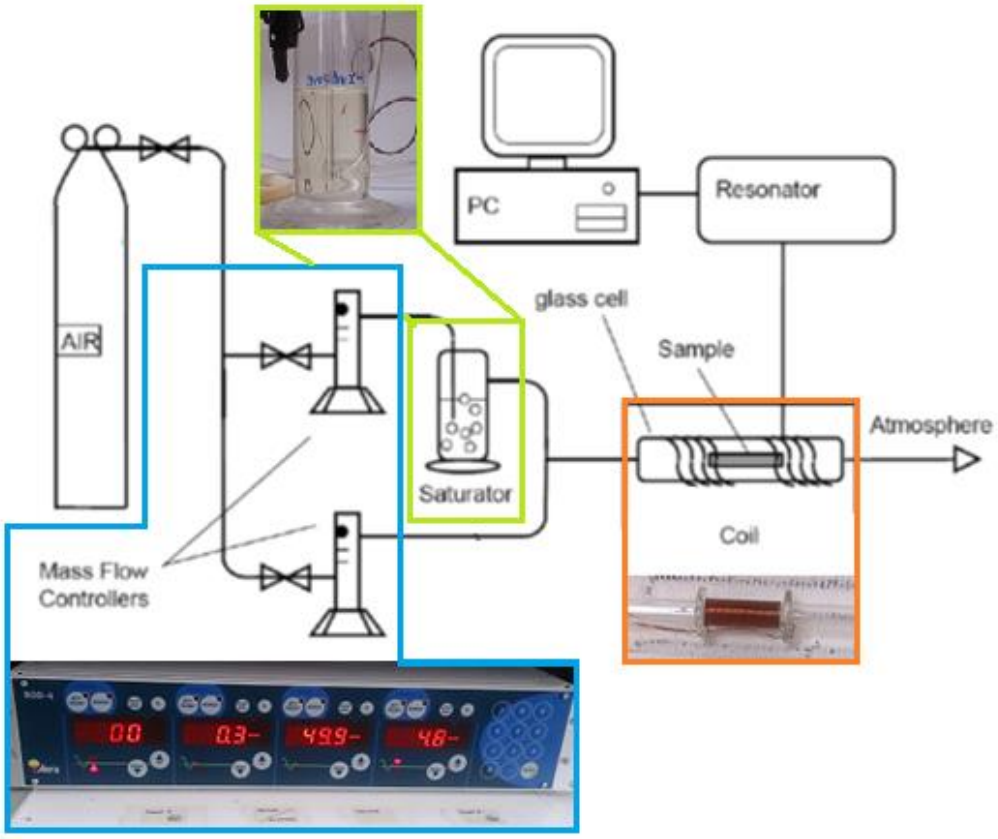

Figure 5.12. Experimental set-up scheme used to detect VOC's using the zeolite covered magnetoelastic material.

The sensing experimental set-up consist of a coil turned onto a glass tube where the gasses pass through creating a controlled atmosphere. The experiments were made in synthetic air atmosphere, the gas flow being driven by a mass flower controller. The gas flow was divided in two branches; the first one with only pure synthetic air, and the second one passing through the saturator where the o-xylene was in liquid state, in order to generate a saturated atmosphere. Those two branches converge again and with the help of a circuit of valves, the desired gas composition can be obtained. The desired o-xylene concentration was achieved by opening or closing the o-xylene path, as the branch of 'only air' branch was always kept open. Then the gas mixture (air or air + o-xylene) went through the sensing resonant platform which was located inside the glass tube surrounded by the coil. For the magnetoelastic resonance measurements, a microprocessor-controlled frequency generator drives a current amplifier connected to that single coil. It creates an alternating

magnetic field, which induces elastic waves on the sensor due to its magnetoelastic properties and, causes the mechanical vibration of the sample. When that mechanical vibration matches with the natural frequency of the sensor, magnetoelastic resonance occurs. The maximum measured frequency at that point is easily followed by an automatized set-up. Since the sample is inside the glass tube with the controlled atmosphere, the stream of gas passes through that glass tube getting in contact with the sensor. So, when the zeolite membrane deposited onto the magnetoelastic detects molecules of that gas stream, those molecules will be trapped into the membrane increasing the mass of the sensor and therefore decreasing its magnetoelastic resonance frequency.

At the same time, the glass tube with the sensing platform inside and the coil wrapped around it were placed inside a small furnace. This was done prior to start with the sensing experiments, to ensure that the pores and cavities of the fabricated zeolites were empty of any gas or substance. For this purpose, the fabricated sensors, with the different zeolite membranes onto them, were left overnight inside the system with an air flow of 20 sccm at 100 ^{o}C. This process is especially important to eliminate possible water vapour contained into the porous zeolite structures, from both channels and pores. After passing the whole night under such airflow, o-xylene detection started.

The study of the change of the resonant frequency of the developed sensing platforms as the o-xylene concentration varies was performed by changing the o-xylene concentration within the 'sensing chamber'. This was possible by using two mass flow controllers. Figure 5.13 shows a scheme of the detection procedure that has been followed in these measurements, AIR refers to only synthetic air flow and VOC refers to the o-xylene case, as this gas is a Volatile Organic Compound. Measurements were taken every 5 minutes, starting with an AIR flow of 50 sccm, during 30 minutes. Afterwards, o-xylene flow was switched on, and a mixture of 50 sccm AIR and 10 sccm o-xylene passed through the system for 60 minutes, taking measurements every 5 minutes. Finally, o-xylene flow was switched off and only AIR flow was measured for 30 minutes. This procedure was repeated by increasing the o-xylene concentration by 5 sccm at each step until reaching 30 sccm, in order to get and analyse

the response of the sensor to different o-xylene concentrations. The gas sensing measurements were performed at room temperature.

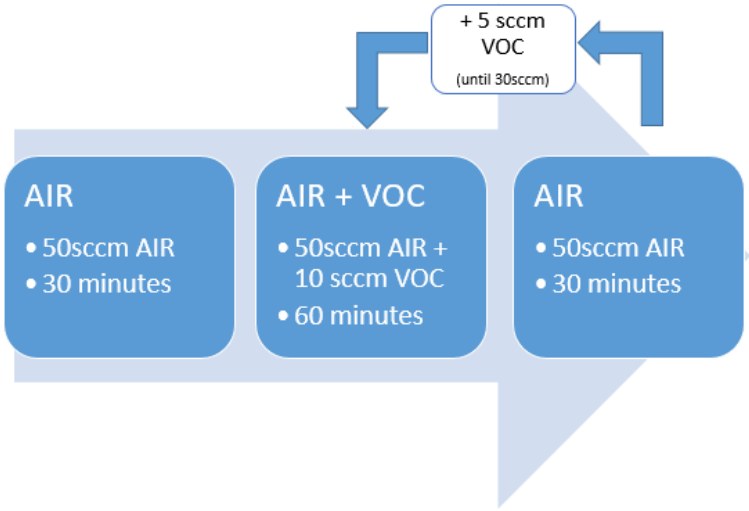

Figure 5.13. Scheme of the VOC detection process followed.

The results obtained for the resonant platforms (MER, magnetoelastic resonator), together with the three different types of zeolites synthesized are presented and discussed in the following.

✓ **MRP + FAU** detection results:

For the sample coated with Faujasite zeolite the obtained results do not show the expected behaviour, as can be observed in Figure 5.14. The magnetoelastic resonant frequency should have to decrease when the o-xylene flow was switched on, but the obtained response seems to be quite aleatory. In fact, it either increase or decrease when the VOC flow was on.

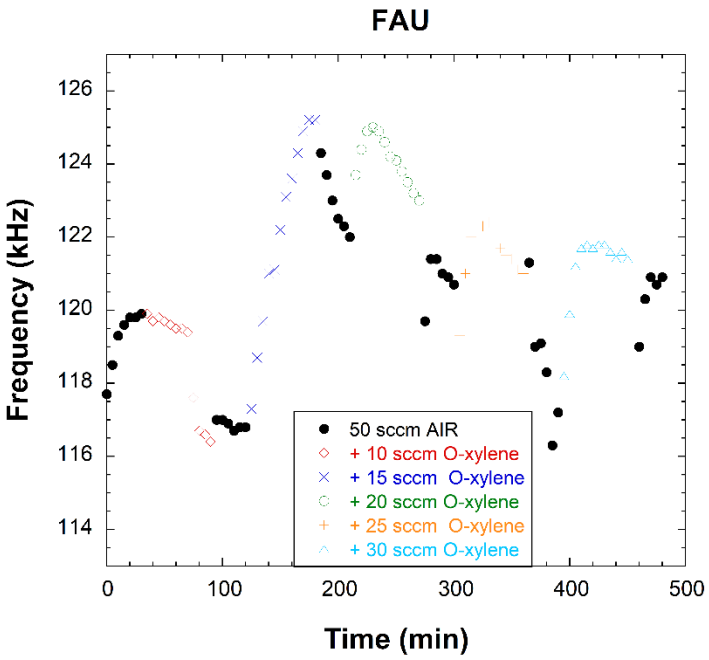

Figure 5.14. O-xylene sensing experiments with FAU zeolite.

This phenomenon could be explained if the formed zeolite membrane was not homogeneously formed. The resonant frequency change does not seem to be related with the o-xylene concentration in the created atmosphere, as it happened in the other cases.

✓ **MRP + MFI** detection results:

The sample with the Movil Five synthesized zeolite was the one that gave the best systematic response to the o-xylene concentration detection. As Figure 5.15 shows, the initial resonant frequency of the sample in only air atmosphere was of about 139kHz, and when the atmosphere was a mixture of air and o-xylene, the presence of the xylene made the resonant frequency to decrease due to the adsorption of the xylene inside the porous structure of the zeolite. Moreover, the decrease of the resonant frequency become bigger with higher o-xylene concentrations, until reaching a saturation value. As can be observed in Figure 5.15, for o-xylene flows higher than 20 sccm, that "saturation" resonant frequency value was of about 132 kHz, most probably indicating

that all the pores and cavities of the zeolite structure were filled with the o-xylene gas molecules and therefore no more quantity could be retained in the structure.

By performing this experiment, it was also possible to test the recovery process for the substrate (MER + zeolite). After any AIR + VOC measure during 60 minutes, a recovery period with only AIR was made during 30 minutes.

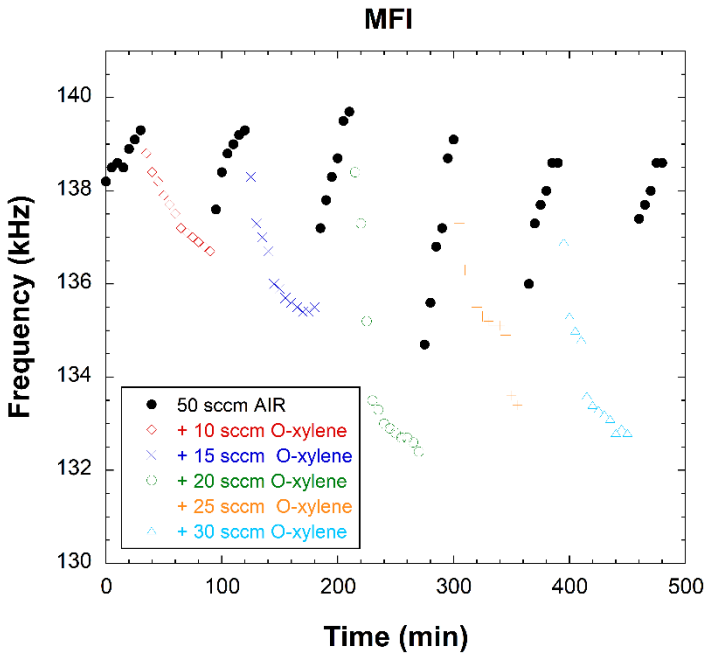

Figure 5.15. O-xylene sensing experiments with MFI zeolite.

As can be observed in Figure 5.15, it took almost those 30 minutes to recover the initial 'only air' value of the resonant frequency of about 139 kHz. This means that was not too difficult to get out the o-xylene from the pores and cavities of the zeolite and have it clean for the next experimental conditions.

The o-xylene concentration was calculated from Raoult's law assuming that the first air stream (through the bubbler) was saturated by organic vapor and knowing the vapor pressure of the o-xylene at room temperature, calculated from equation [5.1] (with temperature value in Kelvin the obtained pressure is given in Pascal):

$$P_{VOC} = \exp(C_1 + \frac{C_2}{T} + C_3 \ln T + C_4 T^{C_5}) \qquad [5.1]$$

where C1, C2, C3, C4 and C5 are constant values for each volatile organic compound[39]. For the o-xylene, the values are 90.3, -7948.3, -10.08, $5.97 \cdot 10^{-6}$ and 2 respectively, giving a vapour pressure value at room temperature (298K) of 880.95 Pa (0.008694 at).

With the concentration values of o-xylene given in ppm, the response and sensitivity of our sensor can be analysed. Figure 5.16 shows the obtained shift in the resonance frequency due to the different concentrations of o-xylene. As can be clearly observed the frequency smoothly increases with the VOC concentration until reaching a steady value. At lower concentrations of o-xylene the shift of the resonance frequency is higher, nevertheless it seems that at certain concentration the zeolite is not able to retain more quantity of xylene and the shift on the frequency remains almost constant. The obtained experimental values polynomial fitting agrees with a second order expression, as it happened in the obtained curves for the polymer depositions.

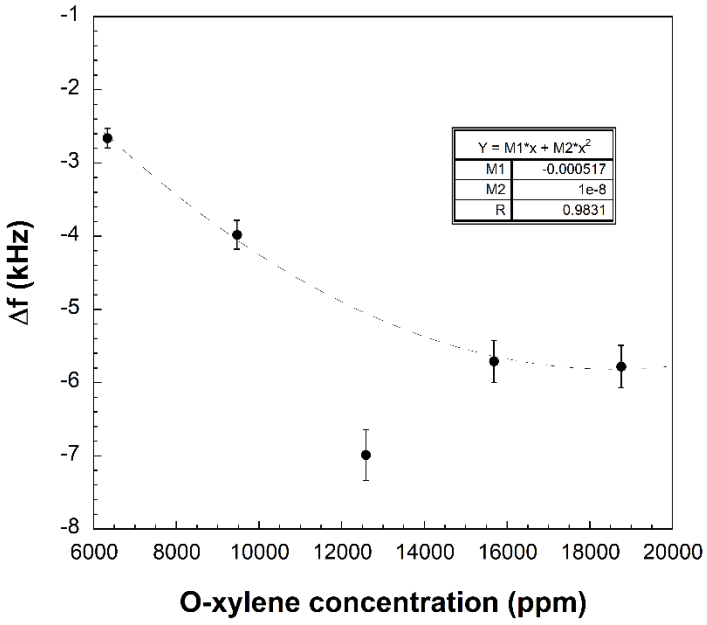

Figure 5.16. Resonant frequency shift due to o-xylene increasing concentration with MFI zeolite.

The sensitivity of our sensor can be estimated from the linear fitting of the obtained values for low o-xylene concentrations being about 0.5 Hz/ppm (see Figure 5.17). It has been also taken into account that there is a saturation detection limit of about 13000 ppm.

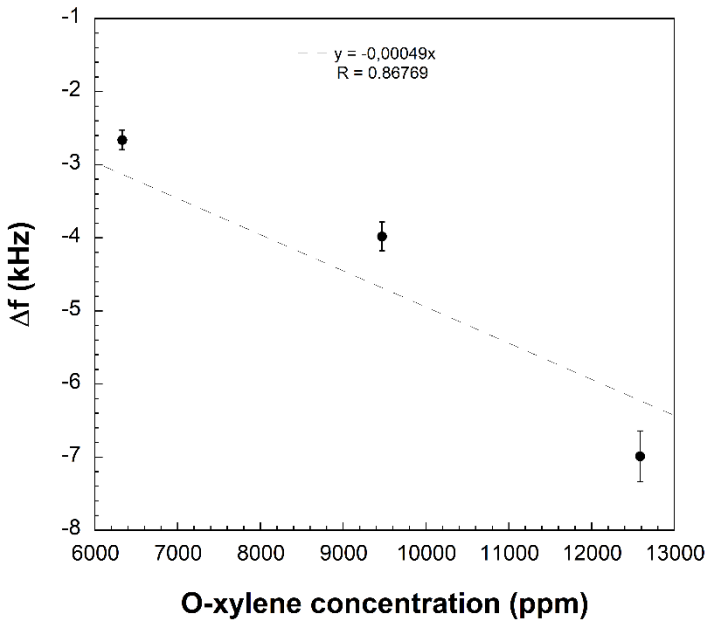

Figure 5.17. Sensitivity results for low o-xylene concentrations with MFI zeolite.

✓ **MRP + LTA** detection results:

The Lynde Type A sample gave intermediate results if compared with the obtained behaviours with the FAU and MFI samples. Performed measurements in this last case are presented in Figure 5.18, and a decrease of the resonance frequency can be observed when o-xylene was present in the atmosphere. Due to initial technical problems, because the sample does not seem to be totally humidity free, the obtained values for the initial AIR and AIR + 10 sccm o-xylene, cannot be taken into account. In the subsequent measurements the expected behaviour appeared, being the initial resonance frequency value in only air atmosphere of about 128 kHz, and always decreasing when the o-xylene concentration increased. In this case, the variation of the

resonance frequency (and also the sensitivity to the detection) is lower than in the case of the MFI zeolite: an abrupt initial change and only of about 2 kHz and almost constant once the o-xylene has been applied.

This phenomenon could be explained taken into account the pore size of the both structures. LTA membrane is formed by channels of pores of 4.2 Å of diameter, while MFI channels have a diameter of 5 Å. Due to this difference in the pore size, xylene molecules can penetrate better in MFI structure where pores are bigger, giving a higher change in the resonance frequency of the system when same flow conditions are compared.

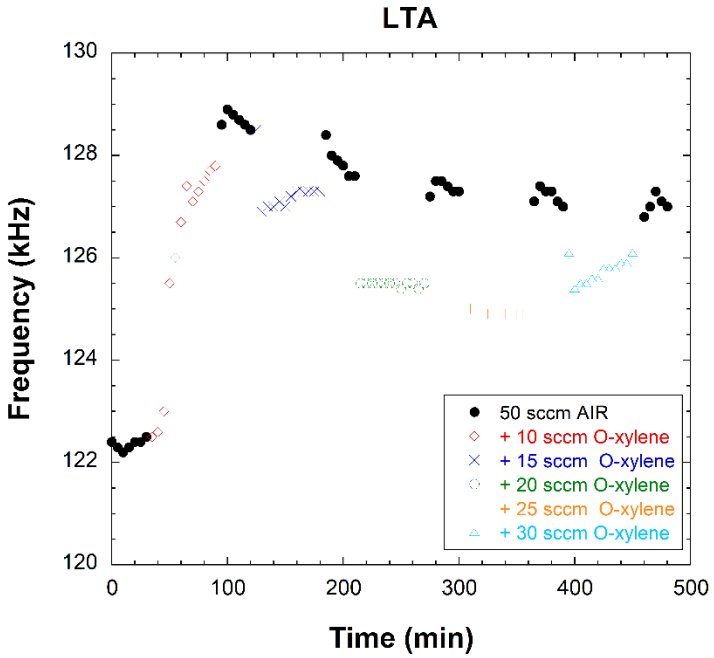

Figure 5.18. O-xylene sensing experiments with LTA zeolite.

As can be observed in Figure 5.18, in LTA sensing experiments there is not a gradual and progressive insertion of the o-xylene molecules inside the zeolite membrane. The change of the resonance frequency is always abrupt and of about 2 kHz, what let us think that there is no adsorption of the o-xylene inside the membrane of the LTA. As LTA is the studied zeolite with the smallest pore size, o-xylene may not be small enough to go inside the membrane. Therefore, o-xylene molecules can only be attached to the surface of the zeolite membrane. This causes

that rapid change on the resonant frequency without a gradual decrease of it, as it happened in the MFI study.

O-xylene whole molecule's kinetic diameter (6.8 Å) seems to be big if compared with the MFI (5 Å) and LTA (4.2 Å) channels size. However, the kinetic diameter of the benzene ring (5.85 Å) and the methyl group (2 Å, Van der Waals radius), matched and is slightly smaller, respectively than the pore size of the MFI zeolite. Because of this fact, MFI measured sensing ability turns out to be better than when using LTA zeolite.

5.3. Summary and conclusions

The results shown in this chapter demonstrate that it is possible to fabricate a magnetoelastic resonance-based device for gas sensing purposes, provided that the surface of the magnetoelastic strip is properly functionalized.

Resonant platforms of composition $Fe_{64}Co_{21}B_{15}$ in the form of ribbons have been fabricated using the melt spinning technique. Such platforms have good magnetic and magnetoelastic properties, which make them suitable for sensing applications.

Additionally, a protective layer was needed to improve the corrosion resistance of the alloys as later processes involve alkali water media. For that purpose, a titanium protective layer was sputtered onto the surface of the ribbons on both sides. Although other metals were tested as protective layers, titanium was the one with the best adhesion and sensing ability results, as gold detached from the surface of the ribbons and chromium did not allow to sense the target analyte.

Finally, the active layer was deposited onto the protected ribbon. Three samples were studied simultaneously having one different zeolite each; Faujasite (FAU), Movil Five (MFI) and Lynde Type A (LTA). In order to have more reactive surface, both sides of the samples were covered with the titanium and the zeolite membranes. The formation of the zeolite membrane took place in two steps; first, a seeding procedure was

made and then the hydrothermal synthesis of the zeolites was carried out.

The synthesis processes for used zeolites was different starting from the seeding process. In the case of the FAU synthesis, commercial powder was used to fabricate the seeding solution while for the case of MFI and LTA, the seeds were fabricated following a recipe found in literature. After the seeding process, the hydrothermal synthesis of the zeolites took place to cover the magnetoelastic material surfaces. After that an annealing treatment was needed for the FAU and MFI zeolites, due to the presence on the synthesis of an organic template that was filling the pores and channels that will be needed for the sensing experiments.

All the samples were characterized by XRD measurements to ensure the structure of the formed zeolite.

Once the sensors were made, sensing experiments were carried out with a totally homemade system. A gas stream passed though the sensor and changes on the resonant frequency of the system were observed when the gas flow contained o-xylene in it.

Results obtained for the three zeolites showed that some problems occurred in the FAU synthesis as the behaviour of the sensor was not the expected one, probably due to the bad formation of the zeolite membrane.

In the case of the LTA sensor, some response was observed when the o-xylene concentration increases, nevertheless the initial measures reveal also a problem on the system.

Finally, the results obtained for the MFI sample reveal that this was the best fabricated sensor. O-xylene is gradually adsorbed by the MFI membrane, decreasing in consequence the resonance frequency of the sensor and making possible the detection of the o-xylene concentrations in air atmospheres. The obtained sensitivity value for this sensor has been of about 0.5 Hz/ppm. The higher limit of detection until the membrane was not able to trap more o-xylene was of about 13000 ppm, giving an almost constant frequency change of about 5.75 kHz. For this system, there was a good relationship between the concentration of o-xylene in

the atmosphere and the change on the resonance frequency. It has also been observed that the recovery time for this system was not too large, as in 30 minutes in air atmosphere the sample recovered the initial resonance frequency value.

References

[1] C.A. Grimes, S.C. Roy, S. Rani and Q. Cai, "Theory, instrumentations and applications of magnetoelastic resonance sensors: a review", Sensors 11 (2011) 2809-2844. DOI: 10.3390/s110302809.

[2] M.K. Jain, S. Schmidt, K.G. Ong, C. Mungle and C.A. Grimes, "Magnetoelastic remote query temperature and humidity sensors", Smart Materials and Structures 9 (2000) 502-510.

[3] R. Zhang, M.I. Tejedor, M.A. Anderson, M. Paulose and C.A. Grimes, "Ethylene detection using nanoporous Pt-TiO2 coatings applied to magnetoelastic thick films", Sensors 2 (2002) 331-338.

[4] Zribi, A. Knobloch, W.C. Tian and S. Goodwin, "Micromachined resonant multiple gas sensor", Sensors and Actuators A: Physical 122 (2008) (1) 31-38. DOI: 10.1016/j.sna.2004.12.034.

[5] Q.Y. Cai, A. Cammers-Goodwin and C.A. Grimes, "A wireless, remote query magnetoelastic CO_2 sensor", Journal of Environmental Monitoring 2 (2000) 556-560.

[6] Q.Y. Cai, M.K. Jain and C.A. Grimes, "A wireless, remote query ammonia sensor", Sensors and Actuators B: Chemical 77 (2001) 614-619.

[7] T. Baimpos, P. Boutikos, V. Nikolakis and D. Kouzoudis, "A polymer-metglas sensor used to detect volatile organic compounds", Sensors and Actuators A: Physical 158 (2010) (2) 249-253. DOI: 10.1016/j.sna.2010.01.020.

[8] R. Shao, E.L. Tan, C.A. Grimes and K.G. Ong, "A wide-area, Wireless, passive dosimeter for tracking mercury vapor exposure", Sensors Letters 5 (2007) 615-620. DOI: 10.1166/sl.2007.237.

[9] I.G. Giannakopoulos, D. Kouzoudis, C.A. Grimes and V. Nikolakis, "Synthesis and characterization of a composite zeolite-metglas carbon dioxide sensor", Advanced functional materials 15 (2005) (7) 1165-1170. DOI: 10.1002/adfm.200400515.

[10] T. Baimpos, D. Kouzoudis and V. Nikolakis, "Use of a zeolite LTA film for the elective detection of light hydrocarbons", Science of advanced materials 2 (2010) 215-218. DOI: 10.1166/sam.2010.1089.

[11] T. Baimpos, L. Gora, V. Nikolakis and D. Kouzoudis, "Selective detection of hazardous VOCs using zeolite/metglas composite sensors", Sensors and actuators A: Physical 186 (2012) 21-31. DOI: 10.1016/j.sna.2011.12.030.

[12] A.F. Cronstedt, (1756) Kongl. Vetenskaps Akad. Handl. Stockholm, 17, 120-123.

[13] www.iza-structure.org (08/2017)

[14] L.B. McCusker and C. Baerlocher, "Zeolite structures", Studies in Surface Science and Catalysis 157 (2005) 41-64. ISBN: 978-0-444-52066-1.

[15] J. Weitkamp, "Zeolites and catalysis", Solid State Ionics 131 (2000) 175-188. DOI: 10.1016/S0167-2738(00)00632-9.

[16] M.O. Daramola, E. Aransiola and T.V. Ojumu, "Potential applications of zeolite membranes in reaction coupling separation processes", Materials 5 (2012) 2101-2136. DOI: 10.3390/ma5112101.

[17] W. Loewenstein, "The distribution of aluminium in the tetrahedra of silicates and aluminates", American Mineralogist 39 (1954) 92-96.

[18] R.M. Barrer, "Zeolites and clay minerals as sorbents and molecular sieves", Academic Press, London, (1978) 497. ISBN: 0120793504.

[19] R.M. Barrer, "Zeolite Structure" [37-82] and "Soption by zeolites" [227-285], Zeolites Science and Technology (1984). ISBN: 978-94-009-6130-2.

[20] L.B. Sand and F.A. Mumpton, "Natural Zeolites: Occurrence, Properties, Use", Pergamon Press, Oxford (1978). ISBN: 0080219225.

[21] G.V. Tsitsishvili, T.G. Andronikashvili, G.N. Kirov and L.D. Filizova, "Natural Zeolites" Ellis Horwood, New York (1992). ISBN: 0136120377 9780136120377.

[22] T.Q. Silva, M.B. dos Santos, A.A.C. Santiago, D.O. Santanda, F.T. Cruz, H.M.C. Andrade and A.J.S. Mascarenhas, "Gas phase glycerol oxidative dehydration over bifunctional V/H- zeolite catalysts with different zeolite topology", Catalysis today 298 (2017) (1) 38-46. DOI:10.1016/j.cattod.2016.08.011.

[23] SM. Shahinuzzaman, Z. Yaakob and Y. Ahmed, "Non-sulphide zaolilte catalyst for bio-jet-fuel conversion", Renewable and Sustainable Energy Reviews 77 (217) 1375-1384. DOI: 10.1016/j.rser.2017.01.162.

[24] E. Wibowo, Sutisna, M. Rokhmat, R. Murniati, Khairurrijal, and M. Abdullah, "Utilization of natural zeolite as sorbent material for seawater desalination", Procedia Engineering 170 (2017) 8-13. DOI: 10.1016/j.proeng.2017.03.002.

[25] P. Arnnok, N. Patdhanagul and R. Burakham, "Dispersive solid-phase extraction using polyaniline-modified zeolite NaY as a new sorbent for multiresidue analysis of pesticides in food and environmental samples", Talanta 164 (2017) 651-661. DOI: 10.1016/j.talanta.2016.11.003.

[26] A.R. Loiola, J.C.R.A. Andrade, J.M. Sasaki and L.R.D. da Silva, "Structural analysis of zeolite NaA synthesized by a cost-effective hydrothermal method using kaolin and its use as water softener", Journal of Colloid and Interface Science 367 (2012) 34-39. DOI: 10.1016/j.jcis.2010.11.026.

[27] R.A. Bessa, L.S. Costa, C.P. Oliviera, F. Bohn, R.F. do Nascimiento, J.M. Sasaki and A.R. Loiola, "Kaolin based magnetic zeolites A and P as water softeners", Microporous and Mesoporous materials 245 (2017) 64-72. DOI: 10.1016/j.micromeso.2017.03.004.

[28] B. Wang and P.K. Dutta, "Influence of cross-linking, temperature, and humidity on CO_2/N_2 separation performance of PDMS coated zeolite membranes grown within a porous poly(ether sulfone) polymer", Industrial and Engineering Chemistry Research 56 (2017) (20) 6065-6077. DOI: 10.1021/acs.iecr.7b00850.

[29] A. Mundstock, S. Friebe and J. Caro, "On comparing permeation through Matrimid-based mixed matrix and multilayer

sandwich FAU membranes: H_2/CO_2 separation, support functionalization and ion exchange", International Journal of Hydrogen Energy 42 (2017) 279-288. DOI: 10.1016/j.ijhydene.2016.10.161.

[30] S. Mandal, A.D. Planells and H.K. Hunt, "Impact of deposition and laser densification of Silicate-1 films on their optical characteristics", Microporous and Mesoporous Materials 223 (2016) 68-78. DOI: 10.1016/j.micromeso.2015.10.035.

[31] J. Lin, Y. Dong, Q. Zhang, D. Hu, N. Li, L. Wang, Y. Liu and T. Wu, "Interrupted chalcogenide-bsed zeolite-analogue semiconductor: atomically precise doping for tunable electro-/photoelectrochemical properties", Angewandte Chemie International Edition 54 (2015) 5103-5107. DOI: 10.1002/anie.201500659.

[32] M. Denoual, D. Robbes, S. Inoue, Y. Mita, J. Grand, H. Awala and S. Mintova, "Thermal resonant zeolite-based gas sensor" Sensors and Actuators B: Chemical 245 (2017) 179-182. DOI: 10.1016/j.snb.2017.01.131.

[33] G.P. Alcantaram L.E.B. Ribeiro, A.F. Alves, C.M.G. Andrade and F. Fruett, "Humidity sensor based on zeolite for application under environmental conditions", Microporous and Mesoporous 147 (2017) 38-45. DOI:10.1016/j.micromeso.2017.03.042.

[34] R. Kandyala, S.P.C. Raghavendra and S.T. Rajasekharan, " Xylene: an overview of its health hazards and preventive measures", Journal of Oral and Maxillofacial Pathology 14 (2010) (1) 1-5. DOI: 10.4103/0973-029X.64299.

[35] "Toxicological profile for xylene", U.S. Department of Health and Human Services (2007).

[36] Y. Zheng, X. Li and P.K. Dutta, "Exploitation of unique properties of zeolites un the development of gas sensors", Sensors 12 (2012) (4) 5170-5194. DOI: 10.3390/s120405170.

[37] M. Jafari, A. Nouri, M. Kazemimoghadam and T. Mohammadi, "Investigations on hydrothermal synthesis parameters in preparation of nanoparticles of LTA zeolite with the aid of TMAOH", Powder Technology 237 (2013) 442-449. DOI:10.1016/j.powtec.2012.12.031.

[38] C.D. Baertsch, H.H. Funke, J.L. Falconer and R.D. Noble, "Permetaion of aromatic hydrocarbon vapors though silicalite-zeolite membranes" The Journal of Physical Chemistry A 100 (1996) 7676-7679. DOI: 10.1021/jp960226h.

[39] "Perry's chemical engineers handbook [Table 2-6 Vapor pressure of inorganic and organic liquids]", Seventh edition, MacGraw-Hill (1997) 2-50-2-54. ISBN: 0-07-049841-5.

6. General conclusions and open perspectives

This last chapter summarizes the obtained conclusions from each experimental chapter: first, concerning the parameters affecting the sensing device itself as the characteristics of the magnetoelastic metallic glass as well as its functionalization by using an active layer as a polymer (like Polystyrene); second the zinc oxide deposition methods, the calculation of the zinc oxide Young modulus value and the hydrogen peroxide sensing ability of the hemoglobin coated metglas/ZnO system; and finally the resonant platform surface functionalization with zeolites, their characterization and o-xylene sensing ability. To conclude this PhD report, some open perspectives and future lines of work will be indicated.

6.1. General conclusions

The most important conclusion derived from this thesis is that magnetoelastic resonators can be functionalized with properly chosen active layers in order to develop biological and chemical sensing devices. In particular,

✓ In Chapter 3 it has been proved that it is possible to coat the homemade magnetoelastic ribbons with polystyrene. Nevertheless, due to the high roughness of the as quenched amorphous ribbons, a previous acid treatment is needed to ensure the good adherence between the magnetoelastic strip and the polymer. The deposition process was carried out by the dip coating technique. In order to obtain a homogenous polymer film covering the amorphous alloy, several factors affecting the film layer formation must be taken into account: the concentration of the dipping solutions, the immersion time, and the solvent used, as the most important ones. It has been observed that the employed solvent influences the amount of mass deposited, as the mass quantities obtained by using THF and toluene are different even by following the same deposition procedure. This has been attributed to the solvent inherent properties, as they have different polarity and water miscibility. More experiments about the influence of the solvent and of the substrate must be perform to understand properly these processes.

Concerning the magnetoelastic resonators and taking into account that for our purposes many of the experiments will be performed in water solution, we have been able to fabricate Cr containing metallic glasses that show high corrosion resistance properties, and to proceed to their full characterization. About the parameters affecting the sensing ability of these magnetoelastic resonators, a comparison of the obtained sensitivity and quality factor of different length ribbons and at different applied magnetic fields was performed. It has been observed that the most sensitive device to the deposited mass is, as expected, the smallest one (L = 1 cm) since it shows the highest Q value. Linearity has been observed in the initial deposition processes when the deposited mass is really small. Nevertheless, theoretical prediction about the linear

dependence of the mass change to resonant frequency change with slope 0.5 needs of a deep revision.

✓ In Chapter 4 it has been demonstrated that it is possible to directly coat a magnetoelastic amorphous commercial material (Metglas 2826MB3) with a zinc oxide active layer by properly controlling parameters such as the temperature or time of the ZnO synthesis conditions. From the obtained results, it was concluded that the best way to deposit a homogenous layer of ZnO is by making a direct casting with the previously synthetized ZnO nanoparticles. By performing successive depositions following that procedure it has been possible to determine the Young modulus of the deposited ZnO film, that has been calculated to be of about 60 GPa for a 1 μm thick ZnO layer.

The deposition of ZnO as active layer allows us to fabricate a biosensor to monitor the oxidation of the hemoglobin protein (attached to the ZnO layer) with hydrogen peroxide. The fabricated sensor was used to simultaneously follow the process by two different methods: cyclic voltammetry (CV) and magnetoelastic resonance. Concerning CV measurements catalysis currents increase linearly with the H_2O_2concentration in a wide range of 25-350 μM. The detection limit is 25-50 μM and the Metglas/ZnO/Hb electrode displays rapid response (30 s) to H_2O_2, and exhibits good stability and reproducibility of the measurements. On the other hand, the performed magnetoelastic measurements show a small linear mass increase versus the H_2O_2concentration with a slope of 152 ng/μM, a mass change that is most probably due to H_2O_2adsorption in ZnO during the electrochemical reaction.

✓ Results shown in Chapter 5 demonstrate that it is possible to fabricate a magnetoelastic resonance based device for Volatile Organic Compounds (VOC) sensing purposes with zeolites working as active layer. In this case, the sensor was fabricated by using a homemade amorphous ribbon of composition $Fe_{64}Co_{21}B_{15}$, which had to be protected before zeolite membrane formation with a passive layer of titanium, in order to avoid corrosion processes during the zeolite synthesis processes. Three

different zeolite types have been hydrothermally synthesized onto the surface of the magnetoelastic material: Faujasite (FAU), Movil Five (MFI) and Lynde Type A (LTA), and characterized using XRD.

Sensing experiments were performed to detect o-xylene, a hazardous volatile organic compound. No sensing response was obtained for FAU zeolite containing resonant platform, probably because of a bad formation of the zeolite membrane during the hydrothermal synthesis. For LTA zeolite containing sensor, some response was observed but it was probably due to a superficial attachment and not to an adsorption process, as the resonance frequency change instead of increasing with the increasing concentration of gas, turns out to be abrupt and almost constant and about 2 kHz for all the concentrations. The best results were obtained for the MFI sample, where the o-xylene is gradually adsorbed, decreasing in consequence the resonant frequency of the sensor. For MFI sample, the obtained sensitivity was of about 0.5 Hz/ppm.

6.2. Open perspectives

This work has generated new doubts and has opened new routes for us to continue the research on magnetoelastic resonators by studying the different processes to fabricate such sensing systems. Thus, we would like to get deeper in the functionalization processes of the magnetoelastic ribbons for specific chemical or biological target molecules:

- Trying to improve the zeolite synthesis onto the magnetoelastic materials in order to have a well fabricated membrane that will be able to discriminate different but at the same time similar gases, in order to have a more specific detection system.

- Using new semiconductors as active layers, as for example SnO_2, which is much more conducting than ZnO and that can

easily and reproducibly be prepared by a low temperature route. This tin oxide has already been successfully deposited onto IOT-PET plastic substrates, and has proved to be useful to properly attach hemin. Hemin is a much smaller molecule that hemoglobin, that could be attached easily on the surface of the deposited SnO_2 film and could be used to follow the electrocatalytic reduction of the H_2O_2.

- By choosing new types of active layers: another good alternative to functionalize the surface of the homemade amorphous ribbons would be Metal-Organic Frameworks, MOFs. Those MOFs are compounds consisting of metal ions or clusters coordinated to organic ligands to form three-dimensional porous structures. Due to the presence of organic ligands they can be synthesised to selectively adsorb pollutant compounds as Volatile Organic Compounds (VOCs). Therefore, by covering our magnetoelastic ribbons with these MOFs, it could be possible to detect different kinds of gases as toluene, for example.

On the other hand, it would be interesting to follow with the analysis of the parameters affecting the sensing ability of those magnetoelastic resonant platforms:

- On one hand, by going deeper in the study of the quality factor *Q*, trying to study the best way to determine it, and the parameters affecting it.

- On the other hand, by improving the fabrication of smaller magnetoelastic resonators of about a few millimetres. A 5 mm resonator will have not only a very low mass value but also a resonant frequency about 1 MHz, facts that lead directly to a high sensitivity for chemical and biological detection.

Appendix

List of publications arisen from this work:

- A. Sagasti, J. Gutiérrez, M. San Sebastián and J.M. Barandiarán, "Magnetoelastic resonators for highly specific chemical and biological detection: a critical study", IEEE Transactions on Magnetics 53 (4), 4000604, (2017). DOI: 10.1109/TMAG.2016.2622359.

- A. Sagasti, N. Bouropoulos, D. Kouzoudis, A. Panagiotopoulos, E. Topoglidis and J. Gutiérrez, "Nanostructured ZnO in Metglas/ZnO/Hemoglobin modified electrode to detect the oxidation of the hemoglobin simultaneously by cyclic voltammetry and magnetoelastic resonance" Materials 10, 849, (2017). DOI: 10.3390/ma10080849.

- A. Sagasti, A.C. Lopes, A. Lasheras, V. Palomares, J. Carrizo, J. Gutiérrez and J.M. Barandiarán, "Corrosion resistant metallic glasses for biosensing applications", AIP Advances 8, 047702, (2018) DOI: 10.1063/1.4994108.

- A.C. Lopes, A. Sagasti, A. Lasheras, V. Muto, J. Gutiérrez, d. Kouzoudis and J.M. Barandiarán, "Accurate determination of the Q quality factor in magnetoelastic resonant platforms for advanced biological detection" (in preparation).